



Calhoun: The NPS Institutional Archive
DSpace Repository

Theses and Dissertations

1. Thesis and Dissertation Collection, all items

2005-12

Evaluation of surface current mapping performance by SeaSonde High Frequency radar through simulations

Toh, Kwang Yong Daniel

Monterey, California. Naval Postgraduate School

<https://hdl.handle.net/10945/1803>

This publication is a work of the U.S. Government as defined in Title 17, United States Code, Section 101. As such, it is in the public domain, and under the provisions of Title 17, United States Code, Section 105, is not copyrighted in the U.S.

Downloaded from NPS Archive: Calhoun



Calhoun is the Naval Postgraduate School's public access digital repository for research materials and institutional publications created by the NPS community. Calhoun is named for Professor of Mathematics Guy K. Calhoun, NPS's first appointed -- and published -- scholarly author.

Dudley Knox Library / Naval Postgraduate School
411 Dyer Road / 1 University Circle
Monterey, California USA 93943

<http://www.nps.edu/library>



**NAVAL
POSTGRADUATE
SCHOOL**

MONTEREY, CALIFORNIA

THESIS

**EVALUATION OF SURFACE CURRENT MAPPING
PERFORMANCE BY SEASONDE HIGH FREQUENCY
RADAR THROUGH SIMULATIONS**

by

Kwang Yong Daniel Toh

December 2005

Thesis Advisor:
Second Reader:

Jeffrey D. Paduan
Steven R. Ramp

Approved for public release; distribution is unlimited

THIS PAGE INTENTIONALLY LEFT BLANK

REPORT DOCUMENTATION PAGE			Form Approved OMB No. 0704-0188	
Public reporting burden for this collection of information is estimated to average 1 hour per response, including the time for reviewing instruction, searching existing data sources, gathering and maintaining the data needed, and completing and reviewing the collection of information. Send comments regarding this burden estimate or any other aspect of this collection of information, including suggestions for reducing this burden, to Washington headquarters Services, Directorate for Information Operations and Reports, 1215 Jefferson Davis Highway, Suite 1204, Arlington, VA 22202-4302, and to the Office of Management and Budget, Paperwork Reduction Project (0704-0188) Washington DC 20503.				
1. AGENCY USE ONLY (Leave blank)		2. REPORT DATE December 2005	3. REPORT TYPE AND DATES COVERED Master's Thesis	
4. TITLE AND SUBTITLE: Evaluation of Surface Current Mapping Performance by SeaSonde High Frequency Radar Through Simulations			5. FUNDING NUMBERS	
6. AUTHOR(S) Toh, Kwang Yong Daniel				
7. PERFORMING ORGANIZATION NAME(S) AND ADDRESS(ES) Naval Postgraduate School Monterey, CA 93943-5000			8. PERFORMING ORGANIZATION REPORT NUMBER	
9. SPONSORING /MONITORING AGENCY NAME(S) AND ADDRESS(ES) N/A			10. SPONSORING/MONITORING AGENCY REPORT NUMBER	
11. SUPPLEMENTARY NOTES The views expressed in this thesis are those of the author and do not reflect the official policy or position of the Department of Defense or the U.S. Government.				
12a. DISTRIBUTION / AVAILABILITY STATEMENT Approved for public release; distribution is unlimited			12b. DISTRIBUTION CODE	
13. ABSTRACT (maximum 200 words) The use of the HF radar to measure and map surface currents has proliferated along the coastlines of many countries for purposes of Search and Rescue, Oil Spill Management, Oceanographic and Fishery Science studies. In the US Navy, these surface current maps are being evaluated for operational use in real-time data assimilating coastal circulation models, and direct monitoring tools in environmentally sensitive operating areas. The SeaSonde HF radar, a DF system, was considered in this study. It uses the MUSIC algorithm to recover bearings from the Doppler backscatter spectrum of the sea surface. By varying the radial and antenna patterns, the simulated backscatter spectra were passed through the SeaSonde software suite for radial pattern recovery. This unprecedented approach directly evaluated SeaSonde's MUSIC, and the associated uncertainties were examined against the simulated inputs of (1) fixed amplitude and phase deviations from the ideal antenna pattern, (2) measured antenna patterns and (3) decreasing SNR. It was found that using the measured antenna pattern to recover radials yielded least uncertainty, but a definitive prediction of MUSIC's radial-recovery capability in relation to the pattern's complex amplitude and phase structure remained illusive. The results highlighted the need to calibrate the military's DF-systems for accurate azimuth recovery.				
14. SUBJECT TERMS SeaSonde HF radar, Ocean surface current, MUSIC, simulations, antenna patterns, SNR			15. NUMBER OF PAGES 123	
			16. PRICE CODE	
17. SECURITY CLASSIFICATION OF REPORT Unclassified	18. SECURITY CLASSIFICATION OF THIS PAGE Unclassified	19. SECURITY CLASSIFICATION OF ABSTRACT Unclassified	20. LIMITATION OF ABSTRACT UL	

THIS PAGE INTENTIONALLY LEFT BLANK

Approved for public release; distribution is unlimited

**EVALUATION OF SURFACE CURRENT MAPPING PERFORMANCE BY
SEASONDE HIGH FREQUENCY RADAR THROUGH SIMULATIONS**

Kwang Yong Daniel Toh
MAJ, Republic of Singapore Navy
B.Engr. (Electrical), National University of Singapore, 1997

Submitted in partial fulfillment of the
requirements for the degree of

MASTER OF SCIENCE IN PHYSICAL OCEANOGRAPHY

from the

**NAVAL POSTGRADUATE SCHOOL
December 2005**

Author: Kwang Yong Daniel Toh

Approved by: Jeffrey D. Paduan
Thesis Advisor

Steven R. Ramp
Second Reader/Co-Advisor

Mary L. Batteen
Chairman, Department of Oceanography

THIS PAGE INTENTIONALLY LEFT BLANK

ABSTRACT

The use of the HF radar to measure and map surface currents has proliferated along the coastlines of many countries for purposes of Search and Rescue, Oil Spill Management, Oceanographic and Fishery Science studies. In the US Navy, these surface current maps are being evaluated for operational use in real-time data assimilating coastal circulation models, and direct monitoring tools in environmentally sensitive operating areas.

The SeaSonde HF radar, a DF system, was considered in this study. It uses the MUSIC algorithm to recover bearings from the Doppler backscatter spectrum of the sea surface. By varying the radial and antenna patterns, the simulated backscatter spectra were passed through the SeaSonde software suite for radial pattern recovery. This unprecedented approach directly evaluated SeaSonde's MUSIC, and the associated uncertainties were examined against the simulated inputs of (1) fixed amplitude and phase deviations from the ideal antenna pattern, (2) measured antenna patterns and (3) decreasing SNR.

It was found that using the measured antenna pattern to recover radials yielded least uncertainty, but a definitive prediction of MUSIC's radial-recovery capability in relation to the pattern's complex amplitude and phase structure remained illusive. The results highlighted the need to calibrate the military's DF-systems for accurate azimuth recovery.

THIS PAGE INTENTIONALLY LEFT BLANK

TABLE OF CONTENTS

I.	INTRODUCTION.....	1
	A. USING HIGH FREQUENCY RADAR FOR SURFACE CURRENT MAPPING	1
	B. RECOVERY OF SURFACE CURRENT PATTERN BY THE SEASONDE HF RADAR.....	2
	C. EVALUATING MUSIC THROUGH SIMULATIONS.....	3
	D. ORGANIZATION	6
II.	SET-UP FOR SIMULATIONS	9
	A. CONCEPT OF SIMULATIONS	9
	B. OPERATION OF SEASONDE SUITE	9
	1. Spectra Generation	10
	a. <i>SPECTRA Smoothing Technique</i>	10
	2. Radial Pattern Recovery	11
	a. <i>Identification and Localization of Bragg Peaks</i>	11
	b. <i>Recovery of Radial Velocities</i>	12
	c. <i>Recovery of Bearings</i>	13
	d. <i>Recovery by Antenna Patterns</i>	13
	e. <i>Compiling Temporary Radial Pattern Files</i>	16
	f. <i>Compiling Output Radial Pattern Files</i>	16
	3. Illustration of Spectra Generation and Radial Recovery.....	16
	C. SPECTRA GENERATOR AND ITS INPUTS	17
	1. Simulation Sites.....	18
	a. <i>Additional Computed Parameters from Header File</i>	18
	2. Mean Received Power (Bragg) Pattern.....	19
	3. Radial Current Pattern	20
	a. <i>Adjustment to Current Limits</i>	22
	4. Receive Antenna Pattern.....	22
	D. SPECTRA GENERATOR OUTPUT	24
	E. MODIFICATIONS TO SEASONDE SUITE’S HEADER FILE TO RECOVER RADIALS FROM SIMULATED SPECTRA	25
	1. Localizing Simulated Bragg Peaks	25
	2. Limitations of Localization Method	28
	a. <i>Noise-Added Currents in Scenarios</i>	28
	b. <i>User Defined and Constant Localizing Parameters</i>	29
	c. <i>Misaligned Indices Representing Limits of Recovered and Known Bragg Peaks</i>	31
	F. SIMULATION OBJECTIVES	33
	G. SCENARIO CREATION AND PERFORMANCE MEASUREMENT ...	33

III.	SCENARIO 1 SERIES: VALIDATING MEASURED VS THEORETICAL PATTERN RESULTS	35
A.	SCENARIO 1 SERIES	35
B.	RESULTS	36
	1. Scenario 1A.....	36
	2. Scenario 1B.....	38
	3. Scenario 1C.....	40
C.	DISCUSSION OF RESULTS	41
	1. Recovery by Measured Antenna Pattern Yields Better Results....	41
	2. Amplitude Deviations Had Greater Effect on MUSIC.....	41
	3. Phase Corrections Required For Recovery by Idealized Antenna Pattern.....	42
	4. “Gaps” in Recovered Radial Velocity Pattern	42
IV.	SCENARIO 2 SERIES: EXPLORING MUSIC’S LIMITATIONS DUE TO CURRENT AND MEASURED ANTENNA PATTERN CHARACTERISTICS.....	43
A.	SCENARIO 2 SERIES	43
B.	RESULTS	45
	1. Scenario 2A.....	45
	<i>a. RMS Errors Increase with Radial Pattern Complexity</i>	<i>48</i>
	<i>b. Inconsistent Coherence of RMS Errors and SD_SeaSonde</i>	<i>48</i>
	<i>c. Systematic Error Bias</i>	<i>48</i>
	2. Scenario 2B.....	49
	3. Scenario 2C.....	51
	<i>a. RMS Errors Increases with Radial Pattern Complexity.....</i>	<i>53</i>
	<i>b. Inconsistent Coherence of RMS Errors and SD_SeaSonde</i>	<i>53</i>
	<i>c. Systematic Error Bias</i>	<i>53</i>
	<i>d. Correlation of RMS Errors with Measured Antenna Pattern Structure.....</i>	<i>53</i>
	<i>e. “Gaps” in Recovered Radial Velocity Patterns.....</i>	<i>55</i>
	4. Scenario 2D.....	56
	<i>a. RMS Errors Increases with Radial Pattern Complexity.....</i>	<i>58</i>
	<i>b. Incoherence of RMS Errors and SD_SeaSonde.....</i>	<i>58</i>
	<i>c. Systematic Error Bias</i>	<i>58</i>
	<i>d. Correlation of RMS Errors with Measured Antenna Pattern Structure.....</i>	<i>58</i>
	<i>e. “Gaps” in Recovered Radial Velocity Patterns.....</i>	<i>60</i>

5.	Scenario 2E	61
a.	<i>RMS Errors Increases with Radial Pattern Complexity</i>	63
b.	<i>Incoherence of RMS Errors and SD_SeaSonde</i>	63
c.	<i>Systematic Error Bias</i>	63
d.	<i>Correlation of RMS Errors with Measured Antenna Pattern Structure</i>	63
e.	<i>“Gaps” in Recovered Radial Velocity Patterns</i>	63
C.	DISCUSSION OF RESULTS	65
1.	RMS Errors Increases with Radial Pattern Complexity, Amplitude Deviations and Poorer Velocity Resolution.....	65
2.	General Incoherence of RMS Error and SD_SeaSonde.....	65
3.	Systematic Error Bias.....	66
4.	Inconsistent Correlation of RMS Errors with Measured Antenna Pattern Structure.....	66
5.	“Gaps” in Recovered Radial Velocity Patterns.....	66
V.	SCENARIO 3 SERIES: RECOVERING RADIALS UNDER VARYING SNR.....	69
A.	SCENARIO 3 SERIES	69
B.	SNR EQUATION.....	69
1.	Estimates of Range-Independent Parameters	70
a.	<i>Average Transmitter Power Output (P_t)</i>	70
b.	<i>Transmit Antenna Power-Gain Over Earth, Including Ground Losses (G_t)</i>	70
c.	<i>Cable Losses to Transmit Antenna (L_c)</i>	71
d.	<i>Receive Antenna Directive Gain, Excluding Ground Losses (D_r)</i>	71
e.	<i>Radar Wavelength (λ)</i>	71
f.	<i>Normalized Radar Cross Section (σ^o):</i>	71
g.	<i>Atmospheric Noise Factor (F_a)</i>	71
h.	<i>Integration Time (τ_i)</i>	71
i.	<i>Internal Receiver Noise Per Unit Bandwidth at Operating Temperature (kT_o)</i>	71
2.	Estimates of Range-Dependent Parameters	72
a.	<i>Range to the specified radar scattering cell (R)</i>	72
b.	<i>Area Inside a Radar Range Cell (ΔA)</i>	72
c.	<i>One-way Attenuation Factor above Normal Free-Space Spreading Loss (F)</i>	72
C.	HF NOISE.....	73
D.	SCENARIO 3 SIMULATION MATRIX.....	76

E.	RESULTS	78
1.	Scenario 3A.....	78
a.	<i>Drowning of Bragg Peaks.</i>	<i>81</i>
b.	<i>Abrupt Decrease of Coverage Density.....</i>	<i>81</i>
c.	<i>Better Performance from Measured Antenna Patterns.....</i>	<i>81</i>
d.	<i>Biased Error Results by Ideal Antenna Pattern</i>	<i>82</i>
2.	Scenario 3B.....	83
a.	<i>Drowning of Bragg Peaks.</i>	<i>86</i>
b.	<i>Abrupt Decrease of Coverage Density.....</i>	<i>86</i>
c.	<i>Better Performance from Measured Antenna Patterns.....</i>	<i>86</i>
d.	<i>Biased Error Results by Ideal Antenna Pattern</i>	<i>87</i>
F.	DISCUSSION OF RESULTS	87
1.	Maximum, Operational and Optimal Range of SeaSonde.....	88
2.	Results from Measured Antenna Patterns	88
3.	Power-Law Relation of RMS Errors to SNR	88
4.	Biased Error Results by Ideal Antenna Pattern	89
VI.	CONCLUSIONS	91
A.	SIMULATION PROCEDURE	91
B.	SUMMARY OF RESULTS	91
C.	APPLICATIONS	93
D.	FUTURE WORK TO IMPROVE BEARING ACCURACY	94
1.	Antenna Design	94
2.	Adaptive Settings Adjustment	94
3.	Hybrid Resolution Processing.....	95
4.	Hybrid Radial Processing.....	95
5.	“Research Mode” for SeaSonde Suite.....	95
	LIST OF REFERENCES	97
	INITIAL DISTRIBUTION LIST	103

LIST OF FIGURES

Figure 1.	Spectra Generation and Radial Recovery Cycle of the SeaSonde HF Radar ..10
Figure 2.	Amplitude of (A) Ideal Antenna Pattern and (B) Distorted Antenna Pattern with Antennae Loop 1 and 2 in Red and Blue, Respectively and Loop 1 Orientation in Orange14
Figure 3.	Illustration of the Composition of Spectral Files to Generate a Radial File Based on Default Radial Output Parameters17
Figure 4.	Approaching (Blue Solid) and Receding (Red Dash-Dot) Bragg Patterns as Computed for Simulated Sites – (A) DUMY, (B) MLNG and (C) PPIN ...20
Figure 5.	Single- and Dual-Solution Radial Current Patterns (Left and Right Panels Respectively) with Gaussian Noise of Standard Deviation 5 cm/s for (A) DUMY, (B) MLNG and (C) PPIN21
Figure 6.	Antenna Amplitude Pattern for DUMY Site (Loop 1 in Red, Loop 2 in Blue and Loop 1 Orientation in Orange) – (A) Meas1 and Meas2 (Both have Amplitude Characteristics of Ideal); and (B) Meas3 (Squished by factor 2).....23
Figure 7.	Antenna Phase Pattern for DUMY Site (Loop 1 in Red Dash-Dot and Loop 2 in Blue Solid) – (A) Meas1 and Meas3 (Both have 0° phase shift); and (B) Meas2 (Phase-shifted by +90°).....23
Figure 8.	Antenna Amplitude Pattern for (A) MLNG and (B) PPIN.....24
Figure 9.	Antenna Phase Pattern for (A) MLNG and (B) PPIN.....24
Figure 10.	Example of (A) Partially and (B) Optimally Localized Bragg Peaks (Bounded between Two Magenta Lines) Based on Different Header Parameters on the Same Spectra File Using the Calibration Process27
Figure 11.	Incomplete Isolation of Bragg Peaks (Bounded Between Magenta Lines) for Spectra Generated by (A) Single- and (B) Dual-Solution Radial Current Regimes with No Current Noise Input29
Figure 12.	Instance of Fully and Partially Localized Bragg Peaks (Bounded by Magenta Lines) Based on the Same Localization Parameters30
Figure 13.	Computed and Recovered Indicial Limits Representing the Bragg Peaks (Bounded by Magenta Lines) of a Given Spectral File32
Figure 14.	Scenario Matrix for Scenario 1 Series, with Inputs for Both the CSSim_mod and SeaSonde Suite35
Figure 15.	Mean Simulated (Blue Line) Versus Recovered (Red Circles) Radial Current Patterns by Ideal (A1 and B1) and Meas1 (A2 and B2) Antenna Patterns of Single- and Dual-Solution Current Regimes (Left and Right Panels Respectively).....37
Figure 16.	Mean Simulated (Blue Line) Versus Recovered (Red Circles) Radial Current Patterns by Ideal without Phase Corrections (A1 and B1), Ideal with Phase Corrections (A2 and B2), and Meas3 (A3 and B3) Antenna Patterns of Single- and Dual-Solution Current Regimes (Left and Right Panels Respectively).....39

Figure 17.	Mean Simulated (Blue Line) Versus Recovered (Red Circles) Radial Current Patterns by Ideal (A1 and B1) and Meas3 (A2 and B2) Antenna Patterns of Single- and Dual-Solution Current Regimes (Left and Right Panels Respectively).....	40
Figure 18.	Scenario Matrix for Scenario 2 Series, with Inputs for Both the CSSim_mod and SeaSonde Suite	44
Figure 19.	Recovered 28 1-Hour Ensembles of Radial Velocity Errors (A1 and B1) Map and SD_SeaSonde (A2 and B2) by Meas1 of Single- and Dual-Solution Current Regimes (Left and Right Panels), Respectively.....	45
Figure 20.	(A) RMS Velocity Error and (B) Average SD_SeaSonde Computed Along Bearings for Radial Ensembles Recovered by Meas1 for Single- and Dual-Solution Current Regimes (Blue Dash-Circle and Red Dash-Diamond, Respectively).....	47
Figure 21.	Recovered 28 1-Hour Ensembles of Radial Velocity Errors (A1 and B1) Map and SD_SeaSonde (A2 and B2) by Meas2 of Single- and Dual-Solution Current Regimes (Left and Right Panels), Respectively.....	49
Figure 22.	(A) RMS Velocity Error and (B) Average SD_SeaSonde Computed Along Bearings for Radial Ensembles Recovered by Meas2 for Single- and Dual-Solution Current Regimes (Blue Dash-Circle and Red Dash-Diamond, Respectively).....	50
Figure 23.	Recovered 28 1-Hour Ensembles of Radial Velocity Errors (A1 and B1) Map and SD_SeaSonde (A2 and B2) by Meas3 of Single- and Dual-Solution Current Regimes (Left and Right Panels), Respectively.....	51
Figure 24.	(A) RMS Velocity Error and (B) Average SD_SeaSonde Computed Along Bearings for Radial Ensembles Recovered by Meas3 for Single- and Dual-Solution Current Regimes (Blue Dash-Circle and Red Dash-Diamond, Respectively).....	52
Figure 25.	Meas3 Vs Ideal (A) Antenna Amplitude, (B) Self-Pattern Antenna Amplitude Ratio, (C) Cross-Pattern Antenna Amplitude Ratio and (D) Cross-Pattern Antenna Phase Ratio	54
Figure 26.	Recovered 28 1-Hour Ensembles of Radial Velocity Errors (A1 and B1) Map and SD_SeaSonde (A2 and B2) by MLNG Measured Antenna Pattern of Single- and Dual-Solution Current Regimes (Left and Right Panels) Respectively	56
Figure 27.	(A) RMS Velocity Error and (B) SD_SeaSonde Computed Along Bearings for Radial Ensembles Recovered by MLNG Measured Antenna Pattern for Single- and Dual-Solution Current Regimes (Blue Dash-Circle and Red Dash-Diamond, Respectively).....	57
Figure 28.	MLNG Measured Antenna Pattern Vs Ideal (A) Antenna Amplitude, (B) Antenna Phase, (C) Self-Antenna Amplitude Ratio, (D) Self-Pattern Phase Ratio, (E) Cross-Pattttern Amplitude Ratio and (F) Cross-Pattern Phase Ratio.....	59

Figure 29.	Recovered 28 1-Hour Ensembles of Radial Velocity Errors (A1 and B1) Map and SD_SeaSonde (A2 and B2) by PPIN Measured Antenna Pattern of Single- and Dual-Solution Current Regimes (Left and Right Panels), Respectively	61
Figure 30.	(A) RMS Velocity Error and (B) SD_SeaSonde Computed Along Bearings for Radial Ensembles Recovered by PPIN Measured Antenna Pattern for Single- and Dual-Solution Current Regimes (Blue Dash-Circle and Red Dash-Diamond, Respectively).....	62
Figure 31.	PPIN Measured Antenna Pattern Vs Ideal (A) Antenna Amplitude, (B) Antenna Phase, (C) Self-Antenna Amplitude Ratio, (D) Self-Pattern Phase Ratio, (E) Cross-Pattern Amplitude Ratio and (F) Cross-Pattern Phase Ratio.....	64
Figure 32.	Computed Signal-to-Noise Ratio for MLNG (solid blue) and PPIN (red dash-dot)	73
Figure 33.	Simulated Self-Spectra of (A) MLNG and (B) PPIN with SNR Corresponding to Range Cell 4.....	75
Figure 34.	Scenario Matrix for Scenario 3 Series, with Inputs for Both the CSSim_mod and SeaSonde Suite	77
Figure 35.	Velocity Error Maps Recovered by Measured Pattern (A1 and B1), Ideal Pattern with Phase Corrections from CrossLoopPatterner Tool (A2 and B2), and Ideal Pattern with Phase Corrections from Stats-Diag File (A3 and B3) at each Range Cell for Single- and Dual-Current Regimes (Left and Right Panels)	79
Figure 36.	RMS Errors (A1 and B1) and Coverage Densities (A2 and B2) Recovered by the Antenna Patterns: Measured (blue solid line with circle), Ideal with Diag-Stats Phase Corrections (black dash-dot line with triangle), and Ideal with CrossLoopPatterner Phase Corrections (red dash-line with diamond) at each Range Cell for Single- and Dual-Current Regimes (Left and Right Panels).....	80
Figure 37.	Simulation Results (Blue '+' and Red 'x') and Lines of Best Fit (Blue Dash-Dot and Red Dash) Corresponding to the Single- and Dual-Solution Current Regimes, Respectively Compared with the Bearing Uncertainty Power-Law Relation.	82
Figure 38.	Velocity Error Maps Recovered by Measured Pattern (A1 and B1), Ideal Pattern with Phase Corrections from CrossLoopPatterner Tool (A2 and B2), and Ideal Pattern with Phase Corrections from Stats-Diag File (A3 and B3) at each Range Cell for Single- and Dual-Current Regimes (Left and Right Panels).....	84
Figure 39.	RMS Errors (A1 and B1) and Coverage Densities (A2 and B2) Recovered by the Antenna Patterns: Measured (blue solid line with circle), Ideal with Diag-Stats Phase Corrections (black dash-dot line with triangle), and Ideal with CrossLoopPatterner Phase Corrections (red dash-line with diamond) at each Range Cell for Single- and Dual-Current Regimes (Left and Right Panels).....	85

Figure 40. Data Points (Blue '+' and Red 'x') and Lines of Best Fit (Blue Dash-Dot and Red Dash) Corresponding to the Single- and Dual-Solution Current Regimes Respectively Compared with the Bearing Uncertainty Power-Law Relation.....87

LIST OF TABLES

Table 1.	Actions Performed on Monopole Self-Spectrum Based on the Header Parameters.....	11
Table 2.	Actions Performed on Positive and Negative Parts of the Monopole's Self-Spectrum Based on the Header Parameters	12
Table 3.	Parameters Read by Spectra Generator.....	18
Table 4.	Relevant Header File Parameters for Each Site to Optimally Localize the Bragg Peaks	26
Table 5.	Comparison of Computed and Recovered Indices Representing the Receding the Approaching Bragg Peaks.....	31
Table 6.	Summary of RMS Differences Between Simulated and Recovered Radial Velocities from Scenario 1 Series.....	41
Table 7.	Summary of RMS Errors Recovered by Scenarios 2 Series.....	65

THIS PAGE INTENTIONALLY LEFT BLANK

ACKNOWLEDGMENTS

This work would not have been possible without the wholehearted support from many people. First, I would like to express my sincere appreciation to my thesis advisor, Professor Jeffrey D. Paduan, and the second reader, Professor Steven R. Ramp. Their experience and expertise in the subject matter, directions and patience, enabled me to complete this thesis. In particular, Professor Paduan's guidance broadened my horizon on the applications of the HF radar in the coastal areas and fueled my interest in this research area.

Next, special thanks are extended to Dan Atwater and Mike S. Cook for their technical advice regarding SeaSonde operation and MATLAB programming. They were instrumental in helping me jumpstart on this study, and condensing my learning curve of the SeaSonde system so that I can complete this study in nine months. Also, I would like to thank the CODAR Ocean Systems, in particular, its Chief Executive Officer, Professor Don E. Barrick, who graciously ran a code whose output was crucial in one part of the study; as well as Bill Rector, whose prompt clarifications to my questions on the SeaSonde system, enabled me to forge ahead in my simulations without interruptions. In addition, I want to express gratitude to Professor David C. Jenn, a renowned antenna design expert in the Naval Postgraduate School, who graciously provided some invaluable literature which was useful in this study, even though I was not his student. Also, I am grateful to the wonderful participants of the Fifth Radiowave Oceanography Workshop (ROW-5), many of whom, are pioneers and experts in the field of radiowave oceanography, and whose works inspired my study of the HF radar.

My stint at the Naval Postgraduate School had been a most pleasant, memorable and rewarding experience in my military career and I have to thank both the school and the Republic of Singapore Navy. I am also grateful to the staff and students at the Oceanography Department, especially the Chairperson, Professor Mary L. Batteen, who helped me, assimilate into an intellectually challenging yet stimulating academic environment.

Last but not least, I reserve my final appreciation to my wife and son, and family members in Singapore, who had provided the physical, emotional and spiritual support during my endeavor for academic excellence. Without them, this work would not have achieved its goals and be considered for an award by the school.

To these people, I offer my sincerest and heartfelt gratitude.

I. INTRODUCTION

A. USING HIGH FREQUENCY RADAR FOR SURFACE CURRENT MAPPING

The theory behind the operation of the High Frequency (HF) radar to measure surface currents have been well established since Crombie's (1955) discovery of resonant backscatter of electromagnetic waves by the sea surface waves. Since then, the use of the HF radar to map coastal surface currents has proliferated in many countries, e.g. Australia, Germany, Japan, USA, etc., for purposes of Search and Rescue, Oil Spill Management, Oceanographic and fishery science studies. Examples of HF radars include the Coastal Ocean Dynamics Application Radar (CODAR; Barrick et al., 1977), Ocean Surface Current Radar (OSCR; Hammond et al., 1987), Wellen Radar (WERA; Gurgel et al., 1999) and SeaSonde radar (Barrick et al., 1994). The reader is encouraged to refer to Gurgel, Essen & Kingsley (1999) which gives a good overview of the developments of HF radars. In the Navy context, real-time surface current maps from HF radar systems are being evaluated for operational use in data assimilating coastal circulation models, as well as for direct monitoring tools in environmentally sensitive operating areas. An extension of the land-based siting option, which is presently under testing, includes installation onboard slowly moving ships.

A single radar unit measures the radial component of the surface currents and, when combined with the radial pattern from another radar, sited in a favorable position to minimize the geometrical dilution of precision, a complete current vector is described. Therefore, the radials need to be spatially resolved in range and azimuth. Two techniques are used to segregate the return signals into range bins or cells, including short pulse edge detection as in the case of the OSCR system or linear Frequency-Modulated, Continuous-Wave (FMCW) chirps, as in the case of the WERA, and SeaSonde systems. In both cases, the horizontal resolution or width of a range cell is an inversely related to the bandwidth of the transmitted HF signal. Two methods to resolve the azimuth have been developed: beam-forming or direction-finding (DF). The former uses large antenna arrays to shape and steer a set of narrow beams along specific bearings while the latter floodlights the coverage area and recovers the azimuth of the backscattered signals using

some kind of element-to-element comparison algorithm, which in the case of the CODAR systems, is proprietary. The OSCAR and WERA are beam-forming systems while the CODAR and SeaSonde are DF. The WERA has the advantage of being configured as either a beam-forming or DF system.

First-order Bragg peaks are produced from the resonant return (or Bragg scattering) of radar signals by surface waves corresponding to half the transmitted wavelength (also referred as Bragg waves). Radial currents are measured from the Doppler shift of the measured Bragg signal from the Bragg frequency, which is related to the phase speed of the Bragg waves traveling in still water. Coupled into the spectrum are the second-order signals, caused by the backscatter returns of non-resonant surface waves, from which significant wave height, dominant wave direction and period are extracted (Lipa & Nyden, 2005).

B. RECOVERY OF SURFACE CURRENT PATTERN BY THE SEASONDE HF RADAR

Only the SeaSonde DF system, produced by CODAR Ocean Sensors (COS), is studied in this paper. It has a compact receiver, comprising a monopole and two orthogonally mounted crossed-loop antennae, is used in conjunction with a transmitter, placed at the immediate vicinity of the receiver. Thus the system has a very small footprint compared to beam forming systems, and hence particularly suited at coastal areas which have competing demands for residential, commercial and nature conservatism purposes. So far, the SeaSonde system has been successfully deployed near to or on top of coastal installations, e.g. lighthouses, coastal observatories, etc. Therefore, it is well poised to be a major player in the Surface Current Mapping Initiative (SCMI) to monitor coastal currents along the USA's coastlines (Paduan et al., 2004).

Being a DF system, radial velocity recovery is straightforward – it is directly related to the Doppler shift of the Bragg signals from the known Bragg frequency of the backscatter spectrum. On the other hand, bearing recovery is more challenged; SeaSonde employs the Multiple Signal Classification (MUSIC; Schmidt, 1986) algorithm to first separate the noise from the signals and then performs a search function to determine the latter's direction of arrival within the antennae's coverage pattern. As the algorithm has

two degrees of freedom (one less than the total number of antennae), it suffers from bearing discrimination when the same signal is received at more than two distinct bearings.

To quantify MUSIC-derived current mapping performance, a two-pronged approach had generally been adopted: conducting field experiments and comparing statistical differences between the results from the HF radar against in-situ current measurement instruments (Emery et al., 2004; Kohut et al., 2005; Paduan et al., 2005); or conducting simulation studies where MUSIC recovers the radial current patterns from simulated backscatter spectrum (Barrick & Lipa, 1999; Laws et al., 1998; Fernandez et al., 1999; Laws, 2001; Glenn et al., 2004). While the benefits of the former approach cannot be entirely discounted, proponents of the simulation approach cited costs, testing inefficiency, resource intensiveness and data mismatch in the nature of measurement, and differences in the spatial and temporal averaging scales, as motivations for simulation studies.

In both approaches, evidence of angular bias was detected whilst recovering the radial pattern using the theoretical ideal pattern. This bias was reduced when the measured antenna pattern was used in a field experiments (Emery & Washburn, 1998; Paduan et al., 2005) and simulations (Barrick & Lipa, 1999; Glenn et al., 2004). Subsequent studies used the measured antenna pattern as the primary source for recovering radials for analysis. However, in a field experiment conducted by Paduan et al. (2005), angular shifts were detected even when using the measured pattern, albeit smaller than from the ideal pattern. The pointing errors recovered by MUSIC also varied along the angular coverage of the radar site, faring worse along certain bearings to the errors recovered by the ideal pattern. This variability in lieu of the antenna and radial current patterns thus warranted further studies.

C. EVALUATING MUSIC THROUGH SIMULATIONS

In this case, a simulation-based effort is desirable because a simulated radial current can be used as the “ground-truth” to evaluate the radial current recovered by MUSIC, using a specific antenna pattern. Therefore, external and variable “noise” due to the environment and measuring instruments are eliminated to definitively assess MUSIC’s performance.

Simulations to study and quantify MUSIC's performance started off with using theoretical idealized antenna pattern to recover radial patterns from spectra generated by single- and dual-solution current regimes. These current regimes tested the validity of MUSIC's theoretical bearing discrimination capability, given its inherent two degrees of freedom. These current profiles were later adjusted to yield an abrupt feature to simulate a current front, and challenge MUSIC's ability to resolve a three-solution regime (Barrick & Lipa, 1996; Laws et al., 1998; Fernandez et al., 1999; Laws, 2001). More recently, Glenn et al. (2004) simulations used measured antenna patterns. In all the above, the Root-Mean-Square (RMS) difference (or errors) of the recovered from the simulated radials was a proven measure of performance for quantitative analysis.

In these previous attempts, it is believed that a self-coded MUSIC algorithm was used to recover bearings from the simulated spectral files. In this study, an unprecedented approach of using SeaSonde's organic MUSIC algorithm was adopted. This provided a more realistic and user-oriented approach to validate MUSIC's performance, but it presented a different challenge as the program was not designed for research purposes and several "get-arounds" were required to optimally localize the Bragg peaks. These "get-arounds" also exposed certain limitations associated with the header and option files used by the program to isolate the first-order Bragg peaks.

A COS-supplied MATLAB code was modified to generate an array of spectral files from a combination of currents and distorted antenna patterns. In fact, actual measured patterns from the Moss Landing (MLNG) and Point Pinos (PPIN) HF-radar sites in the Monterey Bay were also used. Other inputs to the spectra generator were held constant. These spectral files were then passed through the SeaSonde's radial current recovery suite and its results compared with the inputted radial pattern.

Three scenario series were designed to systematically test and evaluate SeaSonde's MUSIC algorithm. The first scenario series, designated as Scenario 1, used measured patterns, which essentially are variants of an idealized pattern applied with a constant phase or amplitude deviation, towards radial pattern recovery. The results were compared with recovery by the ideal pattern, accompanied with phase corrections, when applicable. Consistent with previous studies, recovery by the measured patterns gave the

best results, followed by the theoretical patterns, with phase-corrections when applicable. The latter supported COS's founders who have counseled that phase corrections are important to correct radials recovery. This scenario also suggested that amplitude deviations degraded MUSIC's performance more than phase deviations.

Scenario 2 series used a large ensemble of spectral files to explore MUSIC's ability to recover radial vectors in relation to the measured antenna pattern, first using variants of the idealized pattern, and then using MLNG's and PPIN's measured patterns. Results culled from using the variants indicated that amplitude deviation affected MUSIC more than phase deviations. Large velocity uncertainties also coincided with large deviations of the measured pattern from the ideal. However, any relation of recovered velocity uncertainties to the character of MLNG's and PPIN's actual patterns was not apparent, due to their more complicated amplitude and phase structure. The distribution of these uncertainties did not necessarily coincide with the standard deviations of the recovered radials (henceforth referred as SD_SeaSonde), suggesting that the latter which is used by SeaSonde may not be a good flag for erroneous radials. Other than the measured pattern's deviations from the ideal which caused gaps in the recovered radial pattern, results from this scenario series also alluded to higher operating radar frequencies as another likely source.

Scenario 3 series was designed to explore MUSIC's ability to recover the radials from simulated spectra with range-sensitive Signal-to-Noise Ratio (SNR) and frequency-dependent noise floor, using the MLNG (a mid-band SeaSonde) and PPIN (a low-band SeaSonde) measured and ideal antenna patterns. Under the simulated conditions, the maximum range where a radial vector could be recovered compared favorably with COS's designed range for the SeaSonde. However, this range would be lower in the field due to the simulation's limitations. For instance, second-order effects were not simulated, the presence of a complex surface current pattern was not included, and a different physical condition giving rise to a different SNR was not considered. Due to the attenuating SNR, the coverage density of the recovered radials also decreased gradually up to a threshold range where it dropped drastically to less than 50%. This range may be defined as the operational range, which the simulations revealed, was about 6 to 10 km less than the maximum range. Though lower RMS errors were generally recovered from

the measured patterns, there were nevertheless, occasions when it fared worse than the ideal pattern. The simulations revealed that this occurred when the SNRs were approximately less than 15 dB and 20 dB for the mid- and low-band SeaSondes respectively. Finally, the power-law relation of the RMS errors to SNR was attempted, with reasonable curves fitting the data points at higher SNRs. However, due to the limited data points available, a consistent power-law relation was not achieved.

D. ORGANIZATION

Chapter I introduces the HF radar's ability to map surface currents and attention is drawn to the SeaSonde HF system, which uses the MUSIC algorithm to DF the radial currents. A simulation approach is then proposed to evaluate the SeaSonde's surface current mapping performance.

Chapter II outlines the spectra generation and radial recovery cycle of the SeaSonde system. Subsequently, it discusses the process and limitations of integrating the spectra simulator, which generates the simulated backscatter spectrum, with the SeaSonde software suite to recover the radial currents. Finally, the simulation objectives and methodology, as well as a quantitative means to measure MUSIC's performance, are discussed.

Chapter III describes the first of three scenario series, graduated in complexity, to evaluate MUSIC's performance in recovering a single- and dual-solution current pattern. Scenario 1 was a testbed to validate the integration of the spectra generator with the SeaSonde suite. It also set out to explore the contributions of measured antenna patterns, with fixed phase or amplitude deviations from the idealized pattern, in the radial pattern recovery process.

Chapter IV then explores the relationship of MUSIC's performance to the measured antenna pattern by averaging a long time-series of radials. First, the measured patterns used in Scenario 1 (with fixed phase or amplitude deviations) are used to generate the spectra and recover these radials. Thereafter, actual patterns from MLNG and PPIN are used to explore the interactions of phase and amplitude deviations in the radial recovery process.

Chapter V wraps up the series of scenarios by assessing SeaSonde's performance in recovering the radial vectors in a realistic attenuating SNR condition in the presence of a HF noise floor. Actual antenna patterns from MLNG and PPIN are used to generate the spectra and recover the radials using both the measured and ideal antenna patterns. An attempt to define the operational and optimal range of the HF radar is attempted.

Finally, Chapter VI summarizes results culled from the entire series of studies and outlines how the findings apply to HF radar applications in a civilian and military context. Finally, the scope for future research is discussed.

THIS PAGE INTENTIONALLY LEFT BLANK

II. SET-UP FOR SIMULATIONS

A. CONCEPT OF SIMULATIONS

A set of known input parameters which represented ground-truth, e.g. frequency, wind, radial current and antenna patterns, were used to generate the spectral files. These files were passed to the SeaSonde Suite to recover the radial patterns and any resulting pattern deviations were used to measure the performance of the MUSIC algorithm.

First of all, this chapter shall describe how SeaSonde Suite generates the spectral files and recover the radial current patterns. Subsequently, the simulator's input parameters, the mechanics of the spectra generator and how its output is integrated with the suite, and the procedure to set-up the latter to process these files are elaborated. Finally, the simulation objectives, scenario creating methodology and the means to measure MUSIC's performance are discussed.

B. OPERATION OF SEASONDE SUITE

The SeaSonde software suite generates the spectra from the voltage signals received by the three antenna elements and subsequently recovers the radial patterns through its implemented MUSIC algorithm (COS, 2004a). The spectra generation and radial recovery cycle is illustrated in Figure 1.

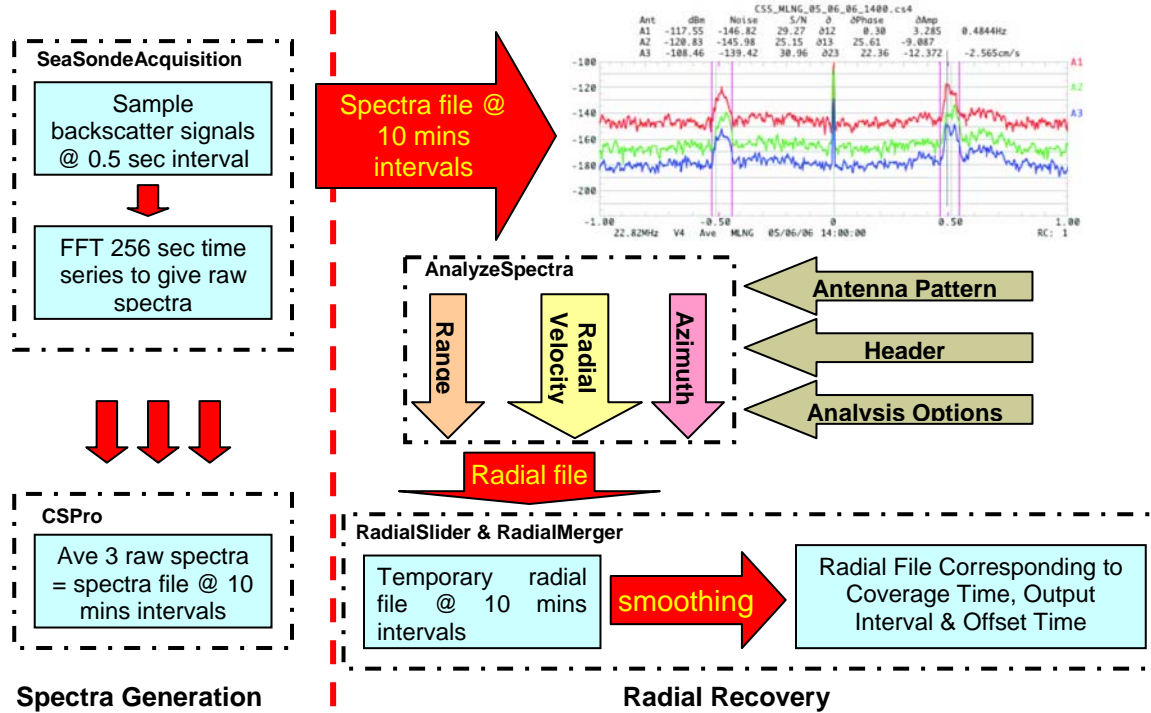


Figure 1. Spectra Generation and Radial Recovery Cycle of the SeaSonde HF Radar

1. Spectra Generation

The spectra generation portion comprises the **SeaSondeAcquisition** which samples the backscatter signals from the surface currents at a rate of 0.5 sec. The linear FMCW chirp modulation employed by the SeaSonde separates the backscatter signals according to range. After acquiring a time series of 256 sec, the signals are FFTed into 512 bins and 0 Hz-centered, to produce the raw spectra for each range cell. The **CSPro** module then reads and smooths every three blocks of raw spectra (representing an averaging of backscatter signals totaling $3 \times 256 = 12.8$ mins) to output a spectra file time stamped at 10 mins intervals. These files are then saved into the SpectraToProcess folder.

a. SPECTRA Smoothing Technique

The SeaSonde employs a unique averaging or smoothing process when generating the spectral files. It re-uses the last raw spectra block used by the previous spectra file and combines it with the subsequent two blocks of raw spectra for the next

spectra file. According to CODAR, this operation replicates a “smoothing factor over time” which prevents sharp signal changes in successive spectral files.

2. Radial Pattern Recovery

The **AnalyzeSpectra** then processes these spectral files and extracts the range, azimuth and radial component of the surface currents. These are stored in temporary radial files at 10 mins intervals, and once the **RadialSlider** tool determines that a sufficient number of temporary radials are recovered (as determined by line 21 of the header file, i.e. coverage time, output interval and offset time), they are merged by the **RadialMerger** tool to produce the final radial for that output period.

a. Identification and Localization of Bragg Peaks

The first step of the radial current recovery process is the identification and localization of the first-order Bragg peaks from the Doppler spectrum, which is controlled by the parameters in the header file (COS, 2004b; 2004c).

Summarized in Table 1 are the operations carried out in a chronological order on the monopole’s self-spectrum in accordance with the relevant header parameters. The noise floor is identified and a threshold is applied on the spectra. The signals above the noise floor are then smoothed and checked if second-order components are to be processed (in this case, this was turned off).

Steps	Line No. / Parameter No.	Name / Default Value	Operation
A1	Line 15, Parameter 2	Noise Factor / 4	Thresholds the signal at 4 times the noise floor
A2	Line 11, Parameter 2	Doppler Smoothing / 2	Apply a running mean of 2 points to identify nulls between first- and second- order spectra components
A3	Line 12, Parameter 2	Second Order / 0	Indicates the presence of second-order components, which in our case is set to 0

Table 1. Actions Performed on Monopole Self-Spectrum Based on the Header Parameters

Subsequently, the maxima for each of the positive and negative parts of the monopole's self-spectrum are identified and any parts of the signal which are between factors of 7.5 and 15 (default values) down from the maxima are isolated as the Bragg peaks. The peaks are processed by MUSIC and any currents greater than the user-defined expected maximum current are filtered out. Table 2 summarizes the actions performed, vis-à-vis the relevant header parameters.

Steps	Line No. / Parameter No.	Name / Default Value	Operation
B1	Line 15, Parameter 1	Factor Down Peak Nulls / 7.5	Isolates the first-order components at 7.5 times down from the maxima
B2	Line 12, Parameter 1	Factor Down Peak Limit / 15	Eliminates the part of the spectrum which is 15 times lower than the maxima
B3	Line 11, Parameter 1	Maximum Current / 100	Accepts recovered radial currents at less than 100 cm/s

Table 2. Actions Performed on Positive and Negative Parts of the Monopole's Self-Spectrum Based on the Header Parameters

The indices representing the first-order Bragg peaks from the monopole self-spectrum are then used to recover the radial velocities and associated bearings.

b. Recovery of Radial Velocities

As a DF system, recovering the radial velocity is straightforward as it is related to the frequency displacement from the Bragg frequency (f_{Bragg} ; Hz), which in turn, is related to the still water phase speed of the Bragg waves as determined by the deep water dispersion relation:

$$f_{Bragg} = \sqrt{\frac{gf}{c\pi}} \quad (1)$$

Furthermore, for a given transmit centre frequency f , the velocity step size for each index increment or velocity resolution (ΔV_r ; cm/s) is given by:

$$\Delta V_r = \frac{c}{512f} \times 100 \quad (2)$$

Therefore, the recovered radial velocity (V_{rd}) is computed from the i -th displacement from the index representing the Bragg frequency (i_{Bragg}) as follows:

$$V_{rd} = (i - i_{Bragg}) \times \Delta V_r \quad (3)$$

c. Recovery of Bearings

On the other hand, directional recovery is more involved and many algorithms have been developed to accomplish it, ranging from the simple arctangent method of the two normalized cross-loop signals (Kohut & Glenn, 2003) to the least squares method (Lipa and Barrick, 1983). More recently, CODAR has adopted a more robust algorithm, called MUltiple SIgnal Classification (MUSIC; Schmidt, 1986; Barrick et al., 1994), used primarily by the military's DF systems for Signal Intelligence (SIGINT) purposes, for SeaSonde's bearing recovery. The method exploits the property that for any incoherent source, the signal and noise subspaces can be extracted from the eigenstructure of the covariance matrix. A search function is then formed from these subspaces, which produces peaks corresponding to the signal's direction of arrivals. As incoherent sources are retrieved from three receive antenna elements in the SeaSonde configuration, this algorithm is able to, in theory, discern up to two bearing directions of arrivals for a given recovered radial velocity (Barrick and Lipa, 1996).

d. Recovery by Antenna Patterns

To aid the search function in locating the signal's direction of arrival, the site's antenna pattern is required by the MUSIC algorithm. In the present configuration, the directions of arrival are discretized in 5° intervals, which suggests that any antenna pattern measurements should be resolved to, at least, the same angular increments.

The SeaSonde’s three-element receiver antenna system comprises two orthogonally mounted cross-loop antennas and a whip (or monopole). Being a vertically polarized radar system, each loop produces a ‘figure-8’ pattern which follows a cosine function while the monopole produces an omnidirectional pattern at the horizon (Barrick & Lipa, 1996). These idealized or theoretical patterns, however, may be distorted in amplitudes and phases, by near-field features like posts, buildings, metal fences, trees, power lines, terrain or inadequate isolation of the antenna’s feedlines (Barrick & Lipa, 1996; 1999). Figure 2 shows the amplitude of an ideal and distorted antenna pattern with Loop 1 and 2 in red and blue, respectively and oriented such that Loop 1 is indicated in orange.

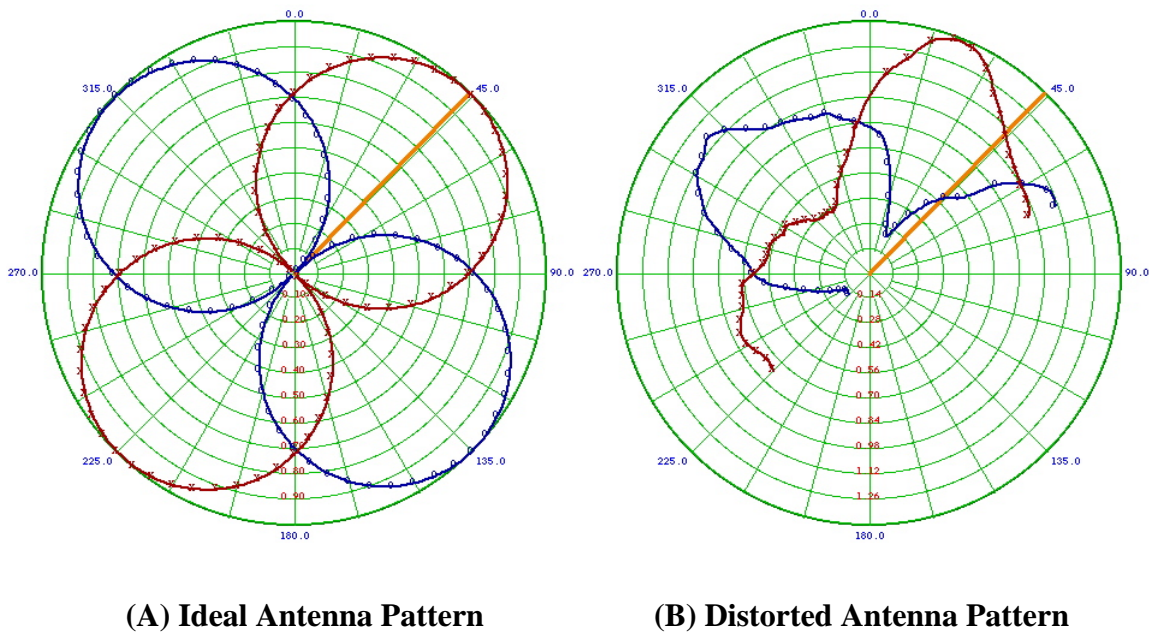


Figure 2. Amplitude of (A) Ideal Antenna Pattern and (B) Distorted Antenna Pattern with Antennae Loop 1 and 2 in Red and Blue, Respectively and Loop 1 Orientation in Orange

Distortions due to mutual antenna coupling (Derneryd & Kristensson, 2004) are discounted because of SeaSonde’s design symmetry and orthogonality (Barrick & Lipa, 1996). Hence, pattern measurements for each operational radar site were performed and normalized against the monopole’s pattern. These distorted or measured

patterns are usually stable over time (as long as the near-field environment remains constant) as observed by Paduan et al. (2005) and Glenn et al. (2004).

The SeaSonde Suite may use the theoretical idealized and/or measured antenna patterns, as determined by the AnalysisOptions file, to recover the radial patterns:

(1) Recovery by Ideal Pattern. This option is exercised when the measured pattern is not available or invalid, or simply to compare the radial patterns recovered by the different antenna patterns. The Ideal pattern is aligned with the orientation of the cross-loop antenna designated as Loop 1, and the radial patterns are recovered after applying phase corrections and an azimuth filter via the Phases.txt and AngSeg.txt files.

Two means of phase inputs are generally adopted: from the CrossLoopPatterner which computes the phase of the site's measured pattern (if available) or from the Statistics-Diagnostics (Stats-Diag) file which consolidates the signal statistics and other diagnostic parameters captured during the radial recovery process. The phases from the latter are then averaged and input into the Phases.txt file for subsequent batches of incoming spectral files.

As the idealized pattern has 360° coverage, radials outside the site's angular coverage may be recovered. The COS software package uses the AngSeg.txt file to filter out these stray radials, but they also can serve as a diagnostic related to MUSIC's performance, if desired.

(2) Recovery by Measured Pattern. This is the preferred modus operandi as previous field investigations by Emery & Washburn (1998) and Paduan et. al (2005) have shown to have the least measurement biases, which was substantiated by simulations by Barrick & Lipa (1999). Furthermore, the measured pattern best represents the effects of antenna pattern distortions caused by near-field features as described earlier. Using the measured patterns does not require any phase corrections nor angular filtering as these are integrated into the coverage of the pattern itself.

e. Compiling Temporary Radial Pattern Files

The recovered bearings and velocities are computed from both the approaching and receding Bragg peaks for each range cell. The radial velocities are averaged and SD_SeaSonde computed along each recovered bearings. They are then stored in a temporary radial file which is maintained by the **RadialSlider** module.

f. Compiling Output Radial Pattern Files

Each spectral file, time stamped at 10 mins intervals, undergoes the above processes (a) to (d) to produce the temporary radial files. Thereafter, as determined by line 21 of the header file (which dictates the coverage, output interval and offset), the **RadialMerger** module merges these files to produce the output radial file for that period. Like the temporary radial file, the output radial file stores the averaged radial velocity and SD_SeaSonde along each recovered azimuth for each range cell. The latter is also used by SeaSonde to flag potential erroneous radials.

3. Illustration of Spectra Generation and Radial Recovery

As an illustration, assume that a radial output is desired at 1000 hrs, with the parameters in line 21 of the Header file set at default values, i.e. 75 mins coverage, 60 mins output intervals with 0 mins offset from the hour.

Recall that SeaSonde employs a “smoothing” technique when generating the spectral files which essentially re-uses the third raw spectra in the preceding spectra file as the first raw spectra in the next spectra file. Therefore, as shown on Figure 3, seven spectral files, centered on the hour, are required to produce seven temporary radial files which are merged to output a radial file for the default radial output parameters.

The details of the simulator input are as follows:

1. Simulation Sites

Three simulation sites were established: a Dummy (DUMY) which operates at 25 MHz to simulate a mid-band SeaSonde; and two operational sites in Moss Landing (MLNG) and Point Pinos (PPIN). The DUMY site had parameters which were consistent with actual ones, with sweep rate at 2 Hz, range cell depth of about 3 km and 180° area coverage. Details of the sites were contained in the header files which were accessed by both the spectra generator and the SeaSonde Suite. See Table 3 for the relevant parameters of the header files which were read by CSSim_mod to generate the spectral files.

Line No.	Line Name	Site Parameters		
1	Site Name	DUMY	MLNG	PPIN
3	Antenna Loop 1 Bearing	310	307	044
4	No. of Range Cells	1	28	28
	Distance to First Range Cell (km)	12.1282	3.03205	3.034
	Distance between Range Cells (km)	3.03205	3.03205	3.034
7	Operating Centre Frequency (MHz)	13 or 25	22.8	13.395281
9	Doppler Hz/Bin	0.003908526		

Table 3. Parameters Read by Spectra Generator

a. Additional Computed Parameters from Header File

The bandwidth (BW) and sweep rate frequency (SRF) were computed as they were required in the header of the spectra file:

$$\text{Bandwidth} = \frac{c}{\text{Distance Between Range Cells} \times 2} \tag{5}$$

$$\text{Sweep Rate Frequency} = \text{Round}(\text{Doppler Hz/Bin} \times 512) \tag{6}$$

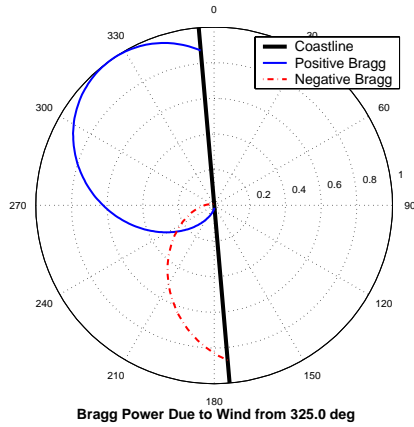
2. Mean Received Power (Bragg) Pattern

Mean received power pattern due to the approaching and receding Bragg waves (denoted by B_+ and B_- respectively) is found to follow a broad, cardioid pattern versus bearing (Barrick and Lipa, 1996). The approaching and receding power patterns gives rise to Bragg peaks at the positive and negative sides of the 0-centered backscatter spectrum respectively. The pattern is steered by the direction of the wind (θ_{wind}) and is given by:

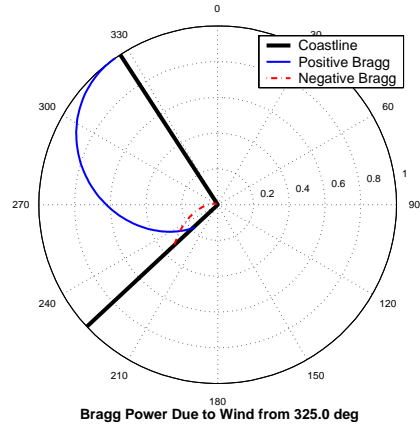
$$B_+ = \sqrt{\frac{\cos^4\left(\frac{\theta - \theta_{wind}}{2}\right) + 0.01}{1.01}} \quad (7)$$

$$B_- = \sqrt{\frac{\sin^4\left(\frac{\theta - \theta_{wind}}{2}\right) + 0.01}{1.01}} \quad (8)$$

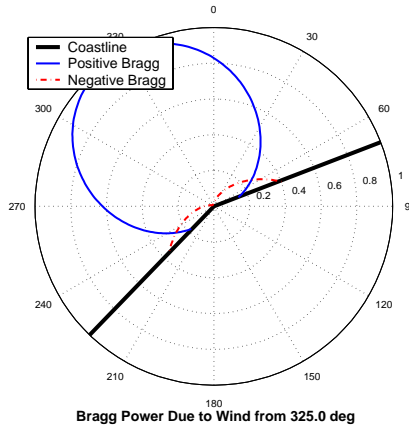
Figure 4 shows the computed approaching (blue solid) and receding (red dash-dot) Bragg Patterns due to θ_{wind} fixed at 325° for the DUMY, MLNG and PPIN sites.



(A) DUMY Bragg Pattern



(B) MLNG Bragg Pattern



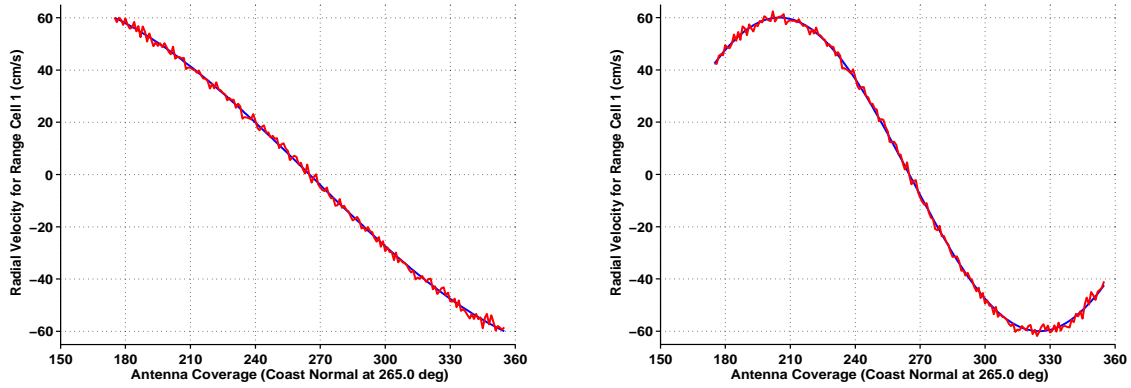
(C) PPIN Bragg Pattern

Figure 4. Approaching (Blue Solid) and Receding (Red Dash-Dot) Bragg Patterns as Computed for Simulated Sites – (A) DUMY, (B) MLNG and (C) PPIN

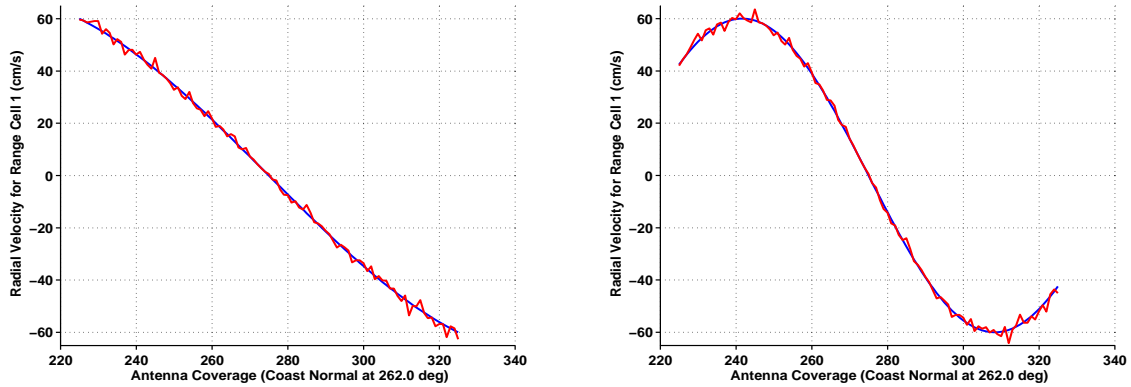
3. Radial Current Pattern

The radial current velocities as a function of bearings were used to simulate the current pattern. Two current regimes were generated: single- and dual-solution. A single-solution pattern had a one-to-one bearing to radial velocity relation while a dual-solution pattern had a two-to-one bearing to radial velocity relation at certain parts of the pattern. The limits of the current (without noise) were set at $\pm 60\text{cm/s}$ to produce a wider Bragg peak for processing. Figure 5 shows the single- and dual-solution radial patterns (left and right panels respectively), with Gaussian noise of standard deviations 5 cm/s, and scaled accordingly for the coverage of each site. If a horizontal line is drawn through

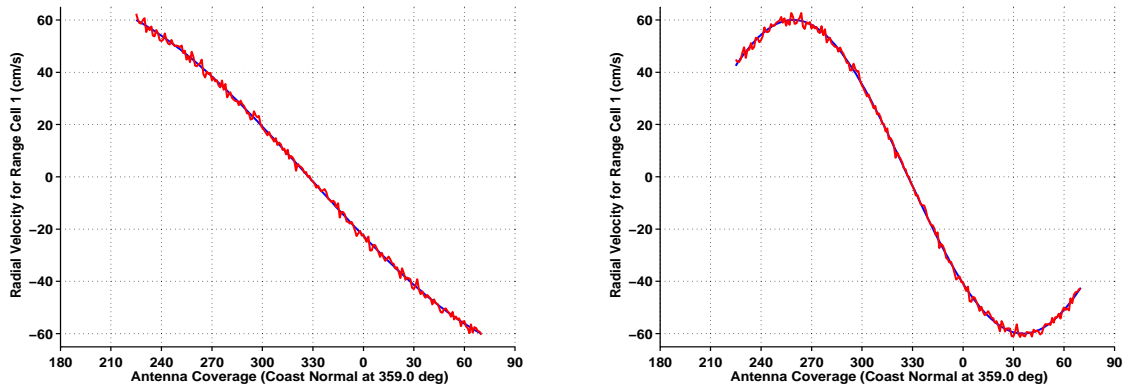
a radial velocity of 50 cm/s, a single-solution current pattern will yield a single bearing while a dual-solution will yield two bearings.



(A) DUMY Radial Current Patterns



(B) MLNG Radial Current Patterns



(C) PPIN Radial Current Patterns

Figure 5. Single- and Dual-Solution Radial Current Patterns (Left and Right Panels Respectively) with Gaussian Noise of Standard Deviation 5 cm/s for (A) DUMY, (B) MLNG and (C) PPIN

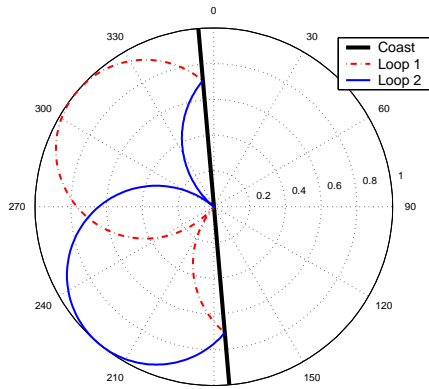
a. Adjustment to Current Limits

The software suite identifies the indices of the Doppler spectrum to recover the radial velocities and subsequently, the bearings. Therefore, it was essential to clip any noise-added current to prevent any “spill-over” to the adjacent index which will yield a higher radial speed and hence, recover an incorrect bearing. The limits of the noise-added current were thus clipped at the next higher speed step increment from ± 60 cm/s. For example, if the DUMY site operating at 25 MHz with velocity resolution of 2.342 cm/s had a noise-added current of 64 cm/s, it was clipped to 60.897 cm/s.

4. Receive Antenna Pattern

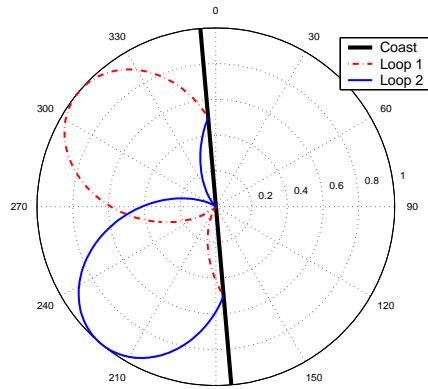
In this simulation study, antenna patterns at 1° resolution were used by the spectra generator to best replicate conditions for each site. The **CrossLoopPatterner** module in the SeaSonde Suite was used to either generate the idealized patterns or obtain phase information of the measured antenna patterns.

For the DUMY sites, variants of the “all-round” idealized pattern were generated to evaluate the effects of fixed phase and amplitude deviations to MUSIC’s performance. Meas1 was a truncated version of the ideal pattern, Meas2 was like Meas1 but phase shifted by $+90^\circ$ and Meas3 was like Meas1 but “squished” by a factor of two, in that the amplitude was modeled as a $\cos^2 \theta$ rather than $\cos \theta$. The amplitude and phase characteristics of the simulated antenna patterns are shown in Figure 6 and 7 respectively. The red line on both figures is due to the Loop 1 and the blue line is due to Loop 2.



Normalised Antenna Pattern with Coast Normal at 265.0 deg

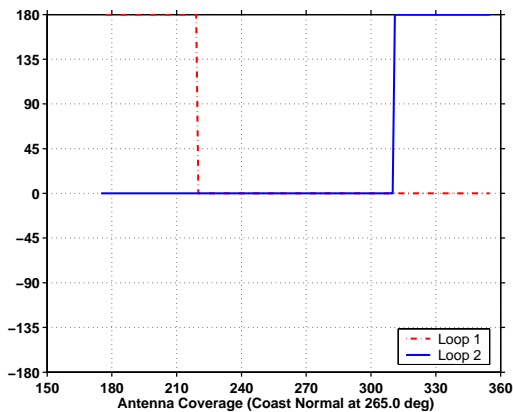
(A)



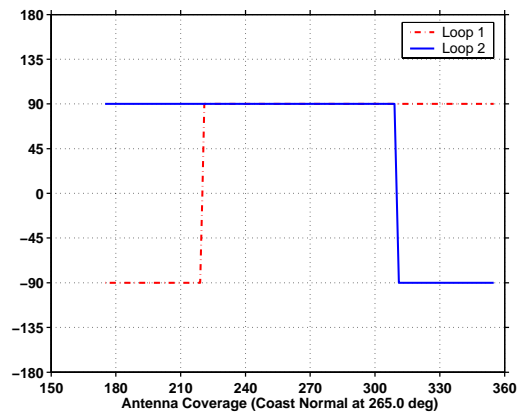
Normalised Antenna Pattern with Coast Normal at 265.0 deg

(B)

Figure 6. Antenna Amplitude Pattern for DUMMY Site (Loop 1 in Red, Loop 2 in Blue and Loop 1 Orientation in Orange) – (A) Meas1 and Meas2 (Both have Amplitude Characteristics of Ideal); and (B) Meas3 (Squished by factor 2)



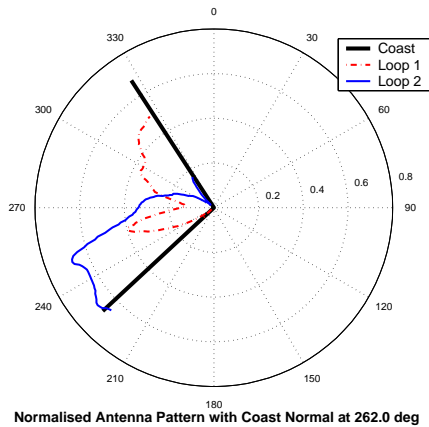
(A)



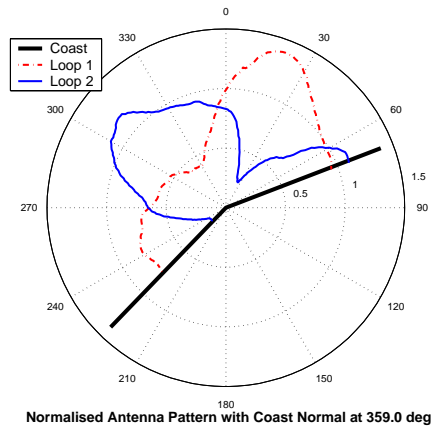
(B)

Figure 7. Antenna Phase Pattern for DUMMY Site (Loop 1 in Red Dash-Dot and Loop 2 in Blue Solid) – (A) Meas1 and Meas3 (Both have 0° phase shift); and (B) Meas2 (Phase-shifted by +90°)

Actual measured antenna patterns for the MLNG and PPIN sites were subsequently used. Figure 8 and 9 show the patterns' amplitude and phase characteristics respectively, with the same color convention as Figures 6 and 7. Evident from the patterns are the complex amplitude and phase variations unique to each site.

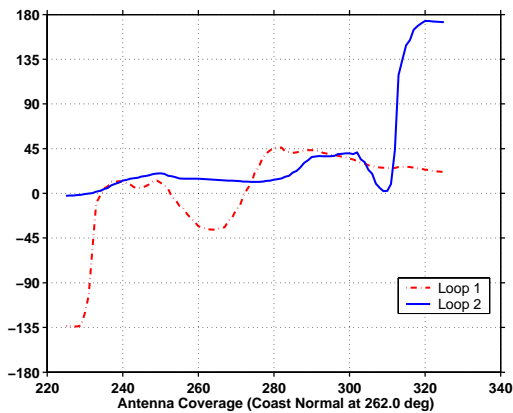


(A) MLNG

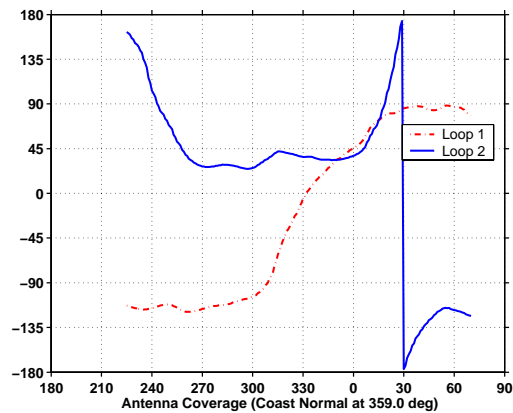


(B) PPIN

Figure 8. Antenna Amplitude Pattern for (A) MLNG and (B) PPIN



(A) MLNG



(B) PPIN

Figure 9. Antenna Phase Pattern for (A) MLNG and (B) PPIN

D. SPECTRA GENERATOR OUTPUT

The CSSim_mod takes the input parameters, as dictated by the simulated scenario, and mimics the **SeaSondeAcquisition** and **CSPPro** by generating the spectral files at 10 mins intervals. It is also capable of reading the parameters in line 21 of the header file to generate a series of spectral files which are “smoothed over time” by re-using the last raw spectra of the preceding spectra file as the first raw spectra of the succeeding spectra file (described earlier in Chapter II, Section B1a).

E. MODIFICATIONS TO SEASONDE SUITE'S HEADER FILE TO RECOVER RADIALS FROM SIMULATED SPECTRA

To recover the radial pattern from the spectra, the Bragg peaks must first be identified and localized. The current magnitude is a function of the Doppler shift of the peak from the Bragg frequency while the direction of the radial vector is recovered by MUSIC. Unlike simulation works by Barrick & Lipa (1996) and Laws (2001), who defined the limits of the Bragg peaks for processing by their self-coded MUSIC algorithm, using the SeaSonde suite required manipulations on a few parameters within the header file to optimally localize the Bragg peaks for subsequent radial pattern recovery. This procedure was fraught with limitations, which highlighted similar difficulties encountered in operational SeaSondes.

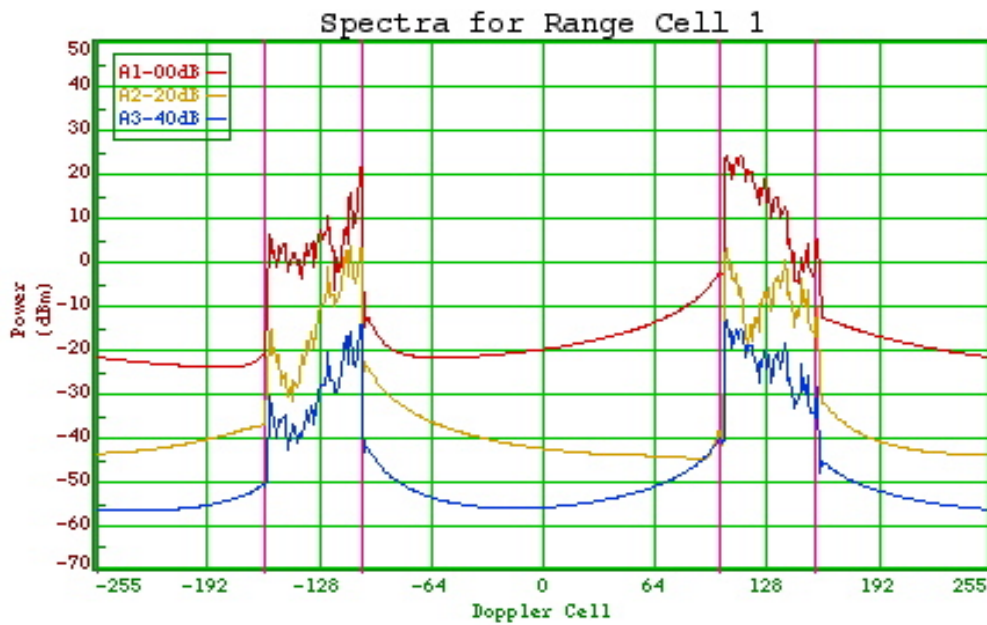
1. Localizing Simulated Bragg Peaks

In this study, the CSSim_mod emulated the **SeaSondeAcquisition** and **CSPro** by generating the simulated spectral file, which were manually transferred into the SpectraToProcess folder for processing. **AnalyzeSpectra** then proceeded to localize and process the Bragg peaks, via the parameters as mentioned in Section B of this chapter.

The **SpectraPlotterMap** module (part of SeaSonde Suite) was used to calibrate these parameters by using a 10 mins simulated spectra files for each site. The parameters listed in Table 4 were adjusted until the Bragg peaks are optimally isolated and saved in the respective site's header file.

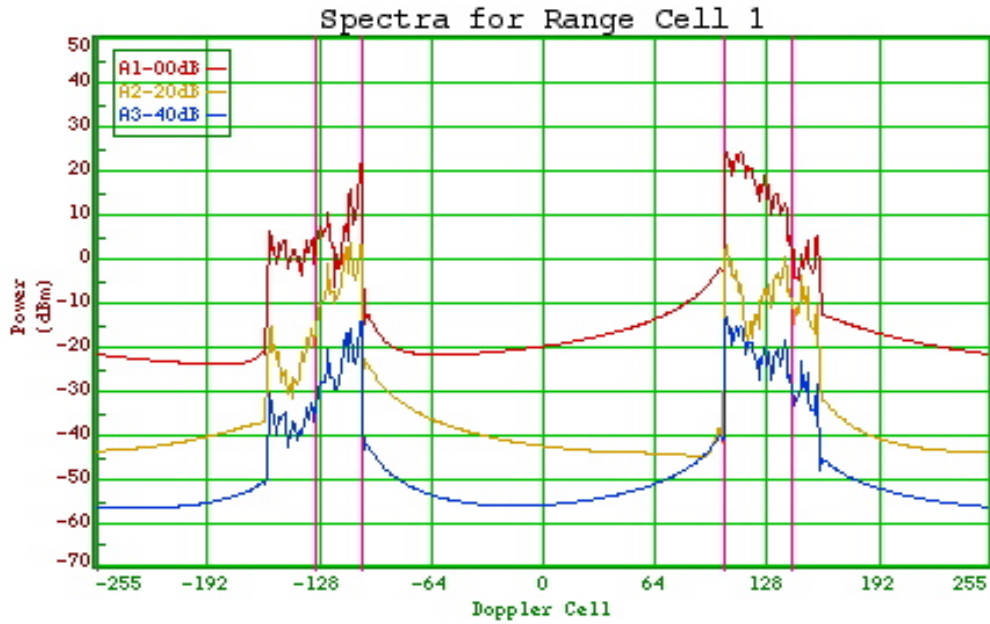
Line No. / Parameter No.	Name	DUMY	MLNG	PPIN
Line 11, Parameter 1	Maximum Current	61	62	62
Line 11, Parameter 2	Doppler Smoothing	2	2	2
Line 12, Parameter 1	Factor Down Peak Limit	478.6	151.4	239.9
Line 12, Parameter 2	Second Order	0	0	0
Line 15, Parameter 1	Factor Down Peak Nulls	478.6	151.4	239.9
Line 15, Parameter 2	Noise Factor	4.0	4.0	4.0

Table 4. Relevant Header File Parameters for Each Site to Optimally Localize the Bragg Peaks

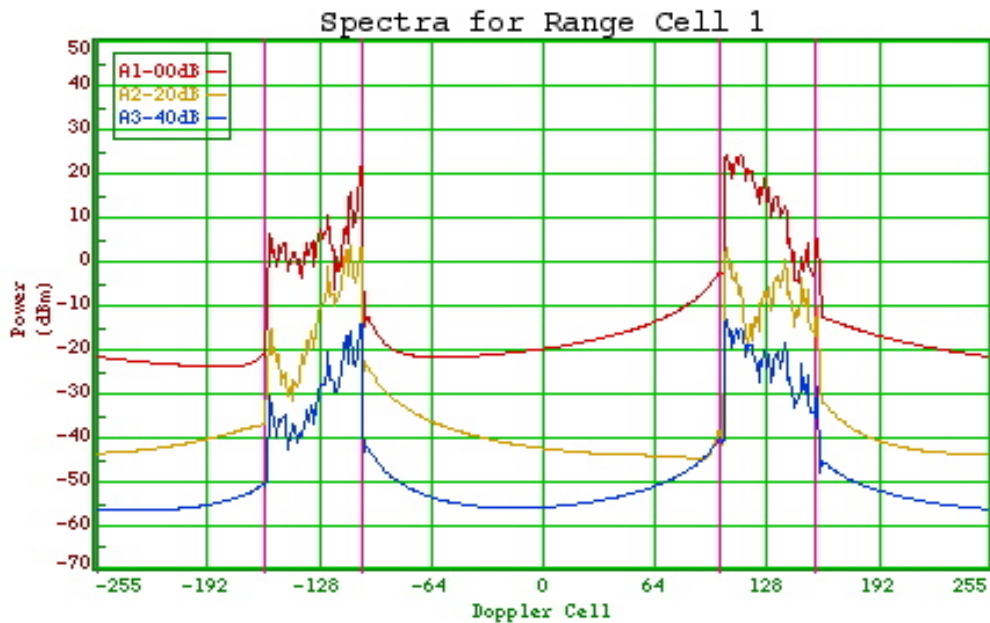


(B) Optimally Localised Bragg Peak

Figure 10 shows when the Bragg peaks, bounded between the two magenta solid lines, are partially and optimally localized during the calibration process. The latter is desired so that the assessment of SeaSonde's radial pattern recovery is unbiased.



(A) Partially Localised Bragg Peak



(B) Optimally Localised Bragg Peak

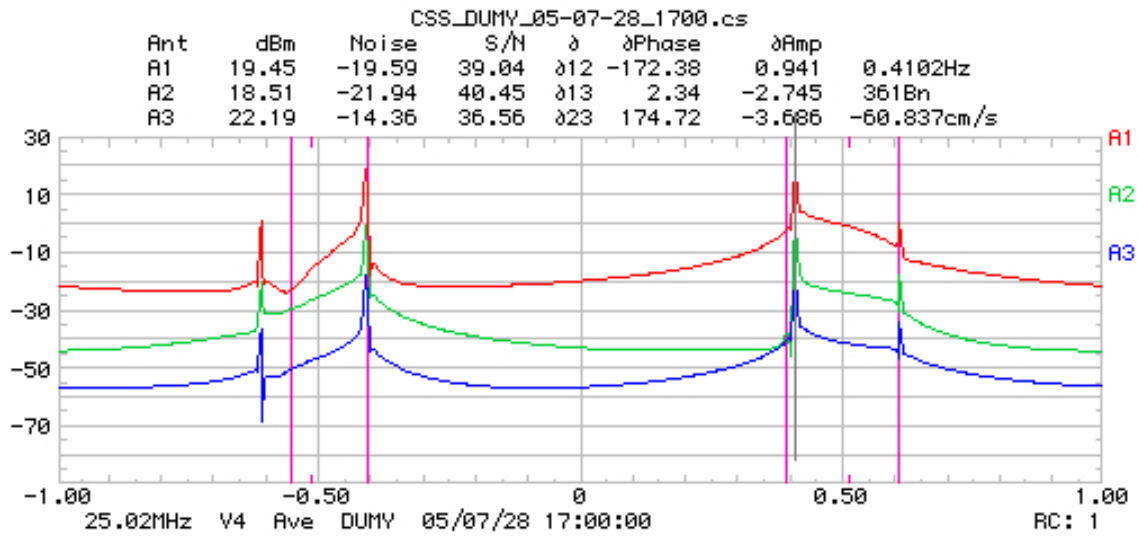
Figure 10. Example of (A) Partially and (B) Optimally Localized Bragg Peaks (Bounded between Two Magenta Lines) Based on Different Header Parameters on the Same Spectra File Using the Calibration Process

2. Limitations of Localization Method

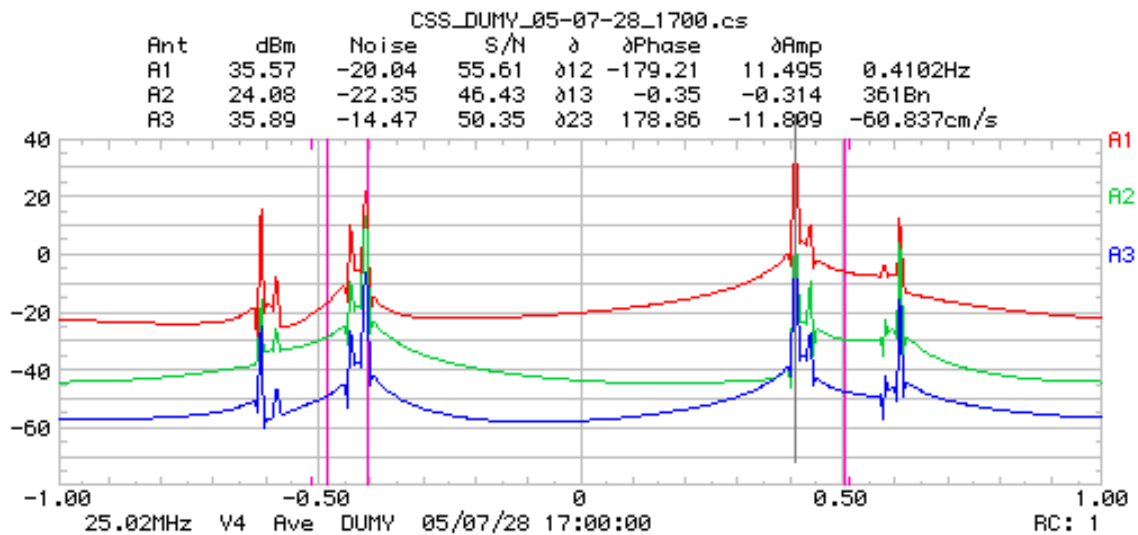
This localization method employed by SeaSonde to localize the Bragg peaks was practical but revealed the limitations in the choice of simulation scenarios, and the challenges in defining these parameters, particularly in operational SeaSondes, as discussed below:

a. Noise-Added Currents in Scenarios

Configuring CSSim_mod to generate the backscatter spectrum from currents with no noise was the obvious choice for this simulation. This would remove any temporal variability, and MUSIC would also yield a singular solution (Barrick & Lipa, 1996), which will facilitate subsequent error analysis. However, preliminary trials which involved passing this type of spectral files through the SeaSonde Suite were disappointing – only part of the Bragg peaks were isolated, hence giving incomplete Bragg region identification shown in Figure 11. However, when Gaussian noise was added to the radial pattern, isolation of the Bragg peaks were then possible, hence necessitating the addition of noise to the “clean” current input in the simulation scenarios.



(A) Single-Solution Radial Current Pattern with No Noise Input



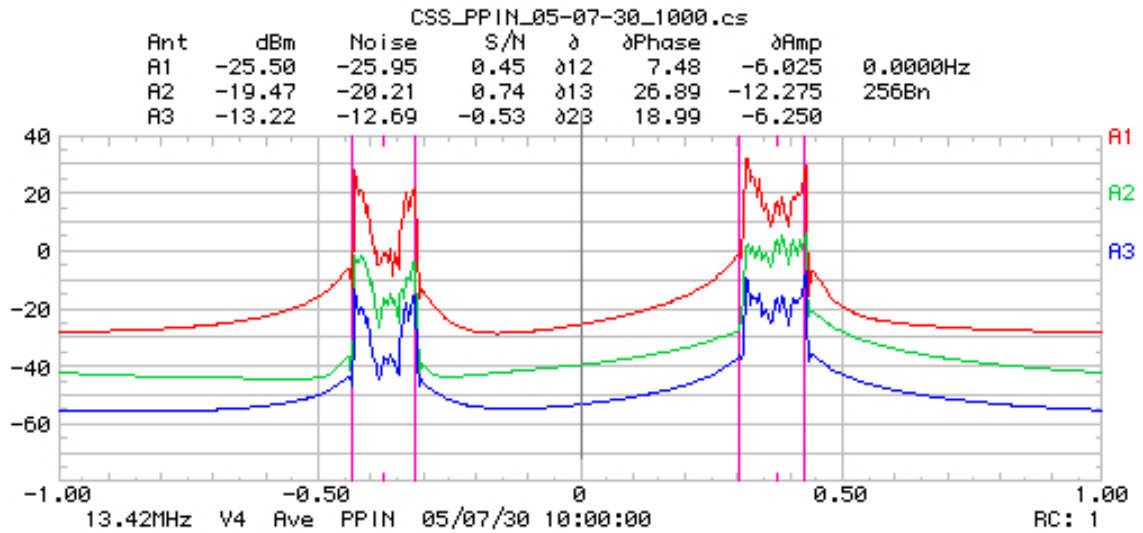
(B) Dual-Solution Radial Current Pattern with No Noise Input

Figure 11. Incomplete Isolation of Bragg Peaks (Bounded Between Magenta Lines) for Spectra Generated by (A) Single- and (B) Dual-Solution Radial Current Regimes with No Current Noise Input

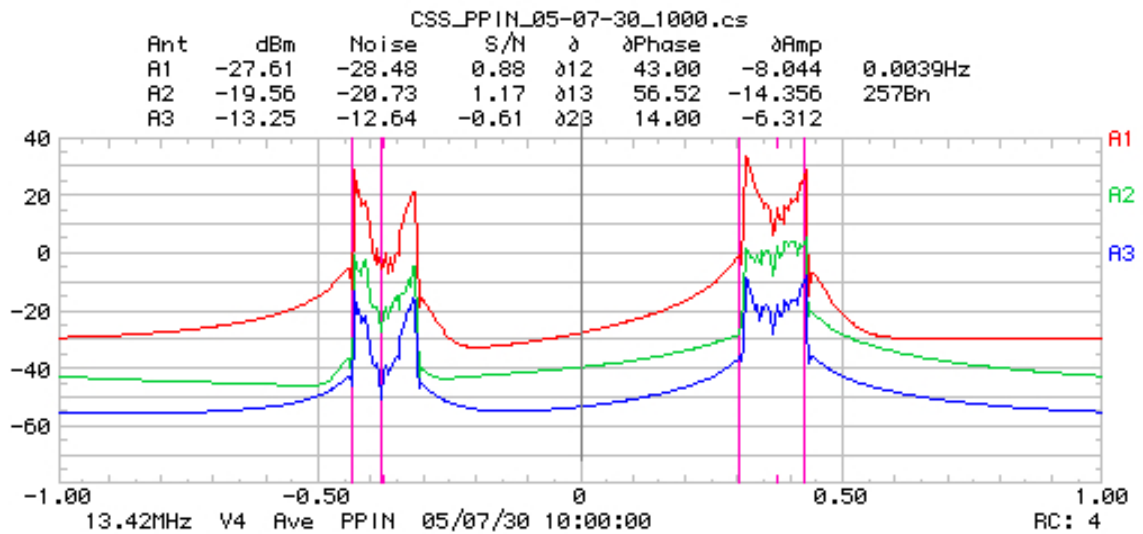
b. User Defined and Constant Localizing Parameters

A user was required to define the localizing parameters which were assumed applicable for all simulated spectral files. However, as the Bragg peaks vary due to varying conditions, both in real-life or simulated, these parameters may not be

robust nor effective. Figure 12 illustrates the optimal and partial localization of Bragg peaks, even though the same localizing parameters were used.



(A) Fully Localized Bragg Peaks



(B) Partially Localized Bragg Peaks

Figure 12. Instance of Fully and Partially Localized Bragg Peaks (Bounded by Magenta Lines) Based on the Same Localization Parameters

c. Misaligned Indices Representing Limits of Recovered and Known Bragg Peaks

The indices of the backscatter spectrum corresponding to the Bragg peaks were exactly determined as the noise-added current was deliberately clipped to avoid “spill-over” to the adjacent velocity bins. After much trial-and-error with **SpectraPlotterMap** to get the optimal parameters, there still remained a persistent misalignment of recovered indices from the computed ones. Tabulated below in Table 5 are the clipped current limits, and the limits of the computed and recovered indices of the receding and approaching Bragg peaks.

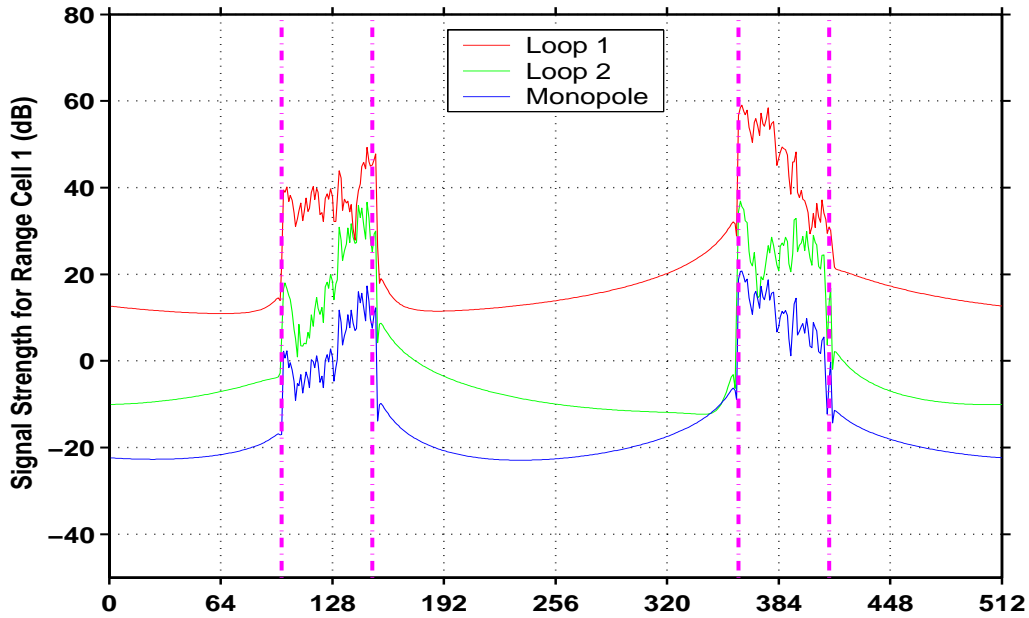
Simulation Input		Receding Bragg Peaks		Approaching Bragg Peaks	
Site	Clipped Current Limits (cm/s)	Computed Indices	Recovered Indices	Computed Indices	Recovered Indices
DUMY	± 60.897	[99, 151]	[97, 152]	[361, 413]	[357, 411]
MLNG	± 61.637	[107, 155]	[107, 156]	[357, 405]	[353, 404]
PPIN	± 60.634	[146, 174]	[144, 175]	[338, 366]	[333, 365]

Table 5. Comparison of Computed and Recovered Indices Representing the Receding the Approaching Bragg Peaks

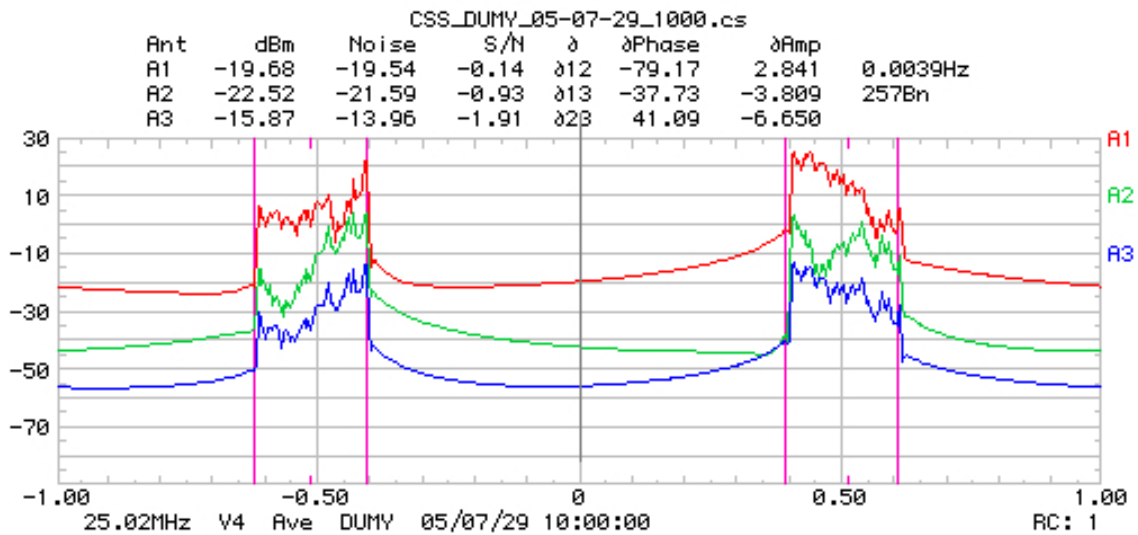
The table indicates a consistent and systematic misalignment of indices for all the sites. This implies that the SeaSonde suite processes part of the backscatter spectra outside the Bragg peaks, and thus recover spurious radials which is undesirable. This is however, mitigated by the selection of a maximum current parameter (header file, line 11, parameter 1) as mentioned in Section E1 of this chapter.

This indicial misalignment may be caused by different FFT and subsequent zero-centering algorithms implemented by MATLAB and SeaSonde. The latter suspicion was aroused as the centre of the backscatter spectrum were actually 255 and 256 (given that 512 spectra bins were generated), which may have caused discrepancies in assigning velocities to the indices. This misalignment may potentially cause a systematic error bias.

Figure 13 shows the actual and recovered indicial limits (bounded between the two magenta lines) of the Bragg peaks for a spectra generated by the DUMY site



(A) Computed Indicial Limits (Magenta Dash-Dot) of Bragg Peaks



(B) Indicial Limits of Bragg Peaks Identified by SeaSonde Suite

Figure 13. Computed and Recovered Indicial Limits Representing the Bragg Peaks (Bounded by Magenta Lines) of a Given Spectral File

F. SIMULATION OBJECTIVES

Arising from our understanding of SeaSonde's radial recovery process, and MUSIC's associated weakness to recover the same signals arriving from more than two bearings, it is obvious that any variability of MUSIC's performance stems from the radial current and antenna pattern characteristics. Therefore, this study set out the following objectives to better understand MUSIC's capabilities and limitations:

- To validate that radials recovered by the measured pattern are more accurate than from the theoretical pattern;
- To explore MUSIC's limitations, if any, of recovering radial patterns due to phase or amplitude deviations from the ideal pattern;
- To assess SeaSonde's performance in a realistic attenuating SNR environment.

G. SCENARIO CREATION AND PERFORMANCE MEASUREMENT

Since a noise-added current (which is consistent to actual current patterns) was used in the generation of the spectral files, radial pattern recovery was fraught with uncertainties (Lipa, 2003). To overcome temporal uncertainties, an ensemble of spectra was used to remove noise from the averaged radial pattern so as to evaluate MUSIC's performance.

Scenarios were created by fixing the wind direction and varying the radial current patterns (single- or dual-solutions) for each simulation site. These scenarios were translated to spectral files by the CSSim_mod, which were subsequently recovered by the suite, using the site's measured and Ideal patterns. The recovered and simulated radial patterns were then compared and the root-mean-square (RMS) errors computed and compared with the suite's computed SD_SeaSonde.

Three series of scenarios were formulated, each with the intent of fulfilling one of the above stated objectives. Details of the scenarios and their results will be revealed and discussed in the subsequent chapters.

THIS PAGE INTENTIONALLY LEFT BLANK

III. SCENARIO 1 SERIES: VALIDATING MEASURED VS THEORETICAL PATTERN RESULTS

A. SCENARIO 1 SERIES

To understand the contributions of phase and amplitude deviations from the idealized antenna pattern in the radial patterns recovery process, a series of scenarios involving systematic variations were designed for the DUMY site. The matrix of simulation scenarios for the DUMY site comprising the combinations of inputs to the spectra generator and the SeaSonde suite is shown in Figure 14. The scenarios were deliberately designed to accentuate errors induced by a single variant of the antenna pattern.

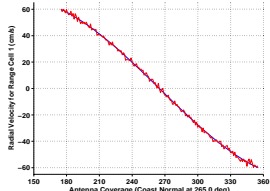
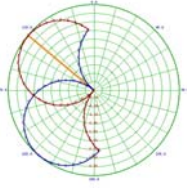
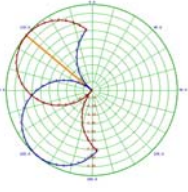
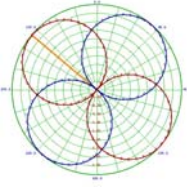
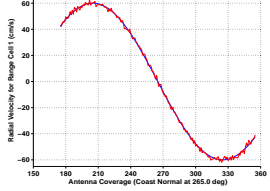
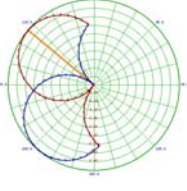
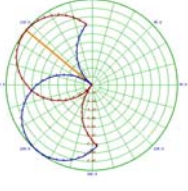
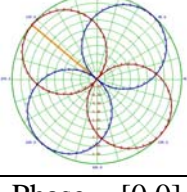
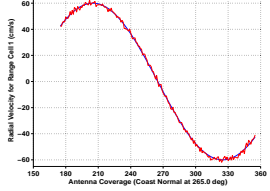
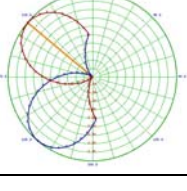
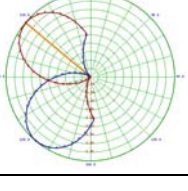
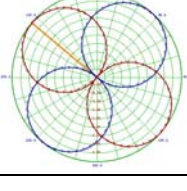
Scenario No.	Simulator Input		SeaSonde Recovery	
	Radial Patterns	Antenna Pattern (Amplitude)	Antenna Pattern (Amplitude)	Theoretical Pattern [Adjusted Phase Input]
1A		Meas1 	Meas1 	Phase = [0,0] 
1B	Or 	Meas2 	Meas2 	Phase = [0,0] and Phase = [90,90] 
1C		Meas3 	Meas3 	Phase = [0,0] 

Figure 14. Scenario Matrix for Scenario 1 Series, with Inputs for Both the CSSim_mod and SeaSonde Suite

In the above scenarios, the Meas1 (truncated Ideal pattern), Meas2 (phase shifted by $+90^\circ$) and Meas3 (amplitude “squished” by a factor of two) antenna patterns were each used to generate seven spectral files for Range Cell 1 from single- and dual-solutions radial patterns. These spectral files were then recovered as hourly radials by the SeaSonde suite, using both the measured and Ideal patterns. The latter was oriented with the cross-loop at 310° (indicated by yellow line) and appropriately corrected for phase.

The recovered radials were compared with the input radials and the RMS velocity error for the range cell was computed:

$$e_{rms}^j = \sqrt{\frac{\sum_i (V_{rcv}^i - V_r^i)^2}{m^j}} \quad (9)$$

- e_{rms}^j : rms error for range cell j
- V_{rcv}^i : radial velocity recovered at bearing i
- V_r^i : simulated radial velocity at bearing i
- m^j : total number of radial velocity recovered in range cell j

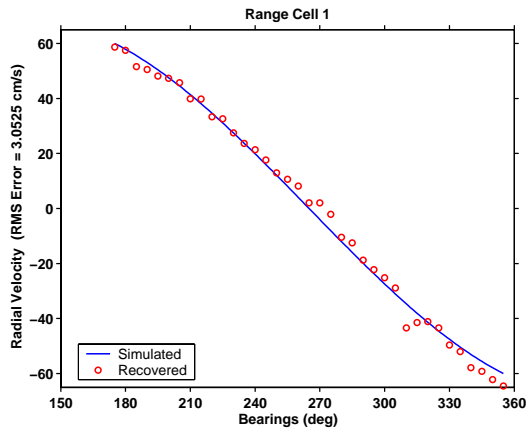
B. RESULTS

Results presented here in this section include plots of the input radial currents as a function of bearing (solid blue line) with overlaid recovered radial currents (red circles) for the different combinations of antenna patterns. In addition, RMS differences across the range cell are tabulated.

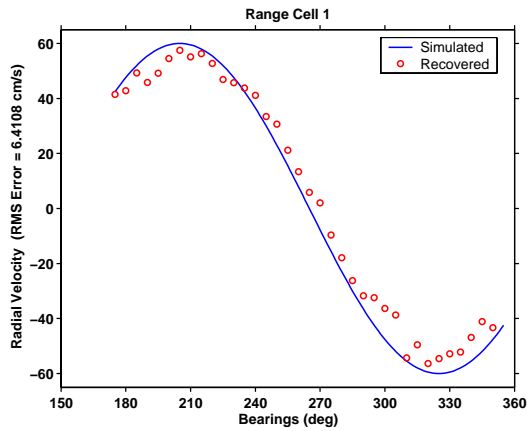
1. Scenario 1A

This scenario was created to serve as a benchmark for subsequent scenarios. The Meas1 pattern was used to generate seven spectral files to produce the hourly radials, recovered by Meas1 and the Ideal patterns. The default phase input of $[0,0]$ was applied. The left and right panels of Figure 15 show the mean single- and dual-solution simulated radial currents respectively, and recovered current patterns by the Meas1 and Ideal antenna patterns. In the single-solution case, the Meas1 and Ideal patterns yielded RMS errors of 2.9 cm/s and 3.0 cm/s respectively; and 5.4 cm/s and 6.4 cm/s respectively in the dual-solution case. It was obvious that MUSIC’s performance degraded by about a factor

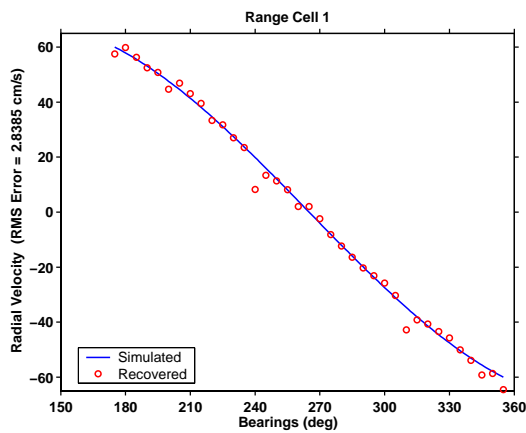
of two due to the dual-solution, which illustrated MUSIC's bearing discrimination limitations. This weakness also manifested in a similar SeaSonde-based simulation study by Barrick & Lipa (1996).



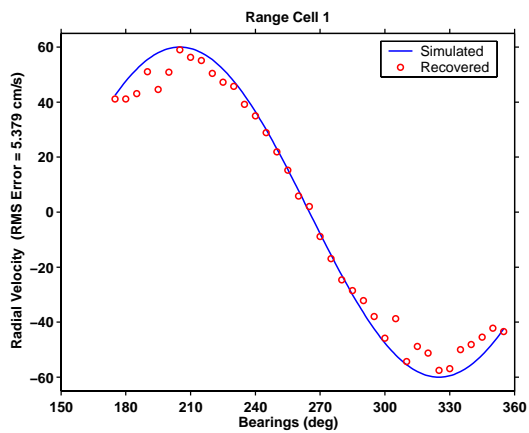
(A1) Recovered by Ideal



(B1) Recovered by Ideal



(A2) Recovered by Meas1

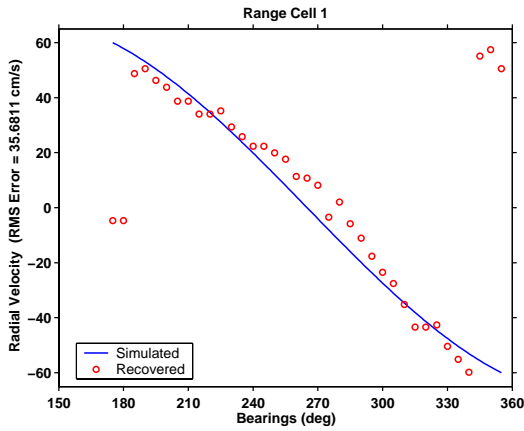


(B2) Recovered by Meas1

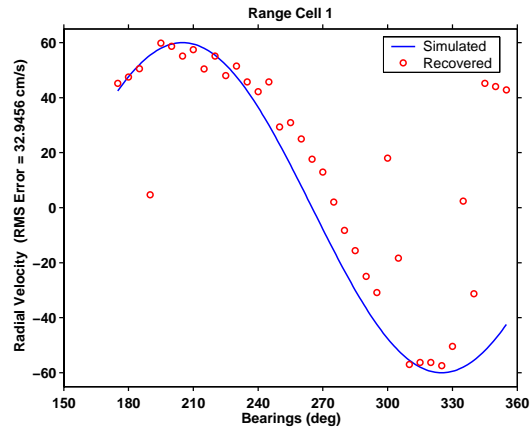
Figure 15. Mean Simulated (Blue Line) Versus Recovered (Red Circles) Radial Current Patterns by Ideal (A1 and B1) and Meas1 (A2 and B2) Antenna Patterns of Single- and Dual-Solution Current Regimes (Left and Right Panels Respectively)

2. Scenario 1B

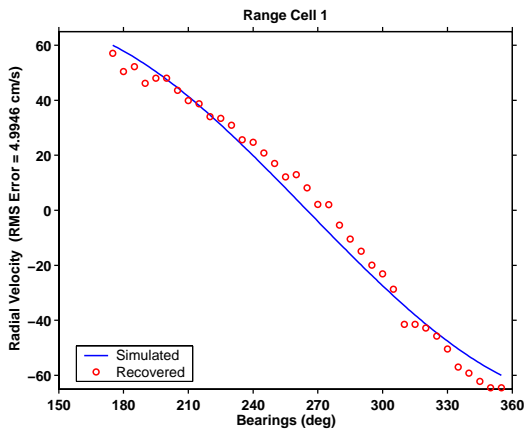
This scenario was created to study the influence of a fixed phase deviation from the Ideal pattern on MUSIC's recovery. Meas2 was used to generate seven spectral files and the hourly radials were recovered, using the Meas2 and Ideal patterns. For the latter, the phase was initially not corrected, i.e. phase = [0,0] and subsequently corrected, i.e. phase = [90,90] to account for the +90° phase shift of Meas2. Shown in Figure 16, RMS errors exceeding 30 cm/s were encountered when radials were recovered by the theoretical pattern without phase corrections and results improved to about 5.0 cm/s and 9.1 cm/s with phase corrections for the single- and dual-solution radial current patterns, respectively. Further improvements were observed when radial currents were recovered using the Meas2 pattern, with the RMS errors reduced to about 2.8 cm/s and 5.4 cm/s, respectively.



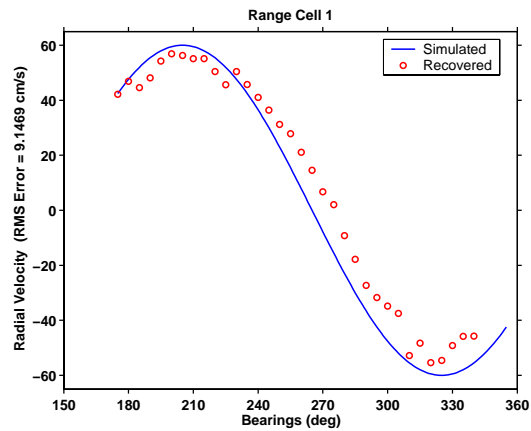
(A1) Recovered by Ideal



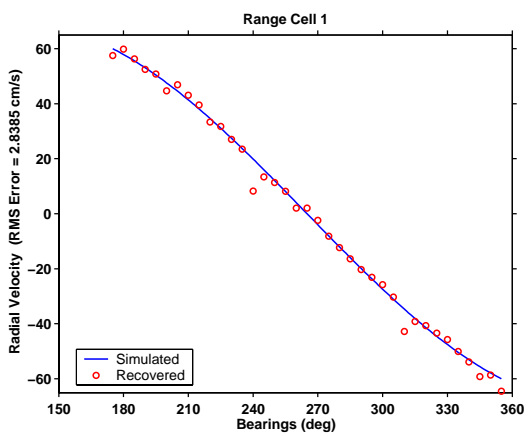
(B1) Recovered by Ideal



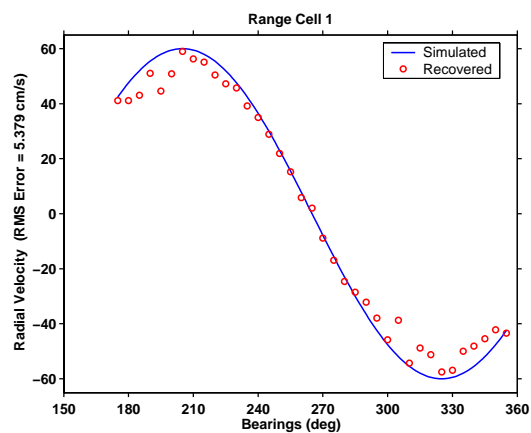
(A2) Recovered by Ideal with Phase



(B2) Recovered by Ideal with Phase



(A3) Recovered by Meas2



(B3) Recovered by Meas2

Figure 16. Mean Simulated (Blue Line) Versus Recovered (Red Circles) Radial Current Patterns by Ideal without Phase Corrections (A1 and B1), Ideal with Phase Corrections (A2 and B2), and Meas3 (A3 and B3) Antenna Patterns of Single- and Dual-Solution Current Regimes (Left and Right Panels Respectively)

3. Scenario 1C

Finally, we explore the contribution of amplitude deviation from the Ideal pattern. The spectral files were created using Meas3 and the hourly radials recovered using the Meas3 and Ideal patterns. The RMS errors of the single- and dual-solution radial patterns recovered by Meas3 were about 5.0 cm/s and 7.7 cm/s, respectively, and 8.0 cm/s and 12.3 cm/s by the theoretical pattern with phase = [0,0] (since Meas3 does not have any phase difference), respectively (See Figure 17). Radial velocity “gaps” were also observed during the recovery of the dual-solution radial pattern by both measured and ideal patterns.

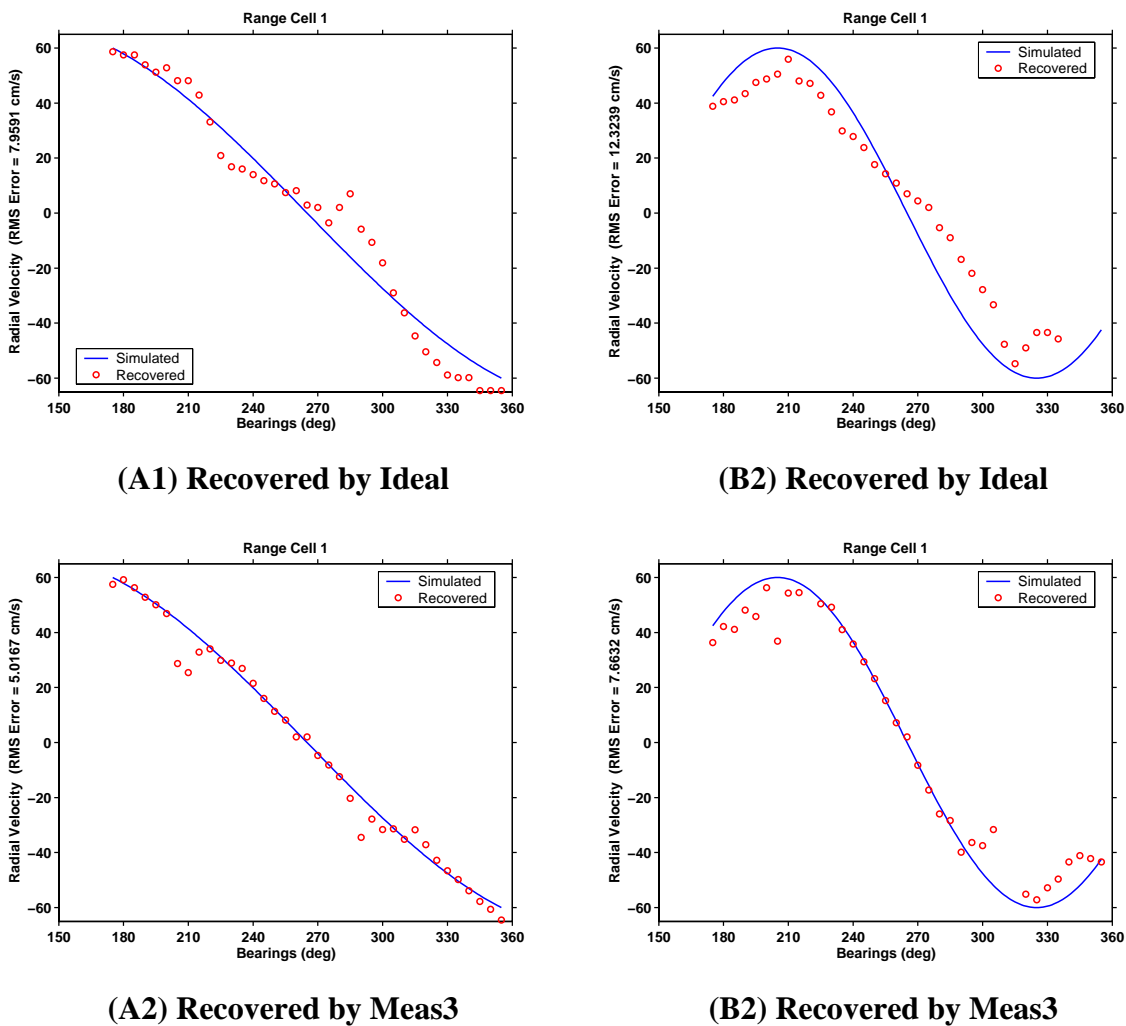


Figure 17. Mean Simulated (Blue Line) Versus Recovered (Red Circles) Radial Current Patterns by Ideal (A1 and B1) and Meas3 (A2 and B2) Antenna Patterns of Single- and Dual-Solution Current Regimes (Left and Right Panels Respectively)

C. DISCUSSION OF RESULTS

The RMS errors from the Scenario 1 series are tabulated in Table 6.

Scenario	Generating Antenna	Recovery Antenna	RMS Errors (cm/s)	
			Single Solution	Dual Solution
1A	Meas1	Theoretical (Phase = [0,0])	3.0525	6.4108
		Meas1	2.8385	5.3790
1B	Meas2	Theoretical (Phase = [0,0])	35.6811	32.9456
		Theoretical (Phase = [90,90])	4.9946	9.1469
		Meas2	2.8385	5.3790
1C	Meas3	Theoretical (Phase = [0,0])	7.9591	12.3239
		Meas3	5.0167	7.6632

Table 6. Summary of RMS Differences Between Simulated and Recovered Radial Velocities from Scenario 1 Series

The discussion points are as follows:

1. Recovery by Measured Antenna Pattern Yields Better Results

Radial pattern recovery by the measured pattern consistently yielded the best results, which is in agreement with simulation studies by Barrick & Lipa (1999), and Glenn et al. (2004) and Paduan et al. (2005). Though the above was conducted in a “clinical” setting with fixed phase or amplitude deviations, it revealed a pertinent truth that the character of the backscatter spectrum is affected by the near-field surroundings, and thus recovery using the measured pattern will yield the best results.

2. Amplitude Deviations Had Greater Effect on MUSIC

It was noted that the RMS errors recovered by Meas1 and Meas2 were the same; and Meas3 yielded the highest RMS errors. This suggested that amplitude deviations had a greater impact to MUSIC’s performance than phase, after known phase offsets were accounted for.

3. Phase Corrections Required For Recovery by Idealized Antenna Pattern

If measured patterns are not available, Scenario 1B showed that the Ideal pattern could still be used, provided it is phase-corrected to correctly reflect the character of the distorted pattern. These phases may be taken from estimates in the Stats-Diag file produced by the SeaSonde Suite, or preferably, from transponder measurements. However, results from these patterns would still be poorer than the measured, and thus should be regarded as a stop-gap measure until the distorted pattern could be mapped out in the field.

4. “Gaps” in Recovered Radial Velocity Pattern

Finally, in Scenario 1C, radial patterns recovered by both antenna patterns in the dual-solution current regime had radial velocity “gaps”. Although a comparison with Barrick & Lipa’s (1999) observation of the coverage densities of the radial vectors recovered by the Ideal and measured patterns is tempting, the averaging of seven radials may not have been sufficient to represent the statistics involved. This deficiency, however, will be addressed in the next scenario series.

The above scenarios gave some preliminary results and insights to the contribution of the antenna pattern in the recovery process – measured patterns yielded the best results, and suggested that amplitude deviations gave rise to larger RMS errors than phase deviations. However, when corrected for phase, Ideal patterns may still be used to mitigate the unavailability of the measured pattern.

In the next chapter, more ensembles of spectral file will be used to average a longer time series of radials, and thus accentuate any of the measured pattern’s character which may contribute to bias errors during the radial recovery process.

IV. SCENARIO 2 SERIES: EXPLORING MUSIC'S LIMITATIONS DUE TO CURRENT AND MEASURED ANTENNA PATTERN CHARACTERISTICS

A. SCENARIO 2 SERIES

To explore MUSIC's limitations in recovering radial vectors in relation to the measured antenna pattern, actual measured patterns from MLNG and PPIN were used, in addition to using DUMY site. Ideal patterns with adjusted phase input were excluded in this study as the results derived from the earlier scenarios showed them to be less accurate than the measured ones.

A larger ensemble of 28 1-hour radials, or equivalently 420 ($= 28 \times 15$) spectral file, were used to better simulate the random noise input. For each simulated hour, the errors between the recovered and simulated radial patterns were computed and plotted as a two-dimensional velocity error plot against bearings, accompanied by a correspondingly mapped SD_SeaSonde. Subsequently, the RMS errors were computed and SD_SeaSonde averaged for each bearing, giving an unbiased analysis of MUSIC's performance vis-à-vis the pattern and current characteristics.

The simulation scenarios matrix for the sites is shown in Figure 18. The scenarios were designed to study MUSIC's limitations in progressively more complex antenna patterns.

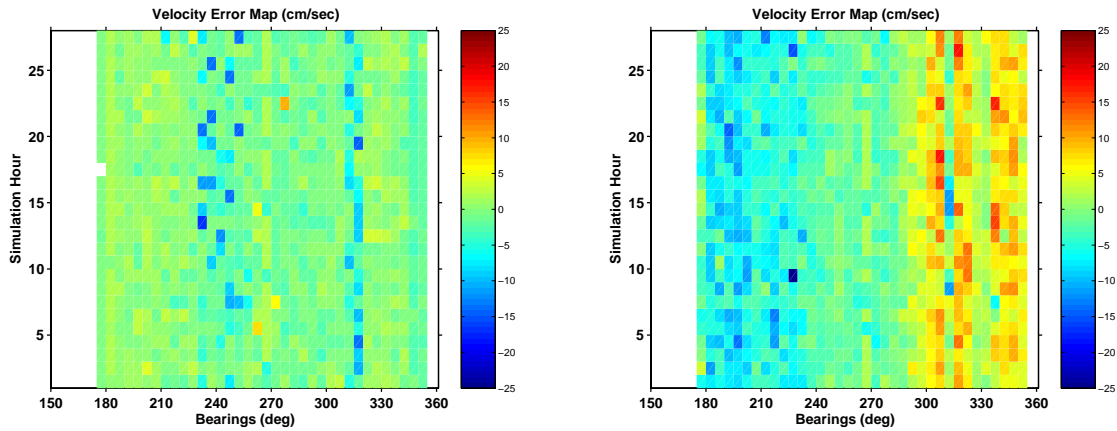
Scenario No.	Simulator Input		SeaSonde Recovery	
	Radial Patterns		Antenna Pattern (Amplitude)	Antenna Pattern (Amplitude)
2A			Meas1	Meas1
2B		Meas2	Meas2	
2C			Meas3	Meas3
2D		MLNG	MLNG	
2E		PPIN	PPIN	

Figure 18. Scenario Matrix for Scenario 2 Series, with Inputs for Both the CSSim_mod and SeaSonde Suite

B. RESULTS

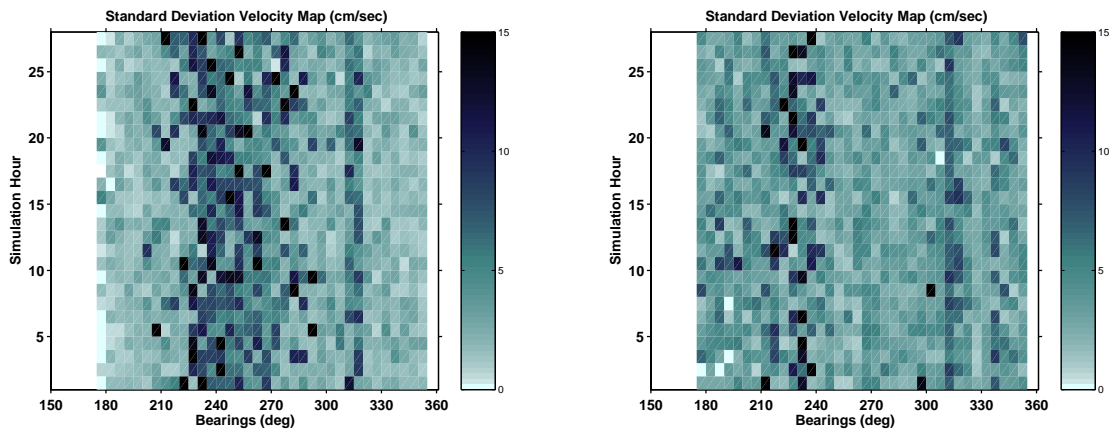
1. Scenario 2A

This scenario was created to study MUSIC's performance in the simplest case: using Meas1 to generate the backscatter spectrum and recover the radial pattern. Figure 19 shows the hourly ensembles of velocity error and SD_SeaSonde plotted against azimuth coverage of the site (referred to hereafter as maps) for the single- and dual-solution current regimes (left and right panels respectively).



(A1) Single-Solution Velocity Error Map

(B1) Dual-Solution Velocity Error Map



(A2) Single-Solution SD_SeaSonde Map

(B2) Dual-Solution SD_SeaSonde Map

Figure 19. Recovered 28 1-Hour Ensembles of Radial Velocity Errors (A1 and B1) Map and SD_SeaSonde (A2 and B2) by Meas1 of Single- and Dual-Solution Current Regimes (Left and Right Panels), Respectively

To appreciate the variability of the uncertainty (henceforth referring to both the computed RMS Errors and SD_SeaSonde) at each bearing across the ensembles, the RMS errors were computed (Equation 10) and SD_SeaSonde averaged (variances were summed in Equation 11 since noise was randomly added) for both current regimes.

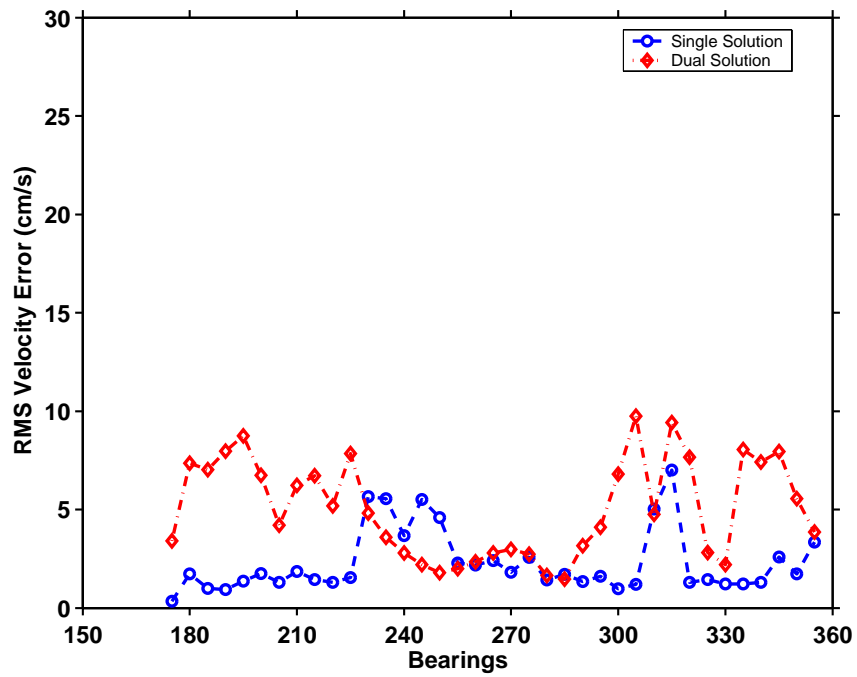
$$e_{rms}^i = \sqrt{\frac{\sum_{j=1}^{28} (V_{rcv_j}^i - V_{r_j}^i)^2}{n^i}} \quad (10)$$

- e_{rms}^i : RMS velocity error at bearing i
- $V_{rcv_j}^i$: radial velocity recovered at bearing i at simulated hour j
- $V_{r_j}^i$: simulated mean radial velocity at bearing I at simulated hour j
- n^i : total number of radial velocity recovered along bearing i ($n^i \leq 28$)

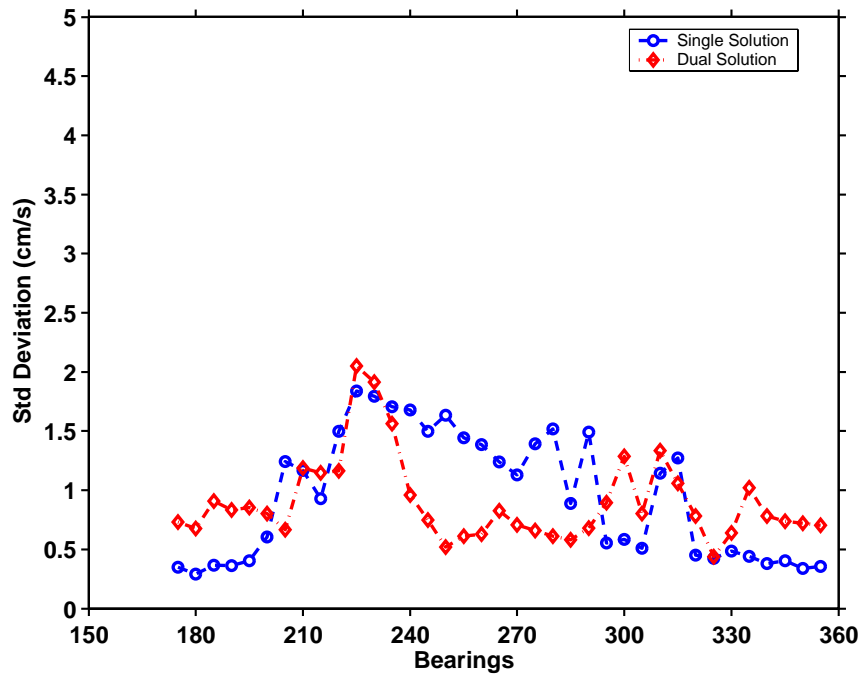
$$V_{SD}^i = \frac{1}{n^i} \sqrt{\sum_{j=1}^{28} (SD_j^i)^2} \quad (11)$$

- V_{SD}^i : standard deviation of radial velocity at bearing i
- SD_j^i : standard deviation of velocity at bearing i at simulated hour j
- n^j : total number of radial velocity recovered along bearing i ($n^i \leq 28$)

Figure 20 shows the uncertainty profile being plotted against bearings for the single- (blue dash-circle) and dual- (red dash-diamond) solution current regimes.



(A)



(B)

Figure 20. (A) RMS Velocity Error and (B) Average SD_SeaSonde Computed Along Bearings for Radial Ensembles Recovered by Meas1 for Single- and Dual-Solution Current Regimes (Blue Dash-Circle and Red Dash-Diamond, Respectively)

Referring to both Figure 19 and 20, the following were observed:

a. *RMS Errors Increase with Radial Pattern Complexity*

The velocity errors were averaged across the 28 1-hour ensembles and the RMS errors computed as 1.8673 cm/s and 5.0151 cm/s for the single- and dual-solution regimes, respectively.

b. *Inconsistent Coherence of RMS Errors and SD_SeaSonde*

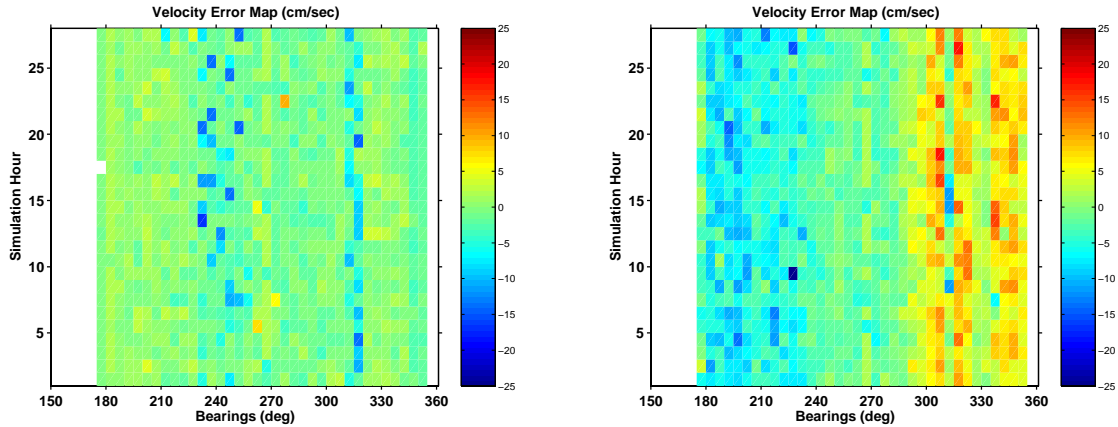
Other than an approximate visual match of a higher uncertainties along bearings 230° to 260°, and 310° to 315° in the single-solution regime, there was a general lack of coherence between the uncertainty profiles.

c. *Systematic Error Bias*

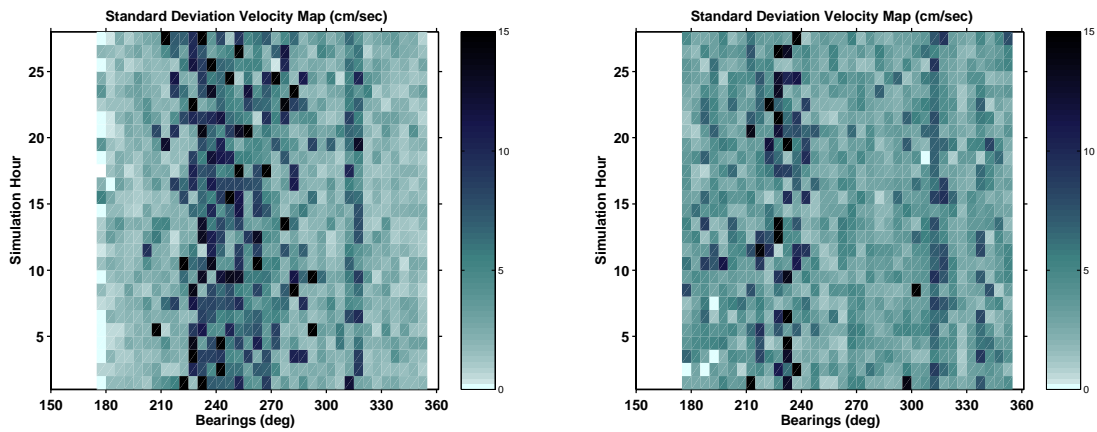
In the single-solution regime, the errors were somewhat random, except for a consistent negative error band, i.e. lower recovered velocities from simulated mean, along bearings 230° to 260° and 310° to 315°. However, in the dual-solution regime, positive error biases were systematically recovered at bearings 295° to 355°, and negative errors along bearings 180° to 230°.

2. Scenario 2B

In this scenario, MUSIC's performance was evaluated given Meas2, which has a constant phase shift of $+90^\circ$ from Meas1. Figure 21 shows the recovered velocity error and SD_SeaSonde maps.



(A1) Single-Solution Velocity Error Map (B1) Dual-Solution Velocity Error Map



(A2) Single-Solution SD_SeaSonde Map (B2) Dual-Solution SD_SeaSonde Map

Figure 21. Recovered 28 1-Hour Ensembles of Radial Velocity Errors (A1 and B1) Map and SD_SeaSonde (A2 and B2) by Meas2 of Single- and Dual-Solution Current Regimes (Left and Right Panels), Respectively

The velocity errors were averaged across the 28 1-hour ensembles and the RMS errors were computed as 1.8672 cm/s and 5.0151 cm/s for the single- and dual-solution regimes, respectively, which were exactly the same with Scenario 2A.

The RMS errors and average SD_SeaSonde at each bearing across the ensembles were computed and the results shown in Figure 22. Their characteristics were observed to be the same as Scenario 2A, confirming that phase does contribute to the correct recovery of radials.

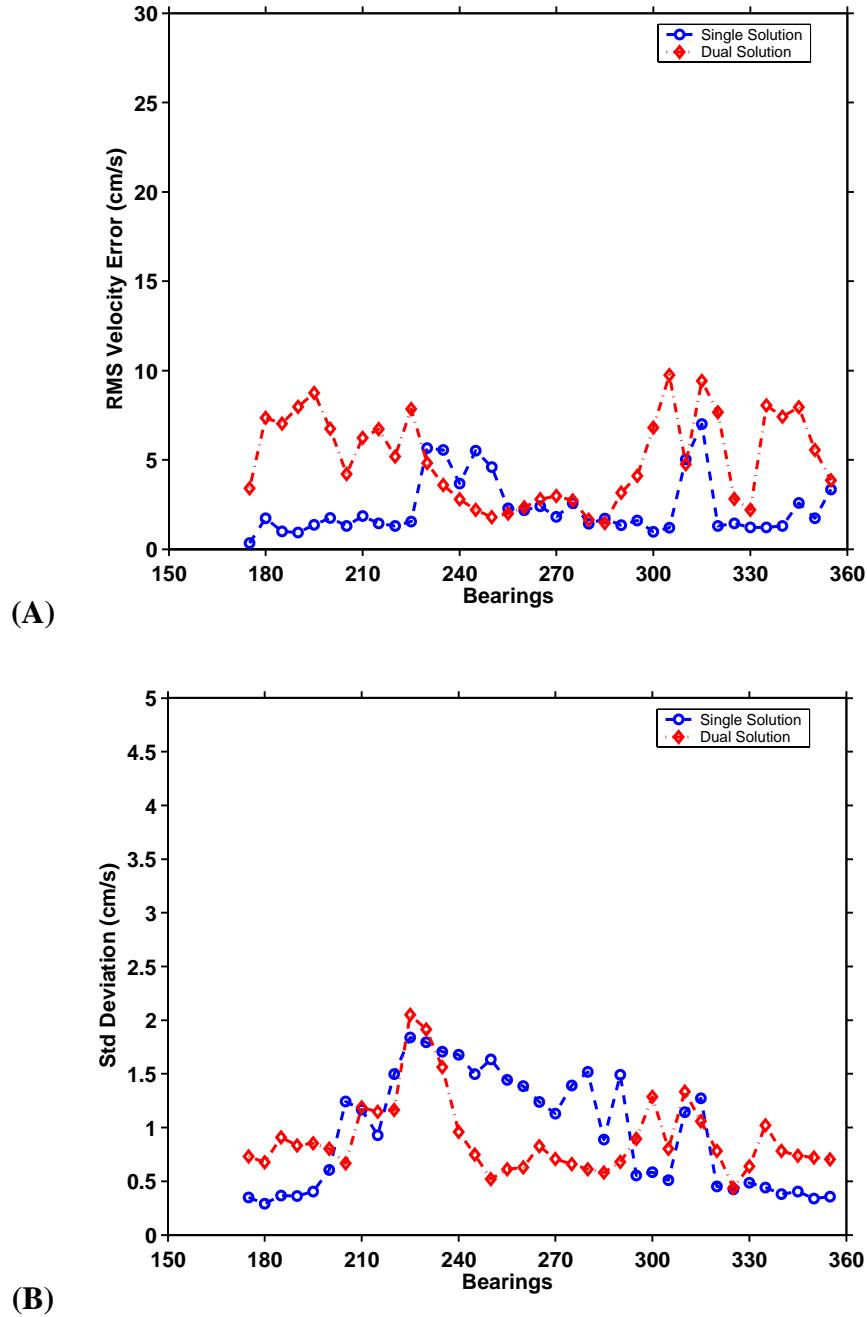
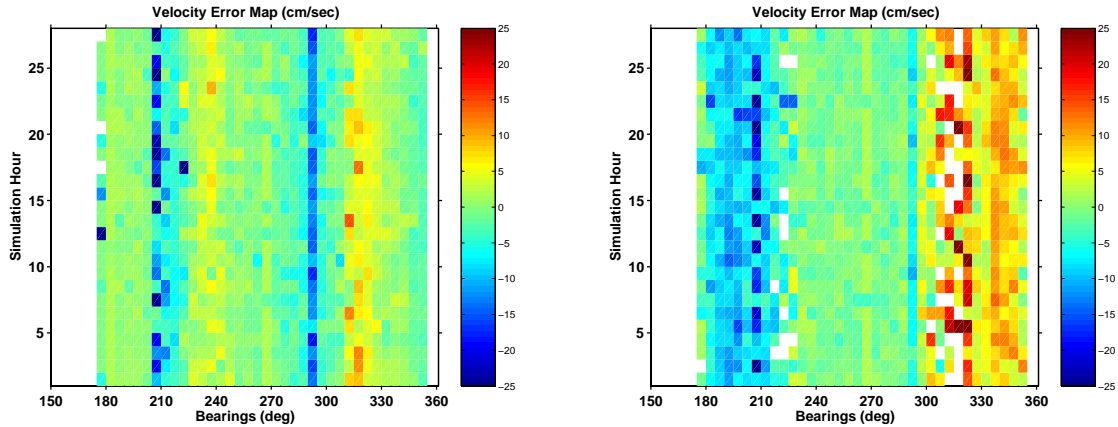


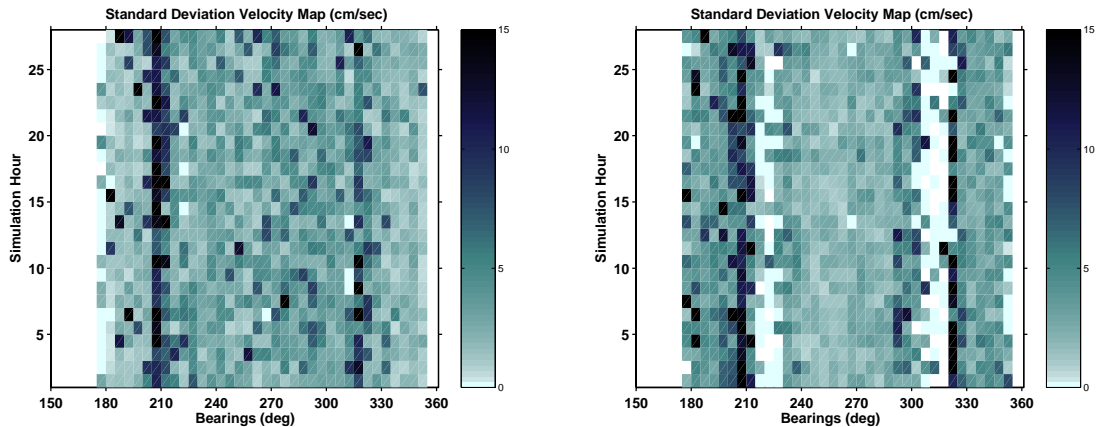
Figure 22. (A) RMS Velocity Error and (B) Average SD_SeaSonde Computed Along Bearings for Radial Ensembles Recovered by Meas2 for Single- and Dual-Solution Current Regimes (Blue Dash-Circle and Red Dash-Diamond, Respectively)

3. Scenario 2C

In this scenario, MUSIC's performance was evaluated given Meas3, which has a constant amplitude factor of two applied on Meas1. Figure 23 shows the recovered velocity error and SD_SeaSonde maps.



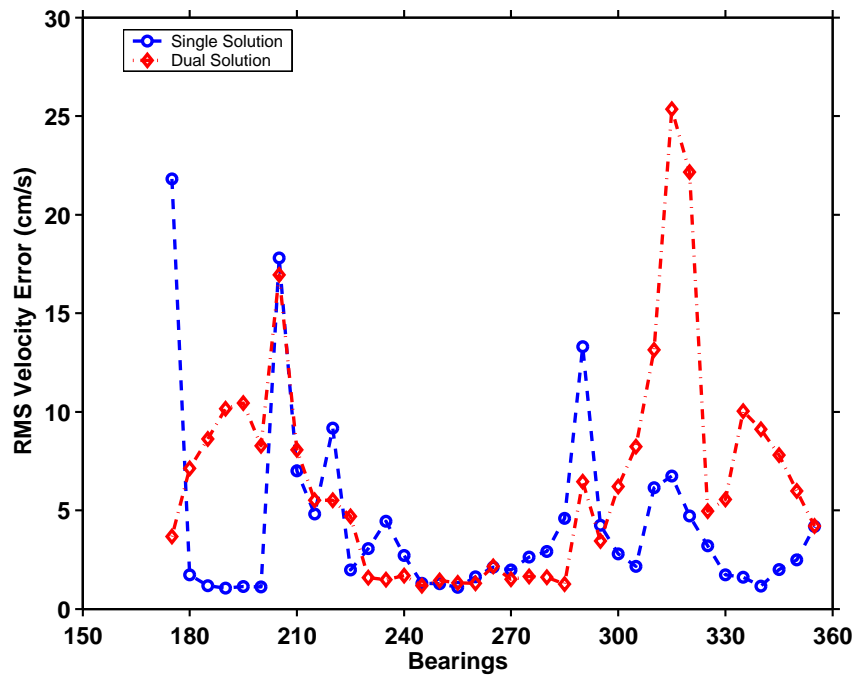
(A1) Single-Solution Velocity Error Map (B1) Dual-Solution Velocity Error Map



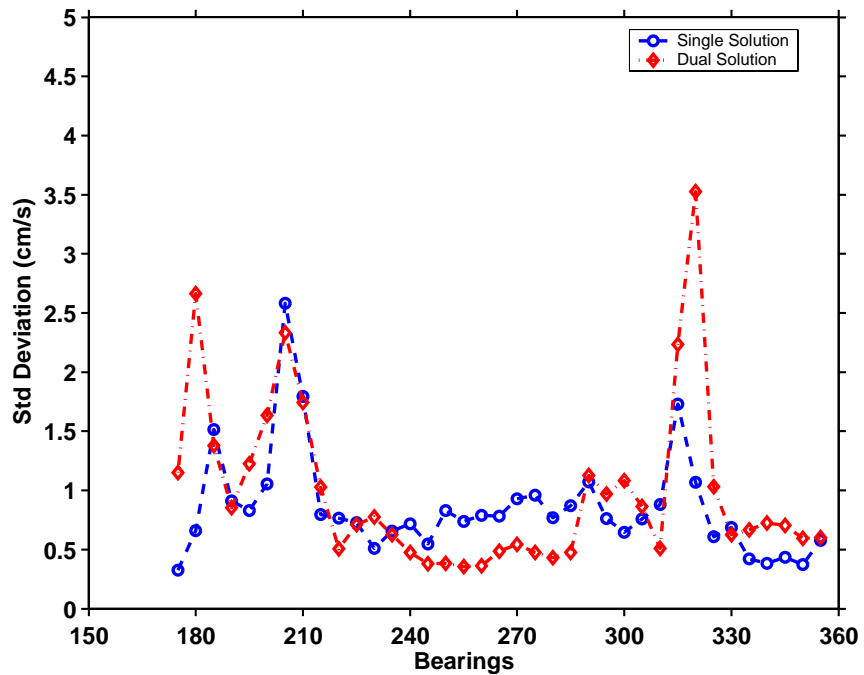
(A2) Single-Solution SD_SeaSonde Map (B2) Dual-Solution SD_SeaSonde Map

Figure 23. Recovered 28 1-Hour Ensembles of Radial Velocity Errors (A1 and B1) Map and SD_SeaSonde (A2 and B2) by Meas3 of Single- and Dual-Solution Current Regimes (Left and Right Panels), Respectively

The RMS error and SD_SeaSonde at each bearing across the ensembles were computed for both current regimes and the results shown in Figure 24.



(A)



(B)

Figure 24. (A) RMS Velocity Error and (B) Average SD_SeaSonde Computed Along Bearings for Radial Ensembles Recovered by Meas3 for Single- and Dual-Solution Current Regimes (Blue Dash-Circle and Red Dash-Diamond, Respectively)

The following were observed from Figures 23 and 24:

a. RMS Errors Increases with Radial Pattern Complexity

The velocity errors were averaged across the 28 1-hour ensembles and the RMS errors were computed as 4.3336 cm/s and 7.0235 cm/s for the single- and dual-solution regimes respectively. This was, by far, the worst results but it was expected and consistent with the results obtained from Scenario 1.

b. Inconsistent Coherence of RMS Errors and SD_SeaSonde

In the single-solution regime, higher RMS errors were observed along bearings 310° to 320°, 205° to 215° and 285 to 295° in the single-solution current regime. However, higher SD_SeaSonde were only observed in the band from 205° to 215°. In the dual-solution case, higher uncertainties coincided along bearings 205° to 215° and 320° to 330°.

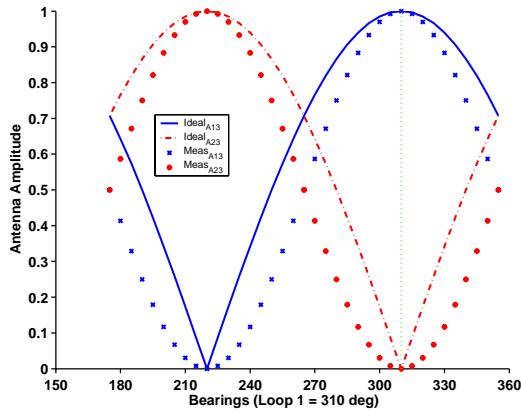
c. Systematic Error Bias

A consistent band of positive errors were observed along bearings 310° to 320°, and negative errors along 205° to 215° and 285 to 295° in the single-solution current regime. In the dual-solution case, velocity errors seemed to straddle the mid-bearings – negative errors at less than 215° and positive errors from 300° onwards.

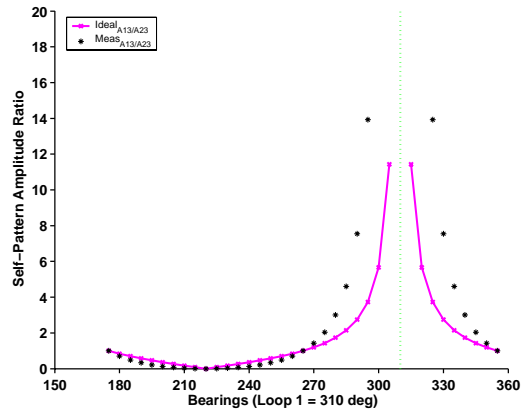
d. Correlation of RMS Errors with Measured Antenna Pattern Structure

In this particular instance, there were some evidence that large excursions of RMS errors coincided with departure of the measured pattern from the theoretical at bearings at 205° and 310°. As such, a series of comparison of the measured and theoretical patterns ensued, which included computation of the antennae amplitudes and

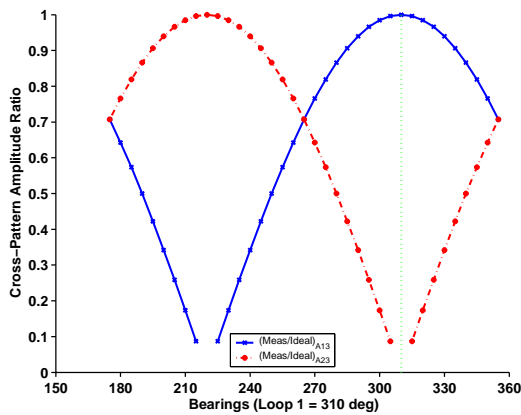
phase ratios, i.e., self-pattern antenna amplitude ratio $\left(= \frac{|\text{Meas Antenna 1}|}{|\text{Meas Antenna 2}|} \right)$ and $\frac{|\text{Ideal Antenna 1}|}{|\text{Ideal Antenna 2}|}$; cross-pattern antenna amplitude ratio $\left(= \frac{|\text{Meas Antenna 1}|}{|\text{Ideal Antenna 1}|} \right)$ and $\frac{|\text{Meas Antenna 2}|}{|\text{Ideal Antenna 2}|}$; and cross-pattern antenna phase ratio $\left(= \angle \frac{\text{Meas Antenna 1}}{\text{Ideal Antenna 1}} \right)$ and $\angle \frac{\text{Meas Antenna 2}}{\text{Ideal Antenna 2}}$. The computed ratios are shown in Figure 25.



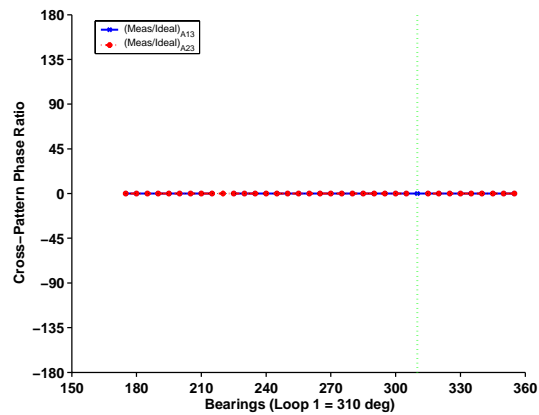
(A) Antenna Amplitude



(B) Self-Pattern Amplitude Ratio



(C) Cross-Pattern Amplitude Ratio



(D) Cross-Pattern Phase Ratio

Figure 25. Meas3 Vs Ideal (A) Antenna Amplitude, (B) Self-Pattern Antenna Amplitude Ratio, (C) Cross-Pattern Antenna Amplitude Ratio and (D) Cross-Pattern Antenna Phase Ratio

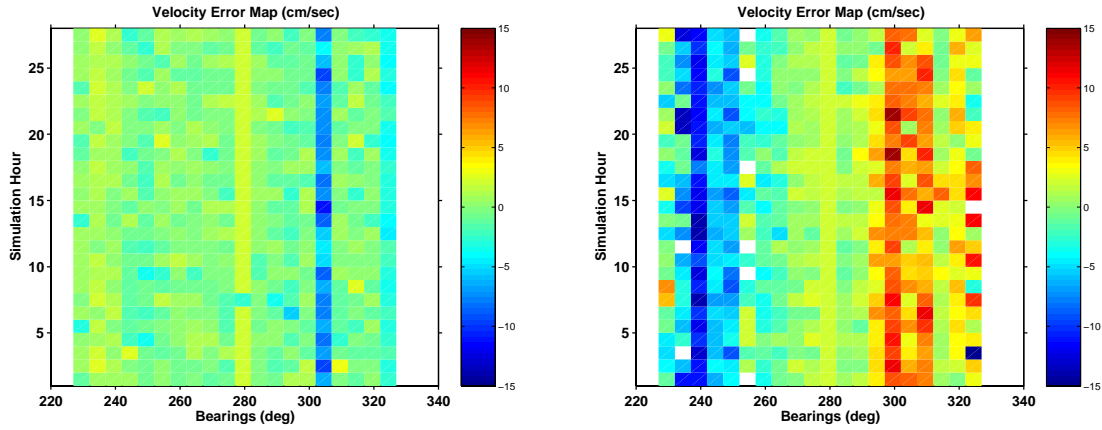
From the cross-pattern amplitude ratio plot, undefined values occurred at 215° to 225° and 305° to 315° , which were very close, but not coinciding, with the two predominant RMS error and SD_SeaSonde peaks in both the single- and dual-solution cases. This is a first indication that a possible relationship exists between MUSIC's performance and the character of the antenna and radial pattern.

e. “Gaps” in Recovered Radial Velocity Patterns

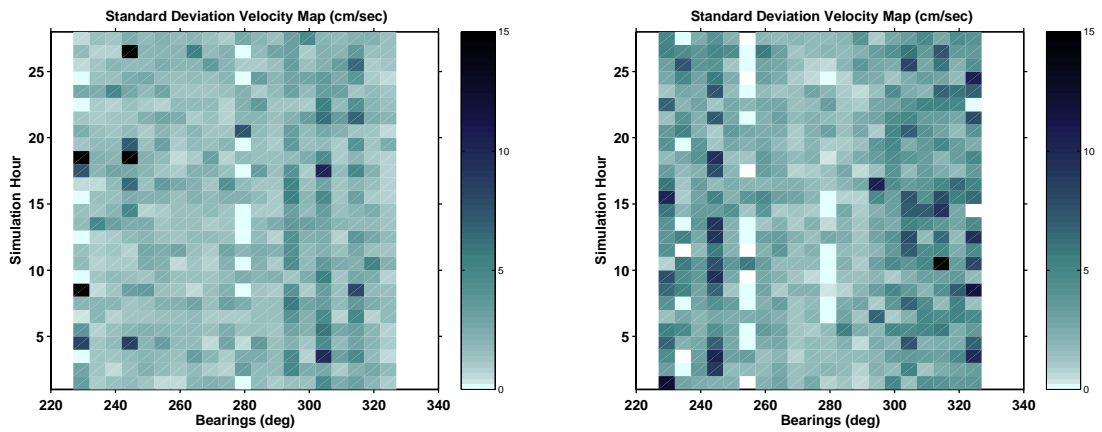
Consistent “gaps” in the recovered radial velocities were first observed in this scenario along bearings 220° to 225° and 310° to 320° of the dual-solution current regime. These “gaps” coincided with regions of undefined values of the amplitude ratios, higher uncertainties and near the maxima and minima of the dual-solutions current regimes.

4. Scenario 2D

This was the first scenario which used an actual measured antenna pattern, having variable amplitude and phase deviations, for both the generation of spectra and its subsequent recovery. The velocity error and SD_SeaSonde maps are shown in Figure 26.



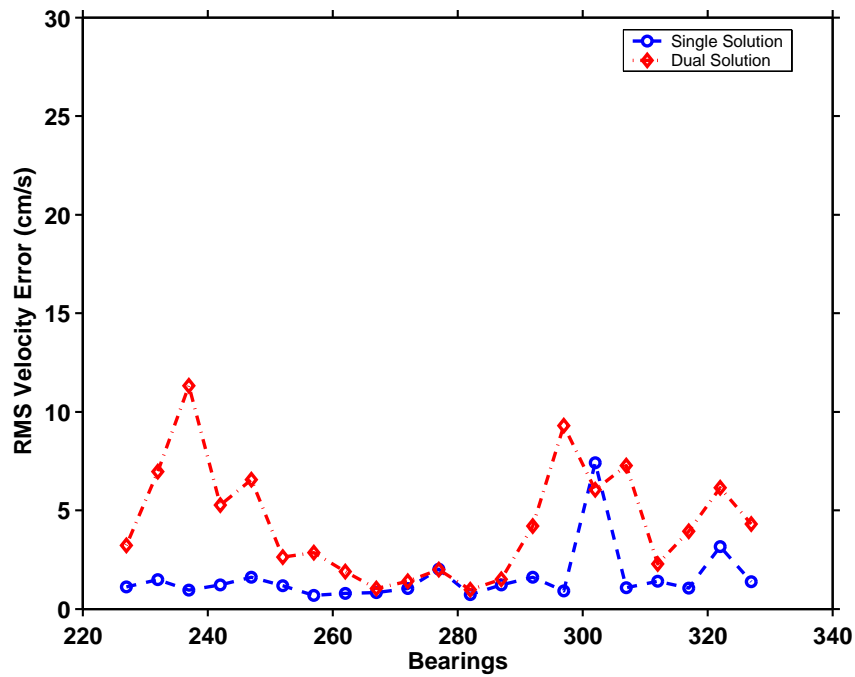
(A1) Single-Solution Velocity Error Map (B1) Dual-Solution Velocity Error Map



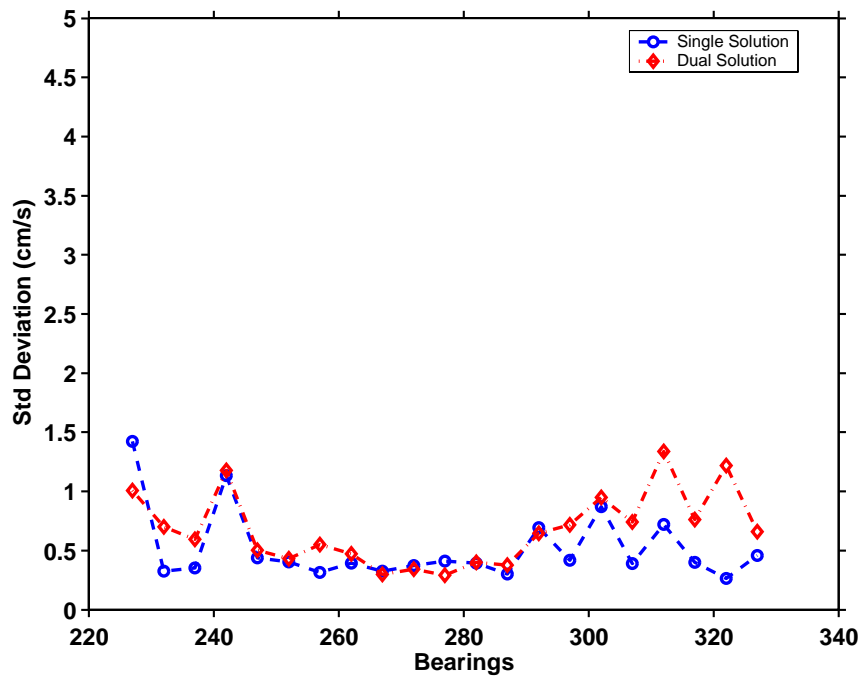
(A2) Single-Solution SD_SeaSonde Map (B2) Dual-Solution SD_SeaSonde Map

Figure 26. Recovered 28 1-Hour Ensembles of Radial Velocity Errors (A1 and B1) Map and SD_SeaSonde (A2 and B2) by MLNG Measured Antenna Pattern of Single- and Dual-Solution Current Regimes (Left and Right Panels) Respectively

The RMS error and SD_SeaSonde at each bearing across the ensembles were computed for both current regimes and the results are shown in Figure 27.



(A)



(B)

Figure 27. (A) RMS Velocity Error and (B) SD_SeaSonde Computed Along Bearings for Radial Ensembles Recovered by MLNG Measured Antenna Pattern for Single- and Dual-Solution Current Regimes (Blue Dash-Circle and Red Dash-Diamond, Respectively)

The following were observed from Figures 26 and 27:

a. *RMS Errors Increases with Radial Pattern Complexity*

The errors and SD_SeaSonde were averaged across the 28 1-hour ensembles and the RMS errors were computed as 2.6140 cm/s and 6.5275 cm/s for the single- and dual-solution regimes, respectively.

b. *Incoherence of RMS Errors and SD_SeaSonde*

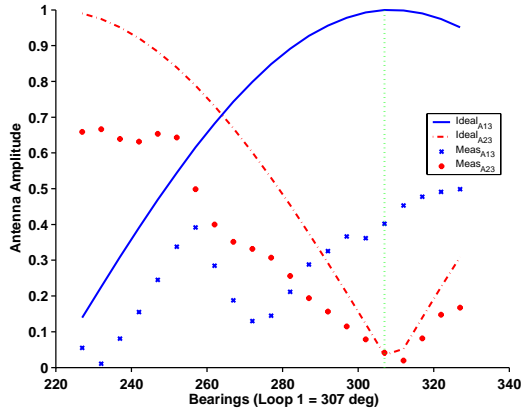
While the radial velocities in the single-solution regime displayed less uncertainty than the dual-solution case, the variability of the profile was more complex than all the previous scenarios. This suggested a more complex contribution of the antenna pattern in MUSIC's radial pattern recovery process.

c. *Systematic Error Bias*

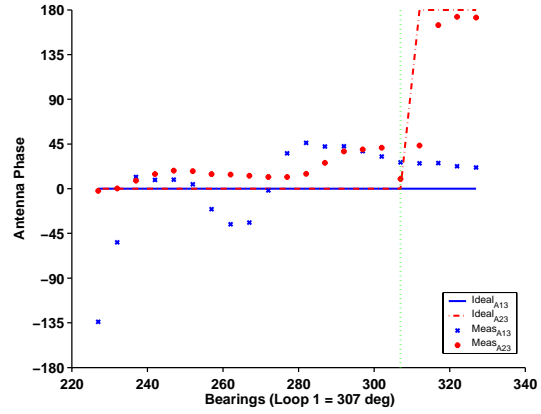
In the single-solution current regime, a persistent band of positive errors of about +5 cm/s was observed along bearing 277° and a persistent negative band occurred at 302° . In the dual-solution case, a consistent straddling of positive and negative errors around the mid-bearings was observed. Positive errors concentrated along bearings exceeding 292° and negative errors at less than 247° .

d. *Correlation of RMS Errors with Measured Antenna Pattern Structure*

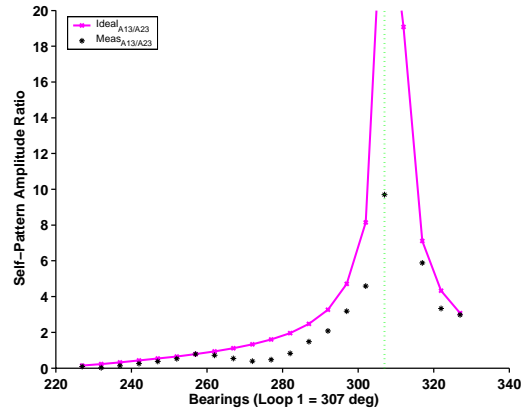
The large excursions of RMS errors were then compared with the structure of the measured antenna computed in the same manner as in Scenario 2C and shown in Figure 28. Higher RMS errors occurred at 302° for the single-solution current regime and from 297° to 307° and 232° to 247° for the dual-solution case. These occurred in the vicinity of sharp deviations of antenna amplitude and phase. However, no distinct correlation of RMS errors to the antenna pattern could be derived, which is testimony to the complex interaction of the antennae's amplitude and phase in MUSIC's radial recovery process.



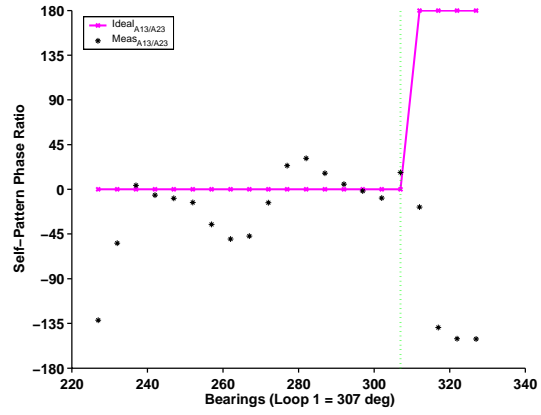
(A) Antenna Amplitude



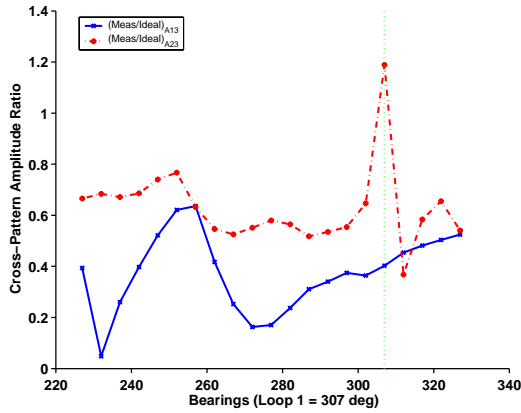
(B) Antenna Phase



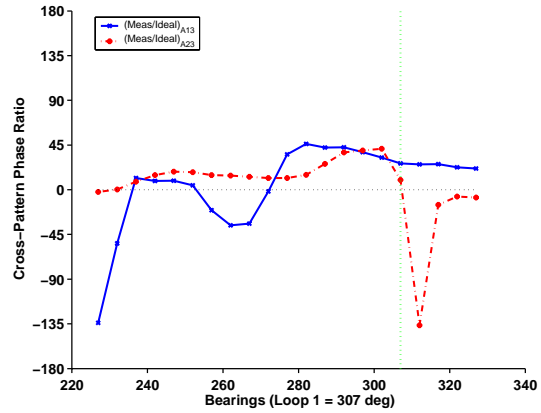
(C) Self-Pattern Amplitude Ratio



(D) Self-Pattern Phase Ratio



(E) Cross-Pattern Amplitude Ratio



(F) Cross-Pattern Phase Ratio

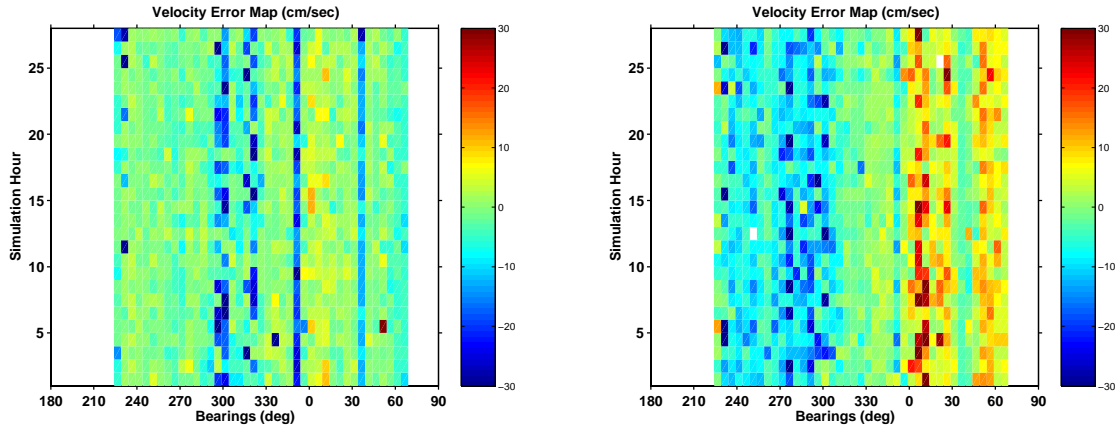
Figure 28. MLNG Measured Antenna Pattern Vs Ideal (A) Antenna Amplitude, (B) Antenna Phase, (C) Self-Antenna Amplitude Ratio, (D) Self-Pattern Phase Ratio, (E) Cross-Pattern Amplitude Ratio and (F) Cross-Pattern Phase Ratio

e. “Gaps” in Recovered Radial Velocity Patterns

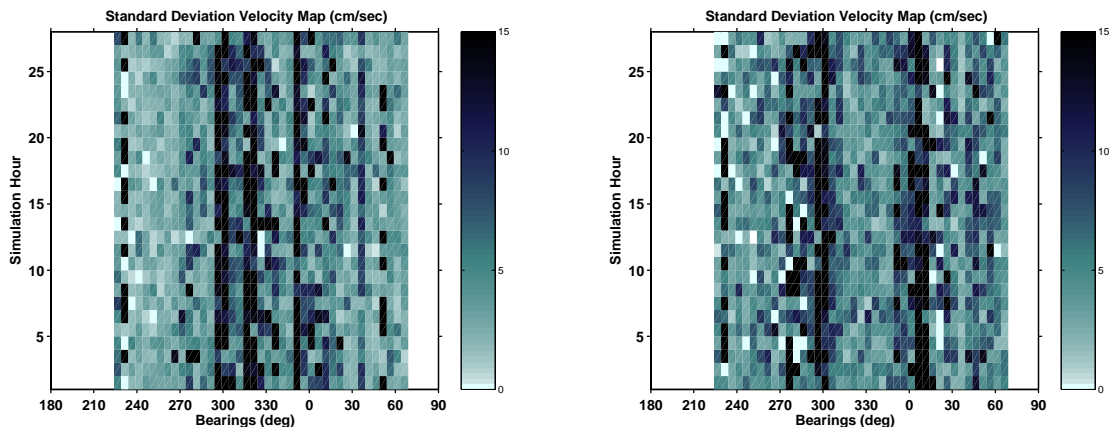
Like in scenario 2C, “gaps” in the recovered radial velocity pattern were observed at bearings 252° and 232° of the dual-solution current pattern. They do not coincide with regions where the antenna amplitude or phase experienced sharp deviations, nor at higher uncertainties. However, these “gaps” occurred near the maxima and minima regions of dual-solutions current regimes.

5. Scenario 2E

In this scenario, the actual measured antenna pattern from PPIN was used for both the generation of spectra and its subsequent recovery. The velocity error and SD_SeaSonde maps are shown in Figure 29.



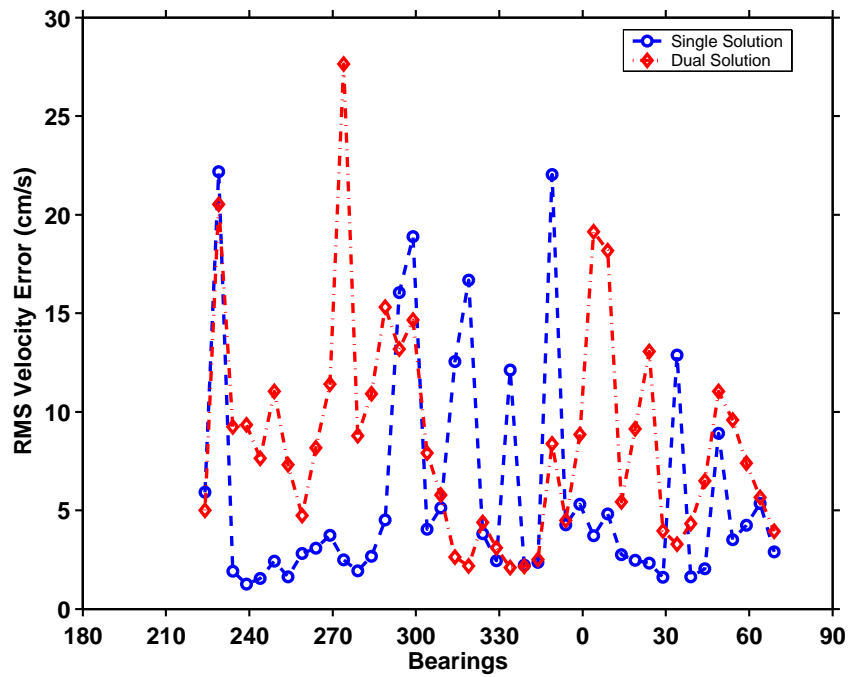
(A1) Single-Solution Velocity Error Map (B1) Dual-Solution Velocity Error Map



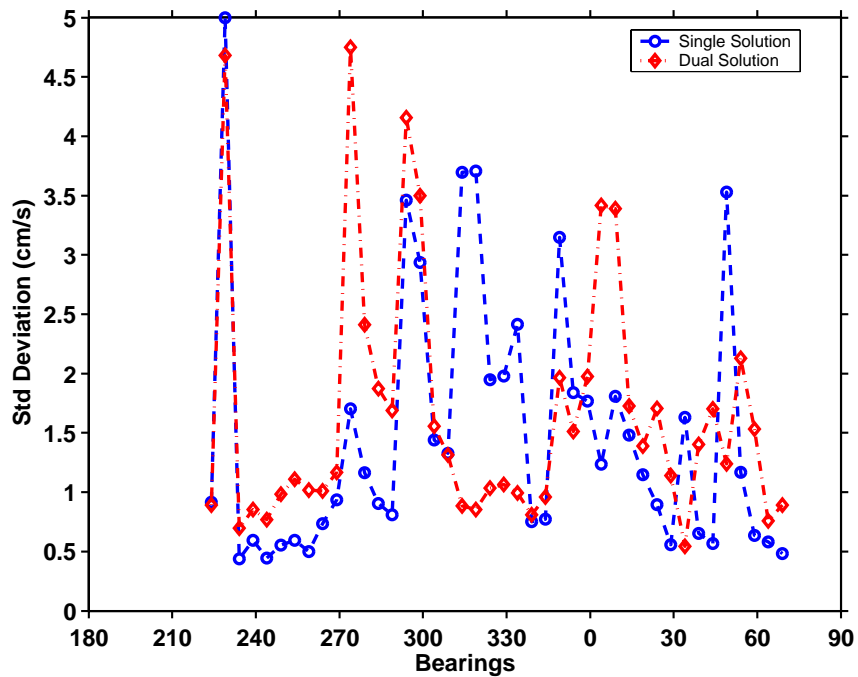
(A2) Single-Solution SD_SeaSonde Map (B2) Dual-Solution SD_SeaSonde Map

Figure 29. Recovered 28 1-Hour Ensembles of Radial Velocity Errors (A1 and B1) Map and SD_SeaSonde (A2 and B2) by PPIN Measured Antenna Pattern of Single- and Dual-Solution Current Regimes (Left and Right Panels), Respectively

The RMS error and SD_SeaSonde at each bearing across the ensembles were computed for both current regimes and the results are shown in Figure 30.



(A)



(B)

Figure 30. (A) RMS Velocity Error and (B) SD_SeaSonde Computed Along Bearings for Radial Ensembles Recovered by PPIN Measured Antenna Pattern for Single- and Dual-Solution Current Regimes (Blue Dash-Circle and Red Dash-Diamond, Respectively)

The following were observed from Figures 29 and 30:

a. *RMS Errors Increases with Radial Pattern Complexity*

The errors and SD_SeaSonde were averaged across the 28 1-hour ensembles and the RMS errors were computed as 6.2903 cm/s and 9.0354 cm/s for the single- and dual-solution regimes, respectively.

b. *Incoherence of RMS Errors and SD_SeaSonde*

The variability of the profile was, amongst the scenarios presented, the most complex and hence incoherent, which reinforced the notion that MUSIC's radial recovery process is affected by the complex interaction of the antennae's amplitude and phase.

c. *Systematic Error Bias*

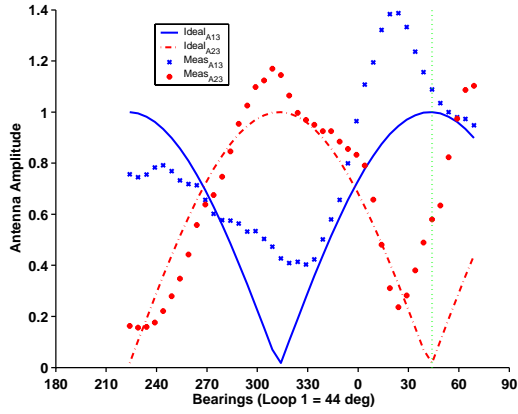
Numerous distinct bands of negative and positive errors (impractical to list here) were recovered from the single- and dual-solution current regimes. The errors recovered from the dual-solution case continue to straddle along the mid-bearings, with positive errors at 359° onwards and negative errors at 319° and less.

d. *Correlation of RMS Errors with Measured Antenna Pattern Structure*

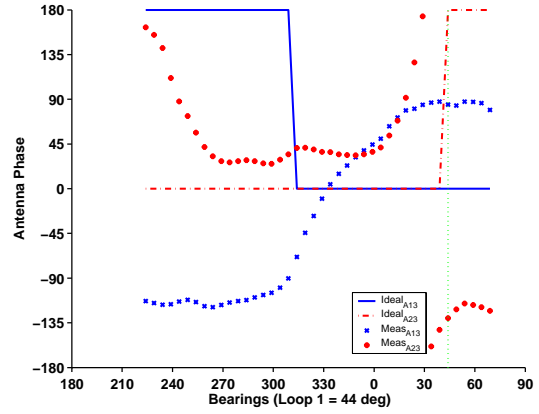
The large excursions of uncertainty were then compared with the structure of the measured antenna and shown in Figure 31. RMS errors occurring in the vicinity of sharp deviations of antenna amplitude and phase at 227°, 229° to 329°, 359° to 029°, 039° to 064°, were generally higher. Like in Scenario 2D, no distinctive correlation of RMS errors to the antenna pattern could be derived, arguing for the complex interaction of the antennae's amplitude and phase in MUSIC's radial recovery process.

e. *“Gaps” in Recovered Radial Velocity Patterns*

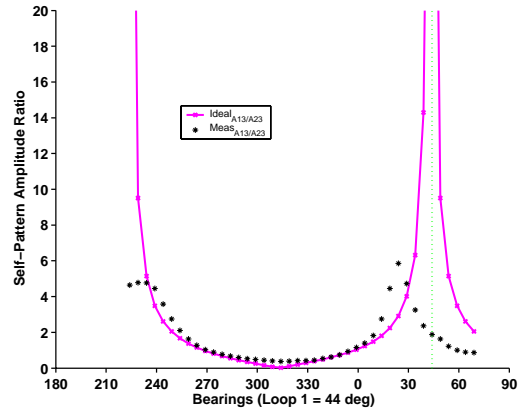
“Gaps” in the recovered radial velocity pattern continued to be observed in the dual-solution current pattern, but only at two locations. This is due to the coarser velocity resolution of the lower operating frequency of the PPIN site, which effectively reduces the width of the Bragg peaks. Like in Scenario 2D, the location of the “gaps” do not coincide with regions where the antenna amplitude or phase deviated most from the ideal, nor at higher uncertainties. They however, continued to occur near the maxima and minima regions of the dual-solution current regimes.



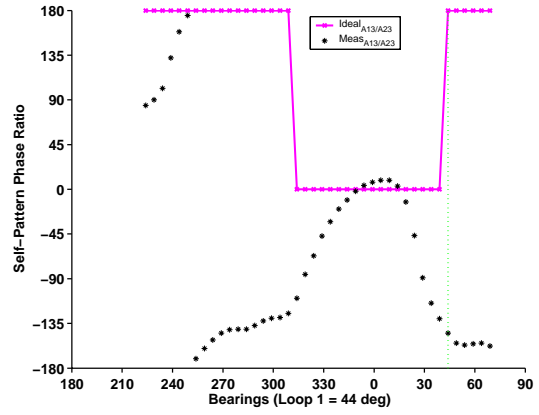
(A) Antenna Amplitude



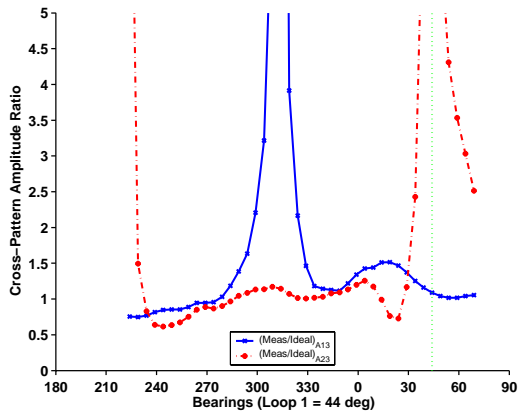
(B) Antenna Phase



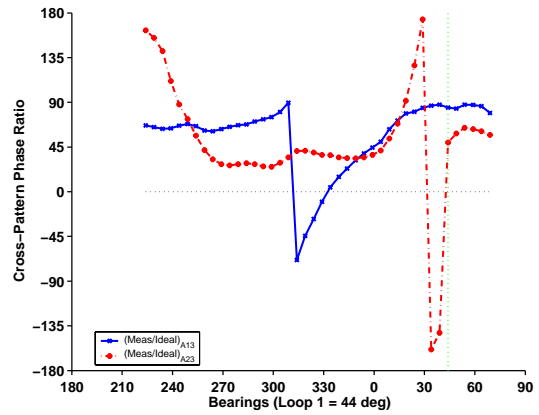
(C) Self-Pattern Amplitude Ratio



(D) Self-Pattern Phase Ratio



(E) Cross-Pattern Amplitude Ratio



(F) Cross-Pattern Phase Ratio

Figure 31. PPIN Measured Antenna Pattern Vs Ideal (A) Antenna Amplitude, (B) Antenna Phase, (C) Self-Antenna Amplitude Ratio, (D) Self-Pattern Phase Ratio, (E) Cross-Pattern Amplitude Ratio and (F) Cross-Pattern Phase Ratio

C. DISCUSSION OF RESULTS

1. RMS Errors Increases with Radial Pattern Complexity, Amplitude Deviations and Poorer Velocity Resolution

Using an ensemble of spectra (and hence radial files), noise inherent in the current was averaged in the radial recovery process. This allowed an unbiased analysis of the performance of MUSIC. The RMS errors for this scenario series were tabulated and are presented in **Error! Reference source not found.**

Scenario	Generating Antenna	Recovery Antenna	RMS Errors (cm/s)	
			Single Solution	Dual Solution
2A	Meas1	Meas1	1.8672	5.0151
2B	Meas2	Meas2	1.8672	5.0151
2C	Meas3	Meas3	4.3336	7.0235
2D	MLNG	MLNG	2.614	6.5275
2E	PPIN	PPIN	6.2903	9.0354

Table 7. Summary of RMS Errors Recovered by Scenarios 2 Series

The RMS error increases from the single- to dual-solution current regimes. This was expected as MUSIC's DF capability is challenged in the latter. Similar results culled from Meas1 and Meas2, but worse results from Meas3, suggested that MUSIC is affected more by amplitude than phase deviations. Results from PPIN were worse than MLNG's, which is, at least in part, attributed to the poorer velocity resolution of the Bragg spectra (Laws et al., 2000; Essen et al., 2000; Laws, 2001; Paduan et al., 2004).

2. General Incoherence of RMS Error and SD_SeaSonde

While there were occasions that high SD_SeaSonde coincided with high RMS errors, the distribution of SD_SeaSonde was, for the most part, incoherent with the distribution of the RMS Errors (except in the dual-solution regime in Scenarios 2C and 2E). This consolidated the notion that SD_SeaSonde is not a consistent indicator of the quality of the recovered radials.

3. Systematic Error Bias

It was noted that the distribution of errors was somewhat systematic, where positive and negative errors seemed to congregate at specific bearings, especially in the dual-solution regimes. This may be attributed to the distorted antenna pattern, and possibly aggravated by an indexing offset during the localizing of the Bragg peaks, induced by different FFT algorithms adopted by MATLAB and SeaSonde (discussed in Chapter II Section E).

4. Inconsistent Correlation of RMS Errors with Measured Antenna Pattern Structure

Results from Scenario 2C suggested a possible correlation of RMS errors with the amplitude structure of Meas3 – higher RMS errors coincided with undefined amplitude ratios between measured and ideal antenna patterns. However, in the case of Scenarios 2D and 2E, no appropriate correlation of the antenna pattern to MUSIC’s performance was derived, due to the varying and complex nature of amplitude and phase deviations of the MLNG and PPIN antenna patterns from the Ideal.

5. “Gaps” in Recovered Radial Velocity Patterns

In Scenario 2C, radial velocity “gaps” occurred at confined bearings in the dual-solution regime, which agreed to a certain extent, with Barrick & Lipa (1999). They observed that the coverage densities of the radial vectors were “gappy” when recovered by the measured antenna patterns and attributed them to deviations of the antenna pattern from the Ideal. Our initial analysis also indicated that the “gaps” occurred in the vicinity of higher SD_SeaSondes and maxima and minima regions of the dual-solution pattern.

While these “gaps” continued to be observed in the dual-solution velocity error maps in Scenario 2D, it was significantly reduced in Scenario 2E. This may be attributed to the narrower Bragg peaks since the PPIN site operates at a lower frequency, and hence coarser velocity resolution.

Thus, in addition to Barrick & Lipa’s (1999) explanation for the reduced coverage densities, other contributors included the operating frequency, antenna and radial pattern characteristics.

Using actual measured antenna patterns to analyze the recovered radials upped the ante and revealed the complex contribution of amplitude and phase to MUSIC's performance. This complicated interaction warrants further research, of which CODAR holds the key to making its MUSIC algorithm readily available for scrutiny and thus improve its bearing discrimination ability.

In the next chapter, using actual antenna patterns, MUSIC's radial recovery performance under a realistic decreasing SNR environment will be investigated.

THIS PAGE INTENTIONALLY LEFT BLANK

V. SCENARIO 3 SERIES: RECOVERING RADIALS UNDER VARYING SNR

A. SCENARIO 3 SERIES

Finally, SeaSonde's ability to recover radial vectors in a realistic SNR environment was evaluated. Using the COS version of the HF-radar SNR equation and HF noise floor expression, the Doppler backscatter spectra corresponding to one hour were generated with attenuating SNR for range cells extending from cells 1 to 28 (default in SeaSonde). Measured antenna patterns from two operational sites, MLNG and PPIN, were used to generate the spectral files, which were subsequently recovered using their measured and theoretical patterns. Recovery by the latter was phase corrected by two methods: via the **CrossLoopPatterner** tool to extract the measured phases or the Stats-Diag file, which provides the estimated phases based on the sea echo. The coverage, i.e., the proportion of vectors within the simulated radar site's angular field of view, and RMS errors were computed and plotted.

B. SNR EQUATION

The validity of results culled from this part of the study hinge on the correct SNR formulation for the simulated HF-radar. There are a couple of versions (Revell & Emery, 1998; Milsom, 1997; Headrick, 1990) and other more elaborate ground-wave propagation models (Sevgi & Sanal, 1997; Sevgi et al., 2002) available, but the more easily implemented ones were narrowed to the one provided by COS (2005) and the Sevgi et al. (2001) version. Closer inspection revealed that these formulations are the same, after accounting for the definition of the slightly different terms used in each one. Anticipating that COS's assistance may be required, the COS version was adopted. The SNR formulation is given as follows:

$$\text{SNR} = \frac{P_t G_t L_c D_r F^4 \sigma^o \Delta A \lambda^2 \tau_i}{(4\pi)^3 R^4 kT F_a} \quad (12)$$

- P_t : Average transmitter power output – SeaSonde duty factors are 50%
- G_t : Transmit antenna power-gain over earth, including ground losses
- L_c : Cable losses to transmit antenna
- D_r : Receive antenna directive gain, excluding ground losses
- λ : Radar wavelength
- τ_i : Integration time or FFT time-series length (in seconds) for spectra processing
- kT_o : Internal receiver front-end noise per unit bandwidth at operating temperature
- σ^o : Normalised radar cross section of first-order Bragg scatter from the sea
- R : Range to mid-point of the specified radar scattering cell
- ΔA : Area inside radar cell at specified range
- F : One-way attenuation factor above normal free-space spreading loss experienced by surface waves above a lossy spherical Earth
- F_a : Atmospheric noise factor

Also available from the COS SNR formulation were estimates of the fixed and variable parameters for the 13 MHz and 25 MHz systems which were adopted for both PPIN and MLNG sites, respectively.

1. Estimates of Range-Independent Parameters

a. Average Transmitter Power Output (P_t)

SeaSonde employs a duty factor of 50% and the average power was set at 50W for both MLNG and PPIN sites.

b. Transmit Antenna Power-Gain Over Earth, Including Ground Losses (G_t)

Factors of 1.0 and 1.6 were adopted for the PPIN and MLNG sites respectively.

c. Cable Losses to Transmit Antenna (L_c)

Factors of -3 dB and -4 dB were used for the PPIN and MLNG sites respectively.

d. Receive Antenna Directive Gain, Excluding Ground Losses (D_r)

Both sites used a factor of 3.2.

e. Radar Wavelength (λ)

Given the transmitter frequency in MHz (f_{MHz}) at each site, the radar wavelength is computed as $300/f_{MHz}$.

f. Normalized Radar Cross Section (σ^o):

The (normalized) radar cross section per unit area of the sea surface is responsible for the resonant backscatter of the radar waves at near-grazing angles (Barrick, 1972). The values estimated for MLNG is -33 dB and the one for PPIN is -38 dB.

g. Atmospheric Noise Factor (F_a)

At high frequencies, external noise dominates internal noise. In the 1930s, the C.C.I.R. (French abbreviation for Consultative International Radio Committee) conducted a worldwide study to relate this factor as a function of time of day, season of the year, sunspot number and geographic location (CCIR, 1988). An average value of this factor across the HF band was calculated using the C.C.I.R. data (Glenn et al., 2004):

$$F_a = 70 - 27.5 \log_{10} f_{MHz} \quad (\text{dB}) \quad (13)$$

h. Integration Time (τ_i)

The integration time or FFT time-series length (in seconds) for spectral processing for both sites was fixed at 256 sec, which also corresponded to $1/B$ where B is the effective noise bandwidth of the system.

i. Internal Receiver Noise Per Unit Bandwidth at Operating Temperature (kT_o)

The receiver's internal noise per unit bandwidth was computed assuming an operating temperature of 17°C, $T_o = 290^\circ\text{K}$ and $k = \text{Boltzmann's constant} = 1.38 \times 10^{-23} \text{ Joule/}^\circ\text{K}$.

2. Estimates of Range-Dependent Parameters

a. *Range to the specified radar scattering cell (R)*

This is defined as the distance from the radar site to the centre of that cell.

b. *Area Inside a Radar Range Cell (ΔA)*

Each range cell or annular of depth or width ΔR (function of transmitted frequency bandwidth) is sub-divided into sectors of angular width, $\Delta\theta$. Therefore, the area prescribed by the cell at range R is given by $R\Delta R\Delta\theta$.

c. *One-way Attenuation Factor above Normal Free-Space Spreading Loss (F)*

Based on propagation theories developed by Norton (1936) and Wait (1962), Barrick (1971) used the program provided by Berry & Chrisman (1966) to investigate propagation losses above a rough sea surface while accounting for the Earth's curvature. Since then, Barrick developed a FORTRAN program called "SegWave" to compute this factor as a function of frequency, sea properties and range (Glenn et al., 2004). The factor decays monotonically from unity close to the source to zero at infinity and is raised to the fourth power to account for the two-way radar path. For this study, Barrick kindly provided the tabulated F values computed for the MLNG and PPIN operating frequencies based on a 2 m Significant Wave Height (a typical value) and conductivity of 4 mho/m, which corresponds to a typical salinity of 33 ppt and water temperature of 14°C. Interpolation was carried out at ranges corresponding to each site's range cells to get the approximate F -value.

The above parameters were then used to compute the SNR values for both the MLNG and PPIN sites, which are plotted in Figure 32. It shows that the PPIN's SNR curve slopes more gradually with increasing range, which agrees with the rule-of-thumb that lower frequencies, are less susceptible to attenuation.

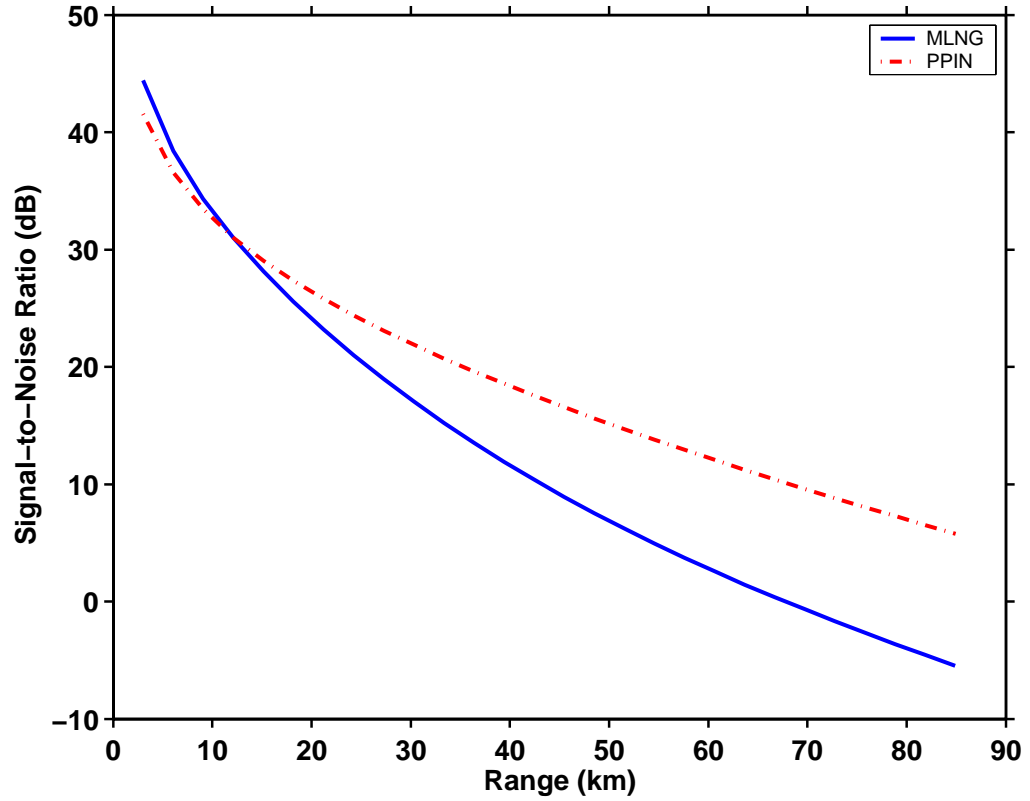


Figure 32. Computed Signal-to-Noise Ratio for MLNG (solid blue) and PPIN (red dash-dot)

C. HF NOISE

In the HF frequency band, external noise dominates the receiver's internal losses and noise levels and manifests as a noise floor in the actual HF spectrum (CCIR, 1988). To mimic the actual Doppler backscatter spectrum, a noise floor was simulated in the spectra generated by CSSim_mod.

Since the SNR is a ratio of signal-to-noise power, the voltage factor (V_{SNR}) of the signal-to-noise is simply its square-root.

$$V_{SNR} = \sqrt{\frac{P_t G_t L_c D_t F^4 \sigma^o \Delta A \lambda^2 \tau_i}{(4\pi)^3 R^4 kT F_a}} \quad (14)$$

This reduction factor was used to scale the maximum simulated voltage (V_{\max}) on the monopole antenna to yield the voltage signal (V_{floor}), which would correspond to the actual noise floor:

$$V_{\text{floor}} = \frac{V_{\max}}{V_{\text{SNR}}} \quad (15)$$

The external noise (N_{floor}) was then computed using the Atmospheric Noise Factor (F_a) over the receiver noise:

$$\begin{aligned} N_{\text{floor}} &= \sqrt{10^{F_a} \times k \times T_o \times \text{Bandwidth}} \\ &= \sqrt{10^{F_a} \times k \times T_o \times \frac{1}{\tau_i}} \end{aligned} \quad (16)$$

Therefore, with a one-to-one relation of the actual noise floor (N_{floor}) to the simulated voltage noise floor (V_{floor}), the actual simulated voltage for antenna k (V_{actual}^k) was then scaled from the simulated voltages $V_{\text{simulated}}^k$ as:

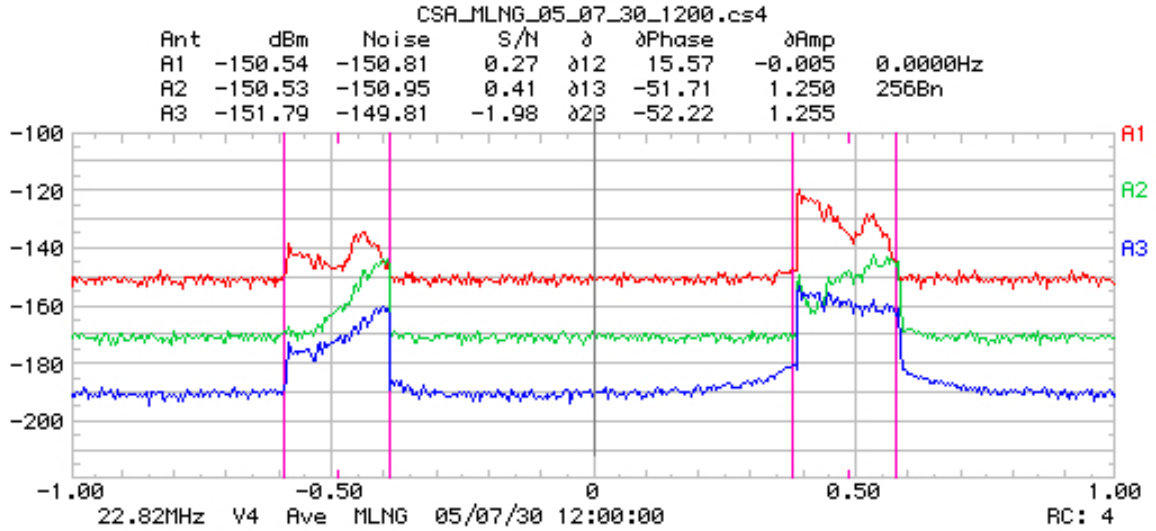
$$V_{\text{actual}}^k = \frac{V_{\text{simulated}}^k}{V_{\text{floor}}} \times N_{\text{floor}} \quad (17)$$

Finally, a Gaussian noise with a user-defined standard deviation Noise_{SD} was added to the voltage signals for each antenna element:

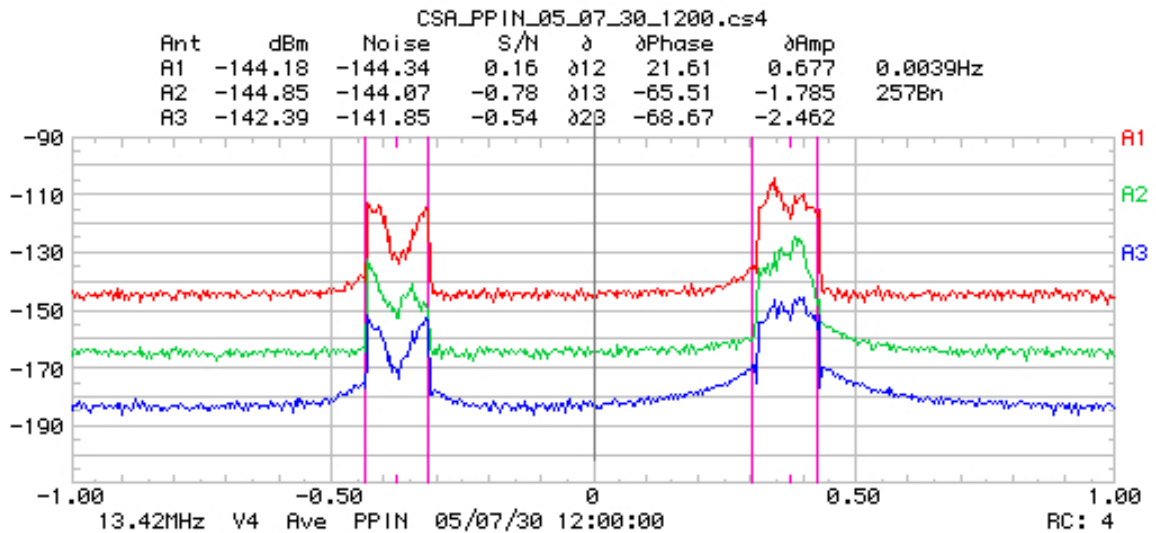
$$V_{\text{noise}} = \text{Noise}_{SD} \times \text{Normal}(0,1) \quad (18)$$

The noise-added voltage signals were then FFTed and the self- and cross-spectra stored in the spectral files. For validation purposes, the simulated backscatter spectra were compared with actual ones from MLNG and PPIN. The results were encouraging as the pertinent features of the spectrum, i.e. peak heights and noise floor, registered the

approximate same order of magnitude. Figure 33 shows the MLNG and PPIN simulated self-spectra with SNR corresponding to range cell 4.



(A) Simulated Self-Spectra of MLNG with SNR Attenuation



(B) Simulated Self-Spectra of PPIN with SNR Attenuation

Figure 33. Simulated Self-Spectra of (A) MLNG and (B) PPIN with SNR Corresponding to Range Cell 4

D. SCENARIO 3 SIMULATION MATRIX

The SNR attenuation and HF floor noise were computed for each generated spectra and the files were passed through the SeaSonde Suite. The hourly radial files were recovered using the same header parameters as before. The SeaSonde Suite was first configured to recover the radials using both the measured and theoretical antenna patterns, the latter phase-corrected using the **CrossLoopPatterner**. The computed phases stored in the stats-diag file were then averaged and used for the next recovery run by the theoretical pattern. The phases computed from the Stats-Diag file were both different in the single- and dual-solution current regimes, suggesting that phases computed by SeaSonde were sensitive to the ground-truth current pattern. This could have resulted from the interaction of the antenna, current and wind patterns. The simulation scenarios matrix for the sites is shown in Figure 34.

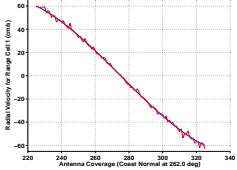
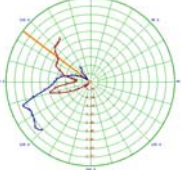
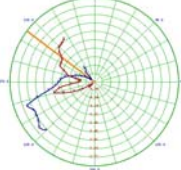
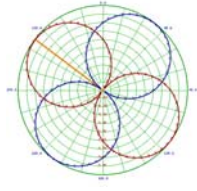

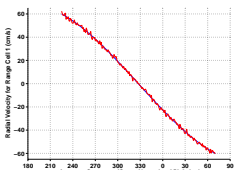
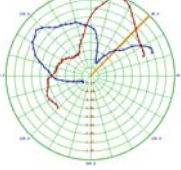
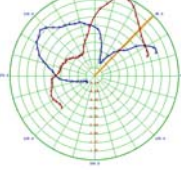
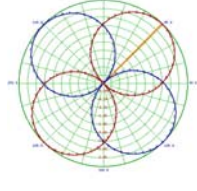
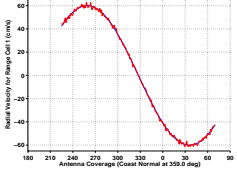
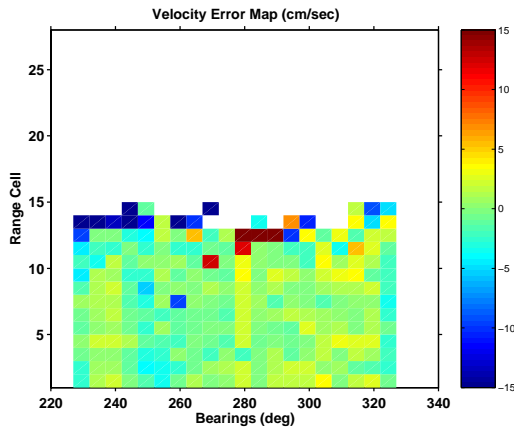
Scenario No.	Simulator Input		SeaSonde Recovery		
	Radial Patterns	Antenna Pattern (Amplitude)	Antenna Pattern (Amplitude)	Theoretical Pattern	
				Diag Phase	CrossLoop-Patterner Phase
3A		MLNG 	MLNG 		
				Phase = [10.7, 15.4]	Phase = [28.0, 9.1]
3B		PPIN 	PPIN 		
				Phase = [59.6, 34.4]	Phase = [75.7, 33.5]
				Phase = [42.8, 34.6]	Phase = [75.7, 33.5]

Figure 34. Scenario Matrix for Scenario 3 Series, with Inputs for Both the CSSim_mod and SeaSonde Suite

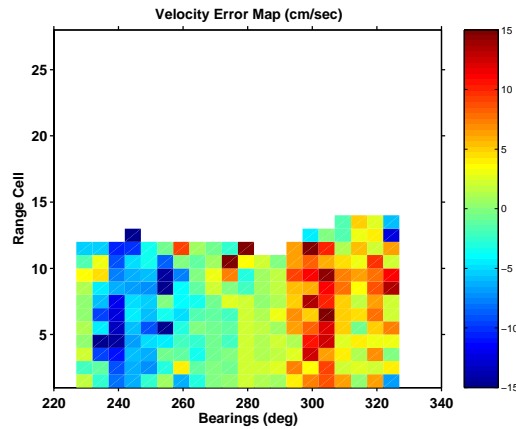
E. RESULTS

1. Scenario 3A

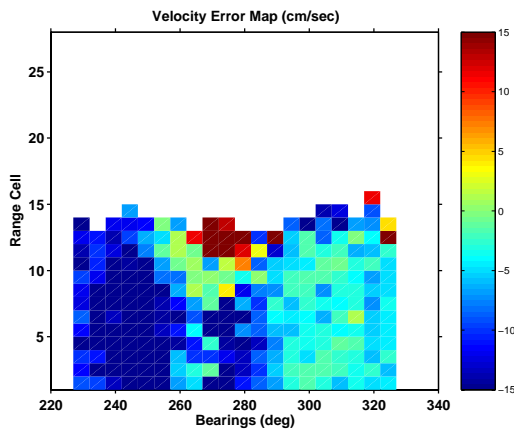
The velocity error (difference between the recovered and simulated radial currents) maps recovered by the MLNG's measured and ideal antenna patterns are plotted in Figure 35. The left panels shows the results obtained from the single-solution regime and the right panel shows the dual-solution regime. Each row across the bearings displays the velocity errors recovered at that range cell by the antenna pattern in question.



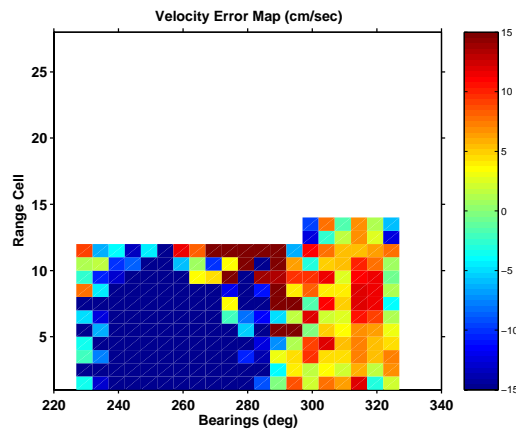
(A1) Measured



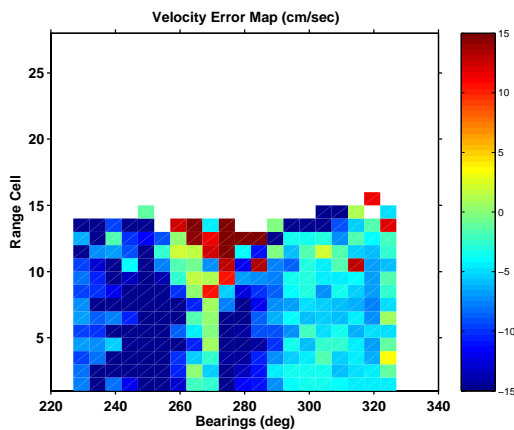
(B1) Measured



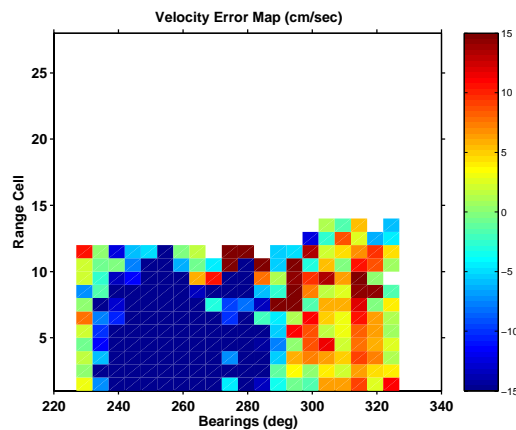
(A2) Ideal (w CrossLoopPatterner Phase)



(B2) Ideal (w CrossLoopPatterner Phase)



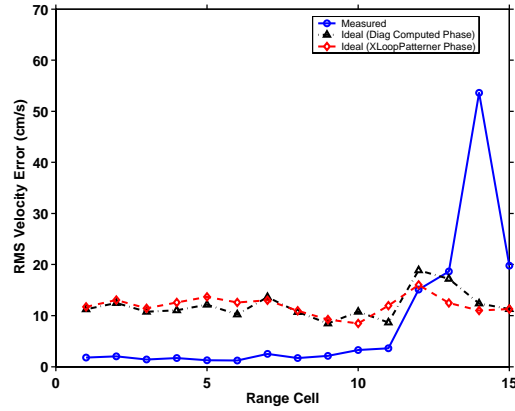
(A3) Ideal (w Stats-Diag Phase)



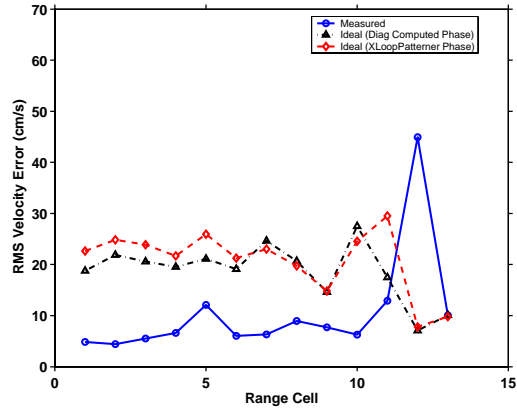
(B3) Ideal (w Stats-Diag Phase)

Figure 35. Velocity Error Maps Recovered by Measured Pattern (A1 and B1), Ideal Pattern with Phase Corrections from CrossLoopPatterner Tool (A2 and B2), and Ideal Pattern with Phase Corrections from Stats-Diag File (A3 and B3) at each Range Cell for Single- and Dual-Current Regimes (Left and Right Panels)

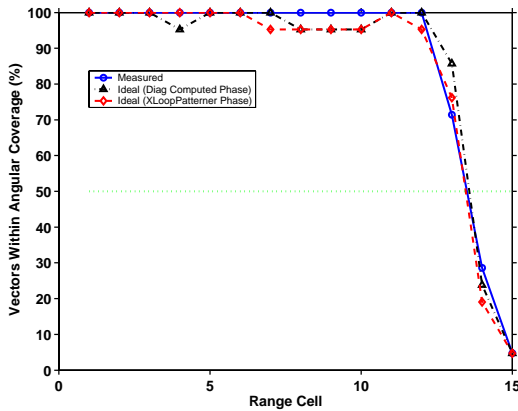
Figure 36 shows the RMS errors and coverage density of valid radials recovered at each range cell by the antenna patterns: measured (blue solid line with circle), ideal with Diag-Stats phase corrections (black dash-dot line with triangle), and ideal with **CrossLoopPatterner** phase corrections (red dash-line with diamond). The left panels shows the results obtained from the single-solution regime and the right panel shows the dual-solution regime.



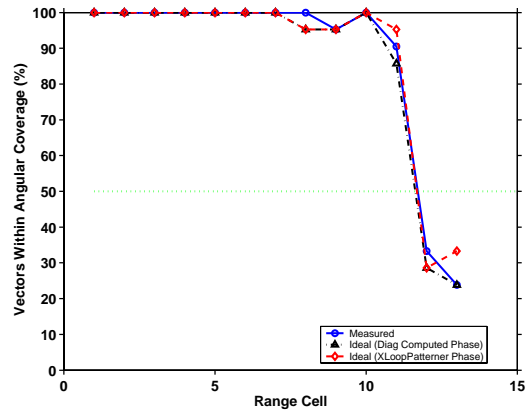
(A1) Single-Solution RMS Errors



(B1) Dual-Solution RMS Errors



(A2) Single-Solution Coverage Densities



(B2) Dual-Solution Coverage Densities

Figure 36. RMS Errors (A1 and B1) and Coverage Densities (A2 and B2) Recovered by the Antenna Patterns: Measured (blue solid line with circle), Ideal with Diag-Stats Phase Corrections (black dash-dot line with triangle), and Ideal with CrossLoopPatterner Phase Corrections (red dash-line with diamond) at each Range Cell for Single- and Dual-Current Regimes (Left and Right Panels)

The results from the simulation, though strictly relevant only to ocean areas that resemble the simulated conditions, had characteristics that should be applicable to other situations employing the 25 MHz SeaSonde as described below.

a. *Drowning of Bragg Peaks.*

Due to the higher rate of SNR attenuation, the Bragg peaks were quickly drowned by the HF noise floor. In this instance, no valid vectors were recovered from range cells 15 and 13 onwards for the single- and dual-solution currents, respectively. This corresponded to about 45.5 km and 39.4 km, respectively, which compared favorably to COS's designed range of about 40 km for the mid-band SeaSondes.

b. *Abrupt Decrease of Coverage Density*

Valid radials were recovered up to a "threshold" range after which coverage drops off substantially. In this case, the density coverage drops off to less than 50% by range cells 13 and 11 for single- and dual-solution patterns, respectively, which corresponded to 39.4 km and 33.4 km. Interpolation of radials beyond these ranges was not feasible due to these data gaps.

c. *Better Performance from Measured Antenna Patterns*

As expected from the previous scenarios, results recovered by the measured patterns had lowest RMS errors, but only when the coverage density exceeded 50%. The latter is, of course, related to the SNR. In Glenn et al. (2004), a power law relation for bearing uncertainty as a function of SNR was derived as:

$$\sigma_{\varphi} = \frac{1}{\sqrt{2 \times SNR}} \text{ radians} = \frac{40.5}{\sqrt{2 \times SNR}} \text{ degrees} \quad (19)$$

The above breaks down if SNR approaches unity but behaves asymptotically for large SNR. The above relation could be extended to estimate uncertainties in range or Doppler velocities (Barton, 1964). Its validity was tested in this study by comparing the predicted error as a function of range against the results of the range-dependent simulations. Figure 37 shows the theoretical curve (black solid line) of bearing uncertainty (for comparison purposes), the simulation results (blue '+' and red 'x') and their lines of best fit. The lines of best fit (based on least squares) were computed as $\sigma_{V_r} = \frac{2113.6}{SNR^{2.10}}$ for the single-

solution (blue dash-dot line) and $\sigma_{v_R} = \frac{180.50}{SNR^{0.98}}$ for the dual-solution current patterns (red dash line). Neither data set follows the bearing uncertainty power law relation, but the data points at SNRs approximately greater than 15 dB fit well with their respective lines of best fit, supporting a power law relation.

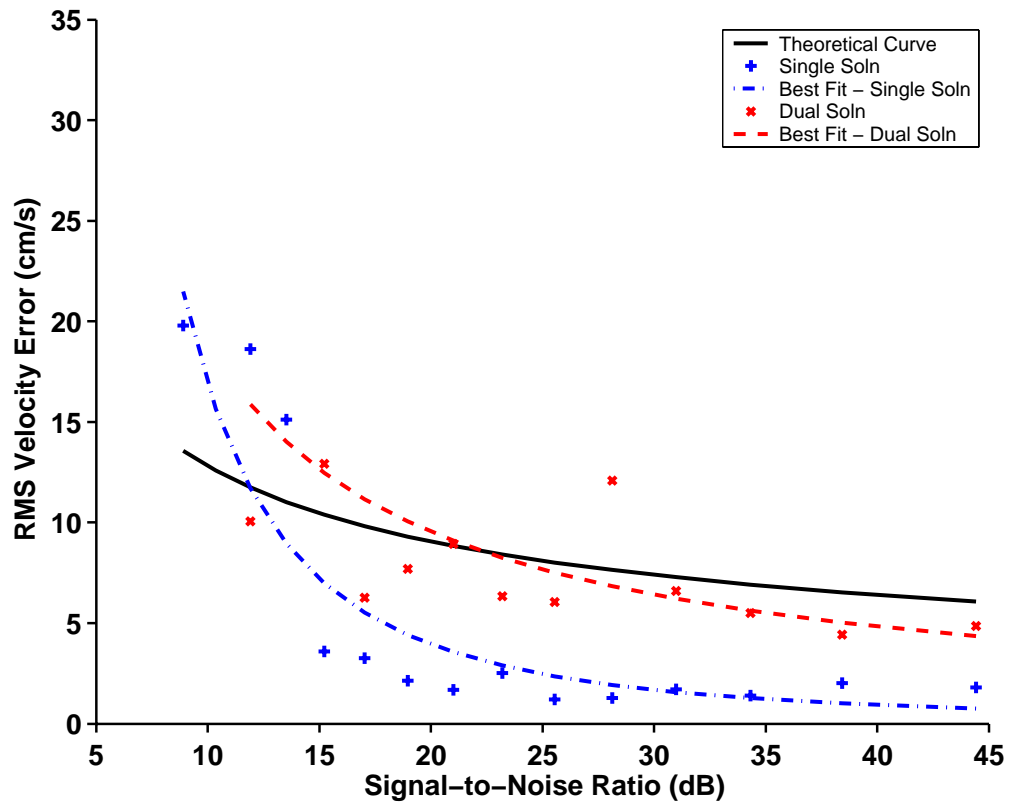


Figure 37. Simulation Results (Blue ‘+’ and Red ‘x’) and Lines of Best Fit (Blue Dash-Dot and Red Dash) Corresponding to the Single- and Dual-Solution Current Regimes, Respectively Compared with the Bearing Uncertainty Power-Law Relation.

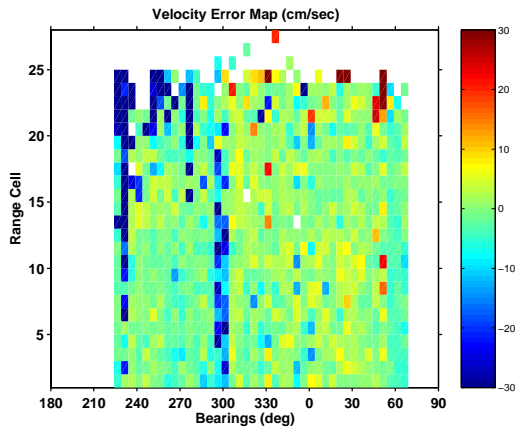
d. Biased Error Results by Ideal Antenna Pattern

Results in Figure 35 are also in agreement with observations by Emery & Washburn (1998) and Barrick & Lipa (1999) in that radial vectors derived by the Ideal antenna pattern were obviously biased. In this instance, there was a negative error bias for bearings less than bearing 280° in the single-solution case. Positive and negative

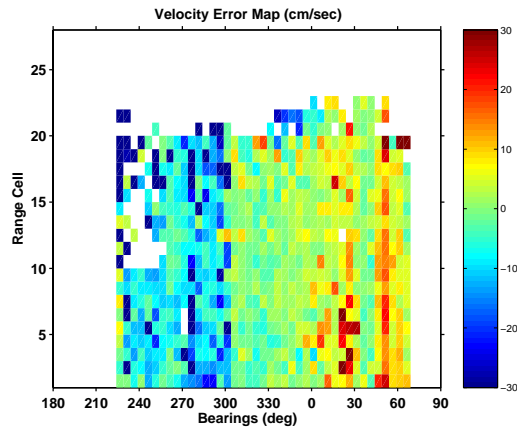
error biases for bearings greater than and less than 280° corresponded to the minima and maxima of the dual-solution radial pattern, respectively.

2. Scenario 3B

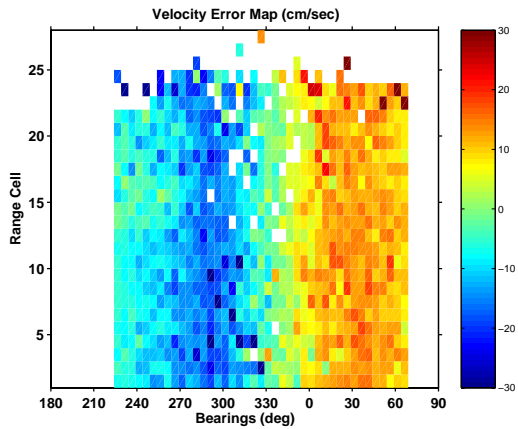
The velocity error maps recovered by the PPIN's measured and ideal antenna patterns are plotted in Figure 38. The left panels shows the results obtained from the single-solution regime and the right panel showing the dual-solution regime.



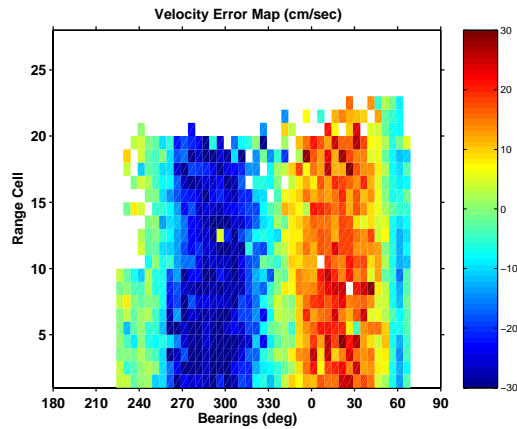
(A1) Measured



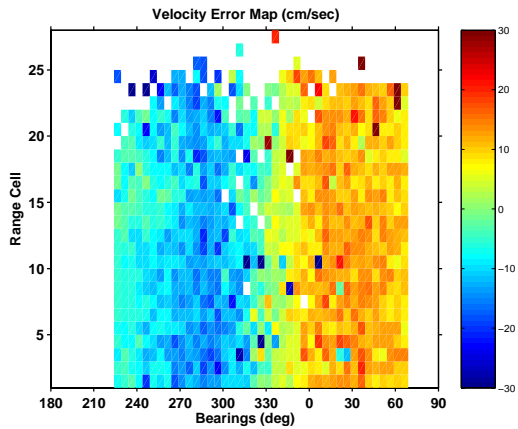
(B1) Measured



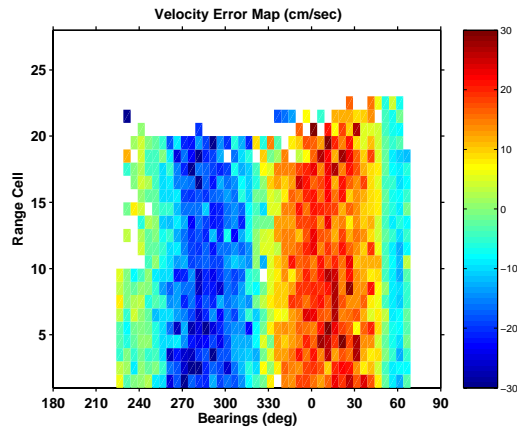
(A2) Ideal (w CrossLoopPatterner Phase)



(B2) Ideal (w CrossLoopPatterner Phase)



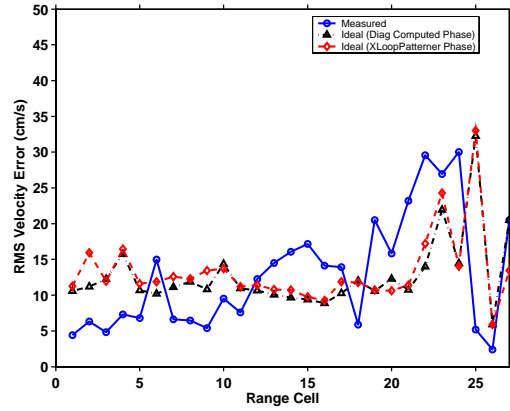
(A3) Ideal (w Stats-Diag Phase)



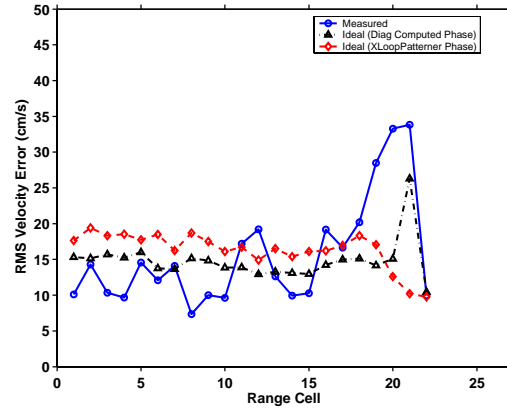
(B3) Ideal (w Stats-Diag Phase)

Figure 38. Velocity Error Maps Recovered by Measured Pattern (A1 and B1), Ideal Pattern with Phase Corrections from CrossLoopPatterner Tool (A2 and B2), and Ideal Pattern with Phase Corrections from Stats-Diag File (A3 and B3) at each Range Cell for Single- and Dual-Current Regimes (Left and Right Panels).

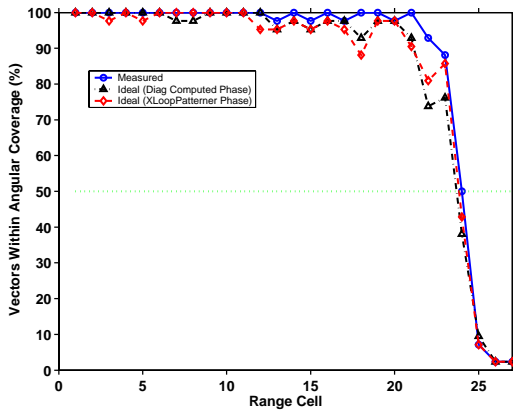
Figure 39 shows the RMS errors and coverage density of valid radials recovered by the antenna patterns: measured (blue solid line with circle), ideal with Stats-Diag phase corrections (black dash-dot line with triangle), and ideal with **CrossLoopPatternner** phase corrections (red dash-line with diamond). The left panels shows the results obtained from the single-solution regime and the right panel shows the dual-solution regime.



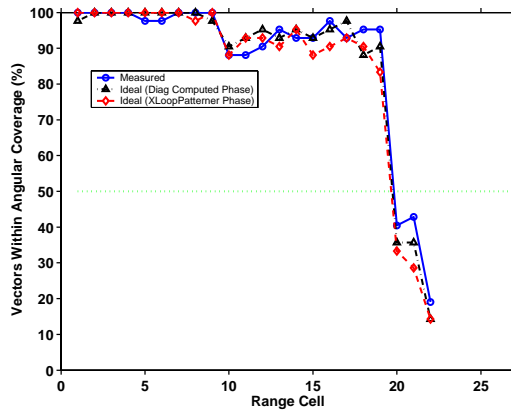
(A1) Single-Solution RMS Errors



(B1) Dual-Solution RMS Errors



(A2) Single-Solution Coverage Densities



(B2) Dual-Solution Coverage Densities

Figure 39. RMS Errors (A1 and B1) and Coverage Densities (A2 and B2) Recovered by the Antenna Patterns: Measured (blue solid line with circle), Ideal with Diag-Stats Phase Corrections (black dash-dot line with triangle), and Ideal with CrossLoopPatternner Phase Corrections (red dash-line with diamond) at each Range Cell for Single- and Dual-Current Regimes (Left and Right Panels)

Similar to the results from earlier scenario, results culled from this simulation would provide an insight to other situations operating the 13 MHz SeaSonde as described below.

a. *Drowning of Bragg Peaks.*

Due to the lower rate of SNR attenuation, the Bragg peaks were distinguishable from the HF noise floor until range cells 27 and 22 for the single- and dual-solution current pattern respectively. This corresponded to about 81.9 km and 66.7 km respectively, which compared favorably to COS's designed range of about 75 km for the 13 MHz SeaSondes.

b. *Abrupt Decrease of Coverage Density*

In this scenario, the density coverage drops off to less than 50% by range cells 23 and 19 for single- and dual-solution patterns respectively, which corresponded to 69.8 km and 57.6 km. Interpolation of radials beyond these ranges was not feasible due to these data gaps.

c. *Better Performance from Measured Antenna Patterns*

The results recovered by the measured antenna patterns were generally better than those recovered assuming ideal antenna patterns. However, at range cells 12 and beyond (corresponding to SNR less than 20 dB), the results from the ideal pattern were better, which adds another dimension to Paduan et al.'s (2005) observation that results from the ideal pattern were better along certain bearings.

Figure 40 shows the lines of best fit based on the power law relation for the single- and dual-solution as $\sigma_{V_R} = \frac{50.0}{SNR^{0.55}}$ (blue dash-dot) and $\sigma_{V_R} = \frac{86.5}{SNR^{0.60}}$ (red dash) respectively, which was surprisingly similar to the bearing uncertainty power law (black solid) relation to SNR as described earlier. However, it is noted that the fit was poorer than compared to Scenario 3A.

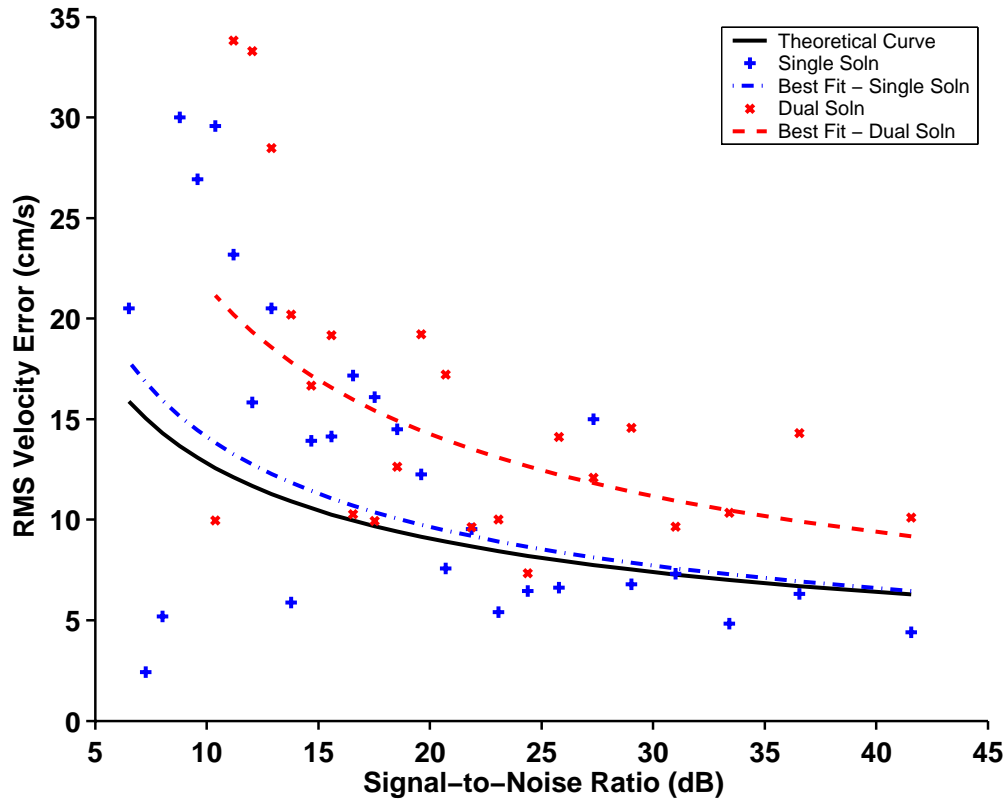


Figure 40. Data Points (Blue ‘+’ and Red ‘x’) and Lines of Best Fit (Blue Dash-Dot and Red Dash) Corresponding to the Single- and Dual-Solution Current Regimes Respectively Compared with the Bearing Uncertainty Power-Law Relation.

d. Biased Error Results by Ideal Antenna Pattern

This scenario continued to show consistent negative and positive error bias or banding in the radials recovered by the ideal antenna pattern which corresponded to the maxima and minima of the simulated radial pattern.

F. DISCUSSION OF RESULTS

Recovering the radial patterns from simulated spectra with range-sensitive SNR and frequency-dependent noise presented an unprecedented yet realistic look at SeaSonde’s performance under such conditions. While these results are restricted to physical (e.g. ocean surface and wind) conditions that are similar to the simulated ones, they provide insights to the character of the results expected in other operating conditions.

1. Maximum, Operational and Optimal Range of SeaSonde

Based on the SNR where the signals could be discriminated from the HF-noise floor, the SeaSonde's designers had designed the 13 MHz and 25 MHz SeaSondes to operate to maximum ranges of 75 km and 40 km, respectively. Results from the above scenarios support this specification, but it must be noted that the second-order backscatter effects were not simulated. Furthermore, the results also suggested that the furthest range where a Bragg peak could be localised depended on the radial current pattern – lower maximum range is achieved in a more complex current pattern. Lastly, the SNR is a complex interaction of frequency-, range- and environment-dependent variables, which vary from case to case, and so it is expected that the SeaSonde's maximum range would be less than specified.

Though an operational range was not officially defined, it could be associated with the “threshold” range, where radial coverage by the measured or ideal patterns falls off to less than 50%, and interpolation between velocity gaps is not be feasible. From the simulation, this is typically 6 to 10 km less than the maximum range.

Finally, an optimal range may be defined as the range where the RMS radial errors recovered by the measured antenna pattern are less than from the ideal. From the above scenarios, this is typically at a range where the SNRs are approximately greater than 15 dB and 20 dB for the 25 MHz and 13 MHz SeaSondes, respectively.

2. Results from Measured Antenna Patterns

When recovered by the measured antenna patterns, radial velocity errors were generally lower. However, these errors exceed the errors recovered by the ideal at SNRs at approximately less than 15 dB and 20 dB for the mid- and low-band SeaSondes respectively. This added another dimension to Paduan et al.'s (2005) observation that such reversal of results was bearings specific.

3. Power-Law Relation of RMS Errors to SNR

The power-law relation was attempted and results were encouraging, with reasonable curves fitting the data points at higher SNRs. Though the fit to the data points corresponding to the low-band SeaSonde was “looser”, the curves had a power factor of about 0.5 which compared well with the relation given by Glenn et al. (2004). On the other hand, the mid-band SeaSonde's data points had a closer fit to the curve, but the

power factor was about two and one for the single- and dual-solution respectively. The results suggested that while the RMS velocity errors may be described by a power-law relation to the SNR, they were however, inconsistent. This was probably because there were insufficient data points to remove any variability.

4. Biased Error Results by Ideal Antenna Pattern

Results from this scenario series showed consistent negative and positive error bias or banding in the radials recovered by the ideal antenna pattern, which corresponded to the maxima and minima of the simulated radial pattern.

THIS PAGE INTENTIONALLY LEFT BLANK

VI. CONCLUSIONS

The development of HF-radars to detect, measure and map sea surface currents has come a long way since the discovery of the Bragg scattering mechanism. Numerous field studies have been conducted to benchmark the HF radar's performance against in-situ current-measuring instruments. However, due to costs, testing inefficiency, resource intensiveness, differences in the nature of the measurements and differences in the spatial and temporal averaging scales, simulations gained prominence in recent studies.

A. SIMULATION PROCEDURE

Unlike previous simulations-based studies where MUSIC was evaluated independent of SeaSonde, this study attempted to let SeaSonde's MUSIC algorithm process the simulated spectral files into the radial current pattern. Chapter II gave an overview of SeaSonde's spectra analysis and radial processing cycle and described the process of integrating the MATLAB-based spectra generator into this cycle. The spectra generator was first fed with wind, antenna pattern and radial current inputs to produce the spectral files, which were subsequently passed into SeaSonde's software suite for processing by both the measured and ideal antenna patterns. The RMS errors between the recovered and inputted radial currents (which represented "ground-truth") were then used as a quantitative measure of performance.

Getting the software suite to isolate the Bragg peaks required the user to specify the localizing parameters, which exposed certain limitations and challenges faced by users operating the SeaSondes. For instance, the localizing parameters may need to become more adaptive to the changing physical environment. Furthermore, it was somewhat perplexing to note a potential systematic misalignment of indices representing the Bragg peaks in the spectra from the computed, which motivates the need to review the FFT algorithms adopted by MATLAB and SeaSonde.

B. SUMMARY OF RESULTS

Scenario 1 (Chapter III) used measured antenna patterns, which were variants of the ideal pattern but applied with a constant phase or amplitude deviation, to generate the spectral files. The radials were then recovered by the measured and ideal antenna patterns and their relative performance were compared.

Consistent with previous studies, the measured patterns gave the best results, followed by phase-corrected theoretical patterns. The study also confirmed that phase deviations, if overlooked by users, will contribute to significant errors while, in general, MUSIC's performance is more sensitive to amplitude than phase deviations.

Scenario 2 (Chapter IV) series set out to study MUSIC's ability to recover radial vectors subject to the phase and amplitude characteristics of the measured antenna pattern. Variants of the ideal pattern, used in Chapter III, were first used to generate a large ensemble of spectral files and the recovered radial files were averaged to remove the variability due to noise.

Amplitude deviations appeared to contribute to MUSIC's degraded performance and large RMS velocity errors occurred along bearings where there were also large deviations of the amplitude from the ideal. Consistent bands of errors of the same sign also suggested a possible indexing mis-alignment due to FFT operation as described in Chapter III. However, when the experiment was repeated using actual measured antenna patterns from MLNG and PPIN, the averaged results suggested a complex inter-play between the phase and amplitude deviations which rendered an inconclusive analysis. In addition, the distribution of velocity RMS errors did not necessarily coincide with the *SD_SeaSonde* computed by SeaSonde, suggesting that the latter may not be a good flag for erroneous radials. Gaps in the radial patterns recovered by measured patterns were observed, which may be antenna and frequency dependent.

Finally, Scenario 3 (Chapter V) used the MLNG and PPIN measured patterns to generate the spectral files coupled with a realistic attenuating SNR and frequency-dependent noise floor. The radials were then recovered by measured and phase-corrected idealized antenna patterns, and statistics on the aggregated RMS errors and radial coverage for each range cell were computed.

Though the maximum range, where Bragg peaks were localized, compared well with SeaSonde's designed range, a lower maximum range was predicted in operational conditions due to second-order effects, complex radial current patterns and signal attenuation. The notion of an operating range was suggested, to correspond with 50% radial coverage density for radial vector interpolation, and an optimal range where the

SNR reaches 15 to 20 dB so that the radial RMS error recovered by the measured pattern is less than the ideal.

Though results recovered by the measured patterns were generally better than the ideal, this simulation study also observed that performance reversals occur at SNRs below 15 to 20 dB. Lastly, due to a probable lack of data points, a power-law relation between RMS velocity errors to SNR was inconsistent.

C. APPLICATIONS

This study validated the expectation that radials recovered by the measured antenna pattern are generally better, and hence preferred, with exceptions at certain bearings and low SNR. This points out that the interaction of phase and amplitude deviations is complex and deserves further research. This is especially so when antenna patterns are severely distorted by the near-field environment onboard ships, oil rigs, coastal installations, etc. Understanding these limitations is crucial in developing plans for operational networks in support of Search and Rescue, oil spill management, and oceanographic and fishery science studies. In the military context, the increased accuracy in remote sensing and mapping of the surface current by the HF radar will improve the prediction of coastal circulation models and direct monitoring tools in an environmentally sensitive areas. Their products will enhance the planning of an amphibious assault, Special Forces sea insertion, or providing sea-land support in a humanitarian mission.

A relatively obscure but parallel application from this study lies in the use of the MUSIC algorithm in the military's DF SIGINT systems (SwRI, 1999). As these antennae are usually collocated with other antennae or in an environment with near-field distortions, such as ships or a fenced military installation, its DF antenna pattern is likely to be distorted in phase and amplitude. Therefore, pattern calibrations will be necessary to reduce the pointing error.

Lastly, as research is ongoing to develop Over-The-Horizon (OTH) HF radars (Glenn et al., 2004) to detect distant ships, measured patterns have been shown to give better bearing accuracy than ideal. Employment of such radars is a viable option to augment EEZ patrols and homeland security.

D. FUTURE WORK TO IMPROVE BEARING ACCURACY

A two-pronged approach is recommended to improve bearing accuracy by the SeaSonde: training and research. The initial inexperience of using SeaSonde Suite exposed certain procedural and analytical errors (Lipa, 2003), e.g. using the wrong antenna pattern, not orientating the ideal pattern to the correct bearing, incorrect use of phase-adjustment and angular filtering, etc. This shortfall, however, is easily addressed through training and experience.

The science (and art) of improving the HF-radar's current mapping may have reached a plateau. Many techniques has been devised, FMCW modulation to lower transmitter power, spatial and temporal averaging to remove noise, MUSIC to improve bearing accuracy, etc. Experienced users acknowledge the influence of the near-field environment and are beginning to account for it during the radial pattern recovery process. However, as this simulation has shown, the interaction of phase and amplitude deviations in the prediction of velocity uncertainty is a complex one, which influences the success of the eigenfunction-based MUSIC algorithm. Therefore, this compels further research in the following areas:

1. Antenna Design

The accurate recovery of radial patterns is predicated on the application of an accurately calibrated antenna pattern. However, as field and simulation studies have shown, there are instances in which the results recovered by the measured pattern fare worse than the ideal. Therefore, as this field of science goes beyond the realm of oceanography, it is probably a timely juncture to enlist antenna design expertise into the community of HF-radar users. For instance, even though SeaSonde has claimed that the orthogonally mounted cross-loop antennae are mutually decoupled from each other, it may be possible that coupling occurs due to near-field distortions. This is evident as the nulls of the measured do not necessarily coincide with the ideal pattern.

2. Adaptive Settings Adjustment

The accurate localization and subsequent processing of Bragg peaks are based on the choice of the "Factor Down" parameters in the header file. As the character of the Bragg peaks are dependent on factors like wind, current and antenna pattern, which vary with time and space, it may be imperative to find an adaptive means to optimally locate

the Bragg peaks. This can occur during the processor's lull time when the backscatter returns are collated and the spectra from the previous timestamp may be analyzed to predict the character of the Bragg peak since the environment changes at greater time scales than 10 mins.

3. Hybrid Resolution Processing

Analysis into Barrick & Lipa's (1996) implementation of MUSIC in the recovery of radials involved a parabolic fit and interpolation operation of antenna pattern with results from the Eigenstructure decomposition. However, as SeaSonde operates at a default angular resolution of 5° , this may not provide a sufficient level of accuracy to carry out the above operations. A futile attempt was made to circumvent this issue by using **CrossLoopPatternner** to interpolate the measured antenna pattern into 1° resolution and hoping that SeaSonde would output the radials at 5° resolution. However, the present software suite cannot handle this combination of angular resolution. Therefore, COS may wish to expand the scope of SeaSonde to process radials in this manner since a 1° resolution antenna pattern is readily available during the antenna calibrating process.

4. Hybrid Radial Processing

Field and simulation results have shown a performance reversal of radial recovery by measured and ideal antenna patterns along specific bearings. Therefore, it may be possible for SeaSonde, after a series of simulations, to know these vulnerable bearings and replace vectors recovered by the measured pattern by those recovered by the ideal.

5. "Research Mode" for SeaSonde Suite

The **RunAnalyzeSpectra** script packaged in SeaSonde has a very rudimentary means to monitor the progress of the radial recovery. In addition, temporary radial files are created prior to merging, which allows for some basic-level pre-processing. However, as future studies may directly use SeaSonde's MUSIC algorithm to process the radials, a "research mode" option will be invaluable as it strips the behind-the-scenes processing and allows the researcher to monitor the output from each step, without revealing the code which proprietary and patented (Barrick et al. 1994). For example, a more detailed Stats-Diag file can be configured to display the raw recovered radials before any form of averaging, which are used to produce a temporary radial file.

6. Frequency Management

SNR plays a critical role in accurate recovery of radial currents and, at present, the scientific users of HF radar instruments work as secondary not-to-interfere users of the radiowave band. As the use and the coordination of multiple HF radar installations grows, it will be beneficial to work toward dedicated frequencies within the HF band to be used by environmental monitoring systems, such as the SeaSonde. This will optimize system performance in terms of external noise sources while also simplifying the operational set up and management of the systems.

LIST OF REFERENCES

- Barton D.K., 1964: Radar Systems Analysis, New York, Prentice-Hall.
- Berry, L.A., and M.E. Chrisman, 1966: A Fortran program for calculation of ground wave propagation over homogeneous spherical earth for dipole antennas, *Rep. 9178*, National Bureau of Standards, Boulder, Colorado.
- Barrick, D.E., 1971: Theory of HF/VHF propagation across the rough sea. Part II: Application to HF/VHF propagation above the sea, *Radio Sci.*, vol. 6, pp. 527-533.
- Barrick, D.E., 1972: First-order theory and analysis of MF/HF/VHF scatter from the sea, *IEEE Trans. Antennas Propag.*, AP-20, pp. 2-10.
- Barrick, D.E., M.W. Evans, and B.L. Weber, 1977: Ocean surface currents mapped by radar, *Science*, Vol. 198, pp. 138-144.
- Barrick, D.E., B.J. Lipa, P.M. Lilleboe, and J. Isaacson, 1994: Gated FMCW DF radar and signal processing for range/Doppler/angle determination, U. S. Patent 5 361 072.
- Barrick, D.E. and Lipa, B.J., 1996: A comparison of direction-finding and beam-forming in HF radar ocean surface current mapping, *SBIR Phase I Final Report*, Contract No. 50-DKNA-5-00092 to National Oceanic & Atmospheric Administration, CODAR Ocean Sensors, Ltd., Los Altos, CA.
- Barrick, D.E. and Lipa, B.J., 1999: Using antenna patterns to improve the quality of SeaSonde HF radar surface current maps, Proceedings of the IEEE Sixth Working Conference on 11-13 March 1999, pp. 5-8.
- CCIR, 1988: Characteristics and applications of atmospheric radio noise data, *CCIR Recommendation 322-3*.

CODAR Ocean Sensor, 2004: How spectra are processed into radials, http://www.codaros.com/Manuals/InsideSeaSonde/ISS_CH4_SpectraToRadials.pdf (accessed on May 20, 2005).

CODAR Ocean Sensors, 2004: First Order Settings, http://www.codaros.com/Manuals/Informative/FirstOrder_Settings.pdf (accessed on May 20, 2005).

CODAR Ocean Sensors, 2004: Radial Configuration, http://www.codaros.com/Manuals/GuidesToFileFormats/File_RadialSetups.pdf (accessed on May 20, 2005).

CODAR Ocean Sensors, SeaSonde power to maximum range, 2005: http://www.codaros.com/Manuals/Informative/SeaSondePower_to_Range.pdf (accessed Jul 10, 2005).

Crombie, D.D., 1955: Doppler spectrum of sea echo at 13.56 Mc/s, *Nature*, vol.175, pp.681-682.

Derneryd, A. and Kristensson, G., 2004: Antenna signal correlation and its relation to the impedance matrix, *IEE Electronics Letters*, **40**(7), pp.401-402.

Emery, B.M. and Washburn, L., 1998: Comparison of surface current measurements in the Santa Barbara Channel: HF radar and moored current meters, Fall American Geophysical Meeting, *EOS Transactions*, AGU Vol.79,No.45, p. F393.

Emery, B.M., Washburn, L., and Harlan, J.A., 2004: Evaluating radial current measurements from CODAR high-frequency radars with moored current meters, *J. Atmos. Ocean Tech.*, pp. 1259 – 1271.

Fernandez, D.M., Laws, K.E., Paduan, J.D., 1999: High-frequency radar simulations, Proceedings of the IEEE Sixth Working Conference on 11-13 March 1999, pp. 9-13.

Glenn, S.M., Barrick, D.E., and Browning, W.J., 2004: Development of shiptracking capabilities for a dual-use multi-static long-range HF Radar Network, *Final Project Report*, Award No. N00014-02-10917, ONR.

K.-W. Gurgel, G. Antonischki, H.-H. Essen and T. Schlick, 1999: Wellen radar (WERA): a new ground wave radar for remote sensing, *Coastal Engineering*, **37**, pp. 219-234.

K.-W. Gurgel, H.-H. Essen, and S. P. Kingsley, 1999: HF radars: Physical limitations and recent developments, *Coastal Engineering*, Vol. 37, Nos. 3-4, pp. 201-218.

Hammond, T.M., C. Pattiaratchi, D. Eccles, M. Osbourne, L. Nash, and M. Collins, 1987: Ocean surface current radar vector measurements on the inner continental shelf. *Cont. Shelf Res.* **7**, 411-431.

Headrick, J.M., 1990: HF Over-the-Horizon Radar in Skolnick, M.I. (Ed), *Radar Handbook*, Second Edition, USA: McGraw Hill, pp. 24.1-24.40.

Kohut, J.T., Roarty, H.J., and Glenn, S.M., 2005: Characterizing observed environmental variability with HF Doppler radar surface current mappers and Acoustic Doppler current profilers, submitted to *IEEE J. Ocean Eng.*

Laws, K.E., Fernandez, D.M., Paduan, J.D., Teague, C.C., Vesecky, J.F., 1998: Simulation studies of errors in HF radar ocean surface current measurements, *Geoscience and Remote Sensing Symposium Proceedings*, 1998. Volume 1, pp.198-200.

Laws, L.E., 2001: Measurements of near surface ocean currents using H.F. radar, Doctoral dissertation, University of California, Santa Cruz.

Lipa, B.J. and D.E. Barrick, 1983: Least-squares methods for the extraction of surface currents from CODAR crossed-loop data: Application at ARSLOE, *IEEE J. Oceanic Engr.*, vol. OE-8, pp. 226-253.

Lipa, B., 2003: Uncertainties in SeaSonde Current Velocities, Proc. of the IEEE/OES Seventh Working Conference on Current Measurement Technology, Judith A. Rizoli, Ed., New York, March 2003, IEEE.

Lipa, B.J., B. Nyden, 2005: Directional wave information from the SeaSonde, *IEEE Jour. Ocean. Eng.*, Vol. 30, no. 1, pp 221-231.

Milsom, J.D., 1997: HF groundwave radar equations, HF Radio Systems and Techniques, Seventh International Conference on (Conf. Publ. No. 441) 7-10 July 1997, pp.285-290.

Norton, K.A., 1936: The propagation of radio waves over the surface of the earth and in the upper atmosphere, 1, Ground wave propagation from short antennas, *Proc. IRE*, **24**, pp. 1367-1387.

Paduan, J.D., J. O'Donnell, A. Allen, P.M. Kosro, S. Glenn, M. Bushnell, D. Musgrave, N. Shay, L. Washburn, and M. Luther, 2004: Surface current mapping in U.S. coastal waters: Implementation of a national system. Ocean. US, Arlington, VA, 22 pp.

Paduan, J.D., K.C. Kim, M.S. Cook, and F.P. Chavez, 2005: Calibration and validation of direction-finding high frequency radar ocean surface current observations. *IEEE J. Oceanic Engin.*, In Press.

Revell, J.C., Emery, D.J., 1998: HF surface wave radar simulation, Radar System Modeling (Ref. No. 1998/459), IEE Colloquium on 8 Oct. 1998, pp.:14/1-14/6.

R.O. Schmidt, 1986: Multiple emitter location and signal parameter estimation, *IEEE Trans. Antennas and Propagation*, vol. 34, pp. 276-280.

Sevgi, L., Sanal, S., 1997: Surface wave HF radar simulator, Radar 97 (Conf. Publ. No. 449), pp.181-184.

Sevgi, L., Ponsford, A., Chan, H.C., 2001: An integrated maritime surveillance system based on high-frequency surface-wave radars. 1. Theoretical background and numerical simulations, *Antennas and Propagation Magazine*, IEEE, Volume 43, Issue 4, pp.28-43.

Sevgi, L., Akleman, F., Felsen, L.B., 2002: Groundwave propagation modeling: problem-matched analytical formulations and direct numerical techniques, *Antennas and Propagation Magazine*, IEEE, Volume 44, Issue 1, pp.55-75.

Shearman, E.D.R., 1986: A review of methods of remote sensing of sea-surface conditions by HF radar and design considerations for narrow-beam systems, *IEEE J. Oceanic Engr.*, vol. OE-11, pp. 150-157.

Southwest Research Institute, 1999: Signal Exploitation and Geolocation Systems, <http://www.swri.edu/3pubs/brochure/d16/signal/signal.htm> (accessed on Nov 7, 2005).

Wait, J.R., 1962: Electromagnetic waves in stratified media, Oxford, England: Pergamon Press.

THIS PAGE INTENTIONALLY LEFT BLANK

INITIAL DISTRIBUTION LIST

1. Defense Technical Information Center
Ft. Belvoir, Virginia
2. Dudley Knox Library
Naval Postgraduate School
Monterey, California
3. Dr. Jeffrey D. Paduan
Department of Oceanography, OC/PD
Naval Postgraduate School
Monterey, California
4. Dr. Steven R. Ramp
Department of Oceanography, OC/RA
Naval Postgraduate School
Monterey, California
5. Dr. Mary L. Batteen
Department of Oceanography, OC/BV
Naval Postgraduate School
Monterey, California
6. Dr. Leslie K. Rosenfeld
Department of Oceanography, OC/PD
Naval Postgraduate School
Monterey, California
7. Dr. Donald E. Barrick, President
Codar Ocean Sensors, Ltd.
Los Altos, California
8. Dr. John F. Vesecky
Baskin School of Engineering
University of California at Santa Cruz
Santa Cruz, California
9. Dr. P. Michael Kosro
College of Oceanic Atmospheric Sciences
Oregon State University
Corvallis, Oregon